Applications of Weighted Dynamics Aggregation Modeling in Distributed Generation Systems

by

Aida Afshar Nia

A thesis submitted in partial fulfillment of the requirements for the degree of

Master of Science

in

Energy System

Department of Electrical and Computer Engineering
University of Alberta

Abstract

It has become increasingly common for power systems to use modular and distributed units to form complex systems. In such large-scale systems, several units with similar structures and control systems are usually interconnected at a Point of Common Coupling (PCC). In such systems, while the higher number of units increases reliability, efficiency, and energy harvesting, it makes system prediction and control system design more challenging. Furthermore, a large number of units interacting with each other and with the rest of the system connected to a PCC can result in unpredictable system behaviors, including oscillations, instability, and undesirable transient responses, which can limit the system's flexibility and scalability. Therefore, it is essential to continuously conduct power system studies to ensure the desired system performance, which demands a computationally efficient and accurate model to analyze and design modular large-scale systems. The weighted dynamic aggregation (WD Agg) method provides an equivalent model for a system consisting of parallel units with the same structure. This thesis applies the WD Agg method to two examples of the distributed generation system: DC microgrids and Doubly-Fed Induction Generator wind farms. The equivalent model mimics the detailed system's behaviour in steady-state and dynamic studies. Therefore, it can be used to study the behavior of the detailed system from a specific output.

Based on the WD Agg method approach, an islanded DC microgrid with droop-controlled DC-DC converters is studied and modeled. The WD Agg method proposes a single equivalent converter and an equivalent control system as a reduced-order model, which without sacrificing the accuracy, reduces the complexity of such large-scale system studies. It is shown that the model equivalent converter and control system parameters can be determined by the weighted average of the corresponding parameters of the large-scale system. The weight of each converter is quantified based on the contribution of that converter to the overall dynamic behavior of the large-scale system. WD agg model can accurately predict the transient response and can be employed in power planning, stability and sensitivity analyses with high accuracy. It is also shown that the proposed model can be used in designing the controller parameters of the large-scale system to ensure desirable system performance. The accuracy and applications of the proposed WD agg model are evaluated through time-domain simulations and experiments of an islanded microgrid consisting of three paralleled converters with different control parameters connected to a Constant Power Load (CPL) emulating a challenging system stability case.

DFIG-based Wind turbines and wind farms are also studied. The WD agg model presents an equivalent Wind Turbine Generator (WTG) consisting of an equivalent generator and an equivalent wind turbine. The $\mathrm{d-q}$ model of the wind farm is derived to find the contribution factor of each WTG. The proposed WD agg model provides an accurate single unit equivalent model for a large-scale wind farm while considering various wind speed zones and unequal WTG parameters. The WD model is evaluated through time-domain simulation of a 4-WTG and a large-scale 20-WTG DFIG-based wind farms in different wind speeds and WTGs parameters. The comparisons of WD models with the detailed model responses verify the method's accuracy in both steady-state and transient behaviors.

Preface

This thesis is an original work by Aida Afshar Nia. Chapter 3 is published as Navid Shabanikia, Aida Afshar Nia, Ahmadreza Tabesh, and S. Ali Khajehoddin, "Weighted dynamic aggregation modeling of induction machine-based wind farms," in IEEE Transactions on Sustainable Energy, vol. 12, no. 3, pp. 1604-1614, 2021. I was responsible for Doubly-Fed induction machine modeling and controller design. Navid Shabanikia proposed the weighted dynamic aggregation modeling and contributed to manuscript writing. Ahmadreza Tabesh was a visiting professor involved with concept formation, and Ali Khajehoddin was a supervisory author.

Acknowledgements

I would like to express my deepest gratitude to my supervisor, Dr. S.Ali Khajehoddin, for his guidance, patience, advice, and support throughout my master's studies. I also like to thank him for giving me the opportunity to develop my skills and pursue my aspirations in a vibrant, knowledgeable and friendly research group.

I would like to especially thank Navid Shabanikia for his mentorship during my research project. He assisted me through various aspects of my project in both theoretical and experimental phases. He also helped me learn new skills and provided support throughout the past three years.

I would also like to thank my friends at UAPEL for their friendship, support and encouragement during the past three years and for all the wonderful memories we made even during the pandemic. I like to thank Kimia Honari for her friendship and encouragement during challenging times in a new country, and for the sweetest memories we made along the way.

Last but not least, I would like to express an outstanding debt of gratitude to my parents and my brother, who encouraged and supported me throughout my life. My family's love kept me following my dreams and finding myself, and I love them with all my heart.

Table of Contents

List of Tables

List of Figures

List of Symbols

P	Active Power
P_{CPL}	CPL Power
P_W	Wind Power
P_m	Mechanical Power
Q	Reactive Power
V_{bus}	Bus Voltage
V_b	Stiff Voltage Source
v_{ref}	Reference Voltage
v_{load}	CPL Voltage
v_d	Diode Voltage
v_o	Converter Output Voltage
V_g	Grid Voltage
V_{dc}	DC Bus Voltage
v_s	Stator Voltage
v_r	Rotor Voltage
i_o	Converter Output Current
i_l	Converter Inductance Current
I_{CPL}	CPL Constant current Source
i_s	Stator Current
i_r	Rotor Current
i_g	Grid Current
ψ_s	Stator Flux
ψ_r	Rotor Flux

T_e	Electrical Torque
T_m	mechanical Torque
R_d	Droop Coefficient
R_{CPL}	CPL Resistance
R_l	Transmission Line Resistance
R_s	Stator Resistance
R_r	Rotor Resistance
L_b	Converter Inductance
L_l	Transmission Line Inductance
$L_{\sigma s}$	Stator Leakage Inductance
$L_{\sigma r}$	Rotor Leakage Inductance
L_m	Mutual Inductance
L_s	Stator Inductance
L_r	Rotor Inductance
C_b	Converter Capacitance
C_{load}	CPL Input Capacitance
s	Generator Slip
G	Gearbox Ratio
D	mechanical Damping
λ	Tip Speed Ratio
R	Wind Turbine Radius
p	Number of Poles
ρ	Air Density
C_p	Power Coefficient
V_W	Wind Speed
ω_m	Mechanical Speed
ω_r	Rotor Speed
ω_s	Stator Speed
θ_m	Mechanical Angle
θ_r	Rotor Angle

Acronyms

DG	Distributed Generation
PCC	Point of Common Coupling
CPL	Constant Power Load
LQR	Linear Quadratic Regulator
OFC	Output Feedback Controller
SFC	State Feedback Controller
MSM	Multi-time Scale Model
DFIG	Doubly-Fed Induction Generator
DFIM	Doubly-Fed induction Machine
WTG	Wind Turbine Generator
WD Agg	Weighted Dynamic Aggregation
Full Agg	Full Aggregation
Zone Agg	Zone Aggregation
RSC	Rotor Side Converter
GSC	Grid Side Converter
TSR	Tip Speed Ratio
PLL	Phase-Lock Loop
THD	Total Harmonic Distortion

Chapter 1

Introduction

Nowadays, the rise in energy prices and growing environmental concerns have led to a greater focus on creating clean, reliable, and efficient energy [1]. To meet the ever-rising energy demands, renewable energy sources and energy storage systems typically consist of smaller subsets connected in parallel [2]. Such subsystems generally have similar structures; however, they may differ in terms of parameters, inputs, and operating conditions. Although these aggregations facilitate the development of high power, reliable, and flexible distributed generation (DG) systems, the prediction of the dynamic response of such systems from a specific output is not straightforward [3].

Various methods model the aggregated systems from a specific output point of view. For example, the detailed state-space model can be derived by writing the differential equation of the state variables [4]. However, the computational burden of the state-space model intensifies as the number of parallel subsystems increases [5]. Therefore, several reduced-order methods are presented in [6–19] to promote accurate and computationally efficient models for the aggregated systems. For instance, the optimization methods define a set of restricting equations, and then the reduced-order model is determined by finding the best fit for these equations [7, 8, 20–24]. Although the optimization method can result in an accurate mathematical model of the aggregated system, it can be time-consuming due to the presence of all the state-space equations of the detailed model in a repetitive optimizing solution [20, 25].

Moreover, the optimization model needs to be updated for each operating condition to maintain the accuracy [21, 22].

The average method is another aggregation approach. This method presents an equivalent system whose equivalent parameters are defined as the average parameters of a detailed system [9–13, 26]. The average method typically assumes an ideal condition where all subsystems have similar parameters and dynamic behavior [12, 13]. However, parallel subsystems can have a vast array of parameters and operating conditions. Therefore, the average method may result in an inaccurate reduced-order model due to the varying dynamics.

To mitigate these problems, the zone-average method is presented in [14–16, 27, 28] for aggregating the parallel subsystems. The zone-average method divides the system into smaller zones and provides average models for each zone. To improve the accuracy of the zone-average model, each zone should consist of similar dynamic subsystems. Finding the appropriate criteria for specifying the zones and the reasonable number of zones [16, 28] are two of the challenges of this method.

The Weighted Dynamic Aggregated (WD Agg) method is another aggregating approach that presents an equivalent model with the similar structure of the original subsystems and similar dynamics as the detailed model [29, 30]. The equivalent parameters of the WD Agg model are derived by weighted averaging of the parallel subsystems' corresponding parameters. The weight of each subsystem can be determined by calculating the impact factor of that subsystem on the overall behavior of the detailed model [30, 31].

This thesis focuses on the application of the weighted dynamic aggregation method on two examples of DG systems: DC microgrids and Doubly-Fed Induction Generator (DFIG) based wind farms.

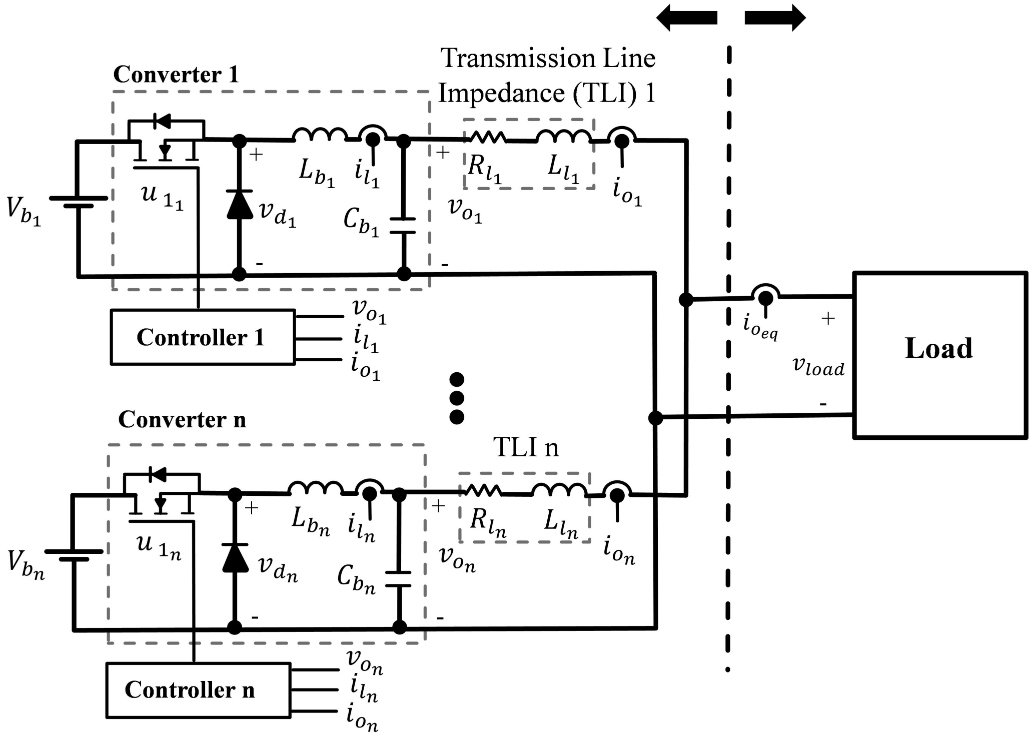

Figure 1.1: An isolated DC microgrid with parallel DC-DC converters

1.1 Review of Existing Reduced-Order Modelings

1.1.1 Droop Based DC Microgrid Modelings

An isolated DC microgrid consisting of parallel DC-DC converters, transmission lines, and a load is depicted in Fig. 1.1. DC microgrids usually feed Constant Power Loads (CPLs), which have negative impedance characteristics that can deteriorate the system stability [32, 33]. Moreover, output LC filters of the converters may resonate with other system components, which also affects the stability of the system [34]. Although paralleled converters with different characteristics can lead to a more efficient system, it may also result in undesirable responses in the microgrid [35]. Therefore, a computationally efficient and accurate model is required to analyze large-scale paralleled converters with different parameters.

Various methods are presented in [7–9, 26–28] to analyze and reduce the model complexity of large-scale paralleled converters. To analyze the stability of the DC microgrid, a state-space model of paralleled DC-DC converters is proposed [6]. The dynamic behavior of the control systems is ignored in this model to reduce the computational cost of analyzing a large number of parallel converters. The optimization methods can be utilized to introduce reduced-order mathematical models based on the dominant eigenvalues of the system [7, 8]. However, the loss of the omitted frequency modes can lead to model inaccuracy [23, 24].

A Thevenin-based model is another reduced-order model that divides the system into smaller clusters [9, 26]. Each cluster is then modelled based on its equivalent thevenin voltage and impedance. This model considers equal power generations, input voltages, and collector line parameters for parallel subsystems. It is worth mentioning that reducing a detailed converter to a single voltage source and impedance shown in Fig. 1.2a can result in too simplistic models ignoring the natural modes of the system [36]. Also, modeling a system with unequal control parameters can result in an inaccurate model due to ignoring the control system dynamics in the model derivations [27, 28, 30].

To improve the model accuracy with unequal parameters, Multi-Time Scale Model (MSM) is proposed in [27, 28]. MSM clusters converters with the same ratio of droop coefficients to the line inductance and models each cluster similar to Thevenin-based methods shown in Fig. 1.2b. However, collector line inductance values are difficult to estimate, and assuming equal droop coefficients would be a limiting assumption.

1.1.2 Doubly-Fed Induction Generator (DFIG) Based Wind Farm Modelings

A large number of Wind Turbine Generators (WTGs) use doubly-fed induction machines to increase speed operating range and decrease rotor loss as compared to fixed-speed WTGs. In these WTGs, the stator is connected directly to the grid while the rotor is connected to the grid through an AC-DC-AC variable frequency converter shown in Fig. 1.3. A wind farm consisting of n parallel DFIG wind turbines connected

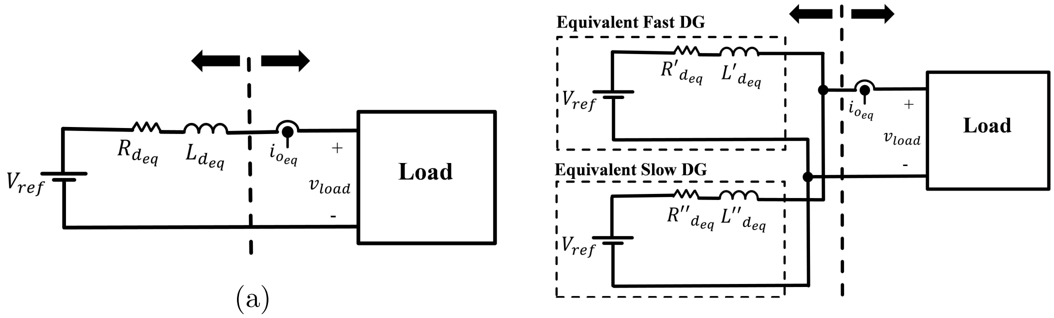

(a)

(b)

Figure 1.2: Existing reduced-order models of parallel-connected DC microgrid (a) Thevenin-based model (b) MSM model

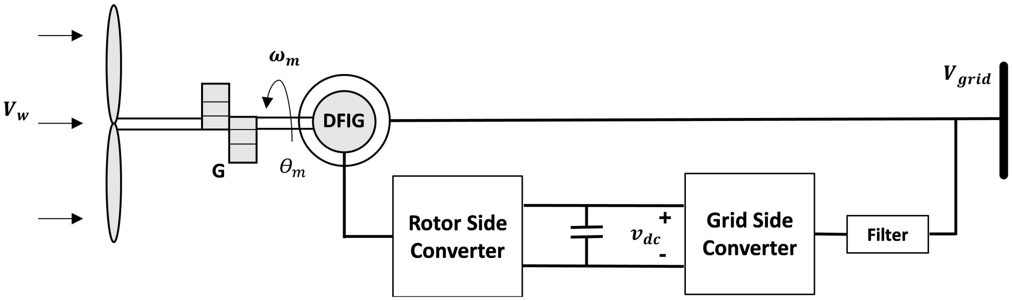

Figure 1.3: A DFIG WTG schematic

to the grid is depicted in Fig. 1.4.

With large-scale wind farms becoming more prevalent in power systems, an aggregation model is required to model such a wind farm with an equivalent system. The aggregation model reduces the computational burden during steady-state and dynamic analyses. Therefore, the proposed model should be computationally efficient and adequately accurate in steady-state and dynamic behavior studies for a wind farm, including hundreds of WTGs under different operating conditions.

Various aggregation methods are suggested in the literature to model a large-scale wind farm. For example, the equivalent admittance of the wind farm is used as the equivalent aggregated model in [37, 38]. Nevertheless, applying this method to DFIG wind farms on a large scale is complex and time-consuming. The optimization methods are suggested to model a large-scale DFIG wind farm using the state-space model of WTGs [21–24]. The equivalent parameters of these models are obtained

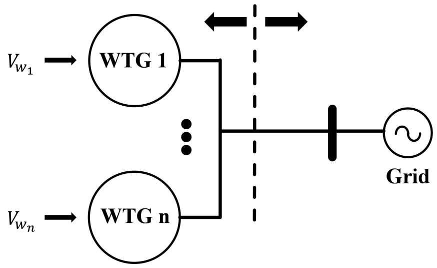

Figure 1.4: n-WTGs wind Farm, where V_{W_j} is jth wind speed

through finding the best solution to the set of optimization equations. To provide an accurate model, the optimization solution needs to be updated for each wind farm operating point which is a computationally expensive process.

The Full aggregation (Full Agg) model is presented in [10–13] for a wind farm with equal wind speed (V_W) and WTG parameters in per unit. This method models the wind farm by one equivalent WTG where the equivalent parameters are calculated by averaging the WTGs parameters in per unit. In this approach, the equivalent apparent power of the reduced-order model is the summation of the wind farm power. It is noteworthy that the accuracy of the Full Agg model significantly decreases when incorporating different wind speed zones and unequal machine parameters [12, 13].

The Zone aggregation (Zone Agg) method divides the wind farm into a few zones based on the wind speed inputs and models each zone with the Full Agg method [14–16]. As a result, the accuracy of the zone Agg model is greatly improved at the expense of model complexity, which makes the Zone Agg method not optimal for modeling large wind farms. The Semi Agg method is presented in [17–19] where the mechanical part of WTGs is preserved. However, its electrical aspect is replaced by a single generator and converter with corresponding average parameters. While the semi-Agg method provides an accurate model, the need for modeling all mechanical components of the WTGs makes the model inefficient for large-scale wind farms.

The basic idea of the Weighted Dynamic Aggregated (WD Agg) method is suggested in [29]. The WD Agg method provides an equivalent unit where its parameters are derived by determining the impact factor of each subsystem in the parallel system.

The suggested WD Agg method is further developed in this thesis for DFIG-based wind farms and DC microgrids.

1.2 Weighted Dynamic Aggregation (WD Agg) Basic Concept

The weighted dynamic aggregation method provides a reduced-order model of a system composed of parallel subsystems with a similar structure. Typically, these subsets have different inputs, parameters, and operating conditions. Therefore, the WD Agg method proposes a model with the same structure, where its equivalent parameters are obtained through the weighted averaging of the subsystems' parameters. The weight of each subsystem can be calculated based on the contribution of that subsystem's dynamic behaviour to the overall dynamic behaviour of the system.

Since parallel subsystems are connected at the Point of Common Coupling (PCC) bus, the dynamic behavior of each subsystem can be determined based on the incremental current each subsystem contributes at the PCC bus. The proposed WD Agg converter delivers $S_{WD} = \sum_{j=1}^{n} S_j$ to the load, where S_j and S_{WD} are the jth subsystem and proposed WD Agg converter normalizing power value in (VA), respectively. The suggested model is shown to be accurate in steady-state and transient behavior analysis. Moreover, it is computationally efficient, easy to use, and appropriately complex for various dynamic behavior studies.

1.2.1 Weighted Dynamic Aggregation Model for Droop Based DC Microgrid

To address some of the challenges associated with existing methods, the Weighted Dynamic aggregation (WD Agg) concept outlined in [29] is developed for n parallel DC-DC converters in an islanded DC microgrid. The proposed method models the detailed system with a single equivalent converter and its corresponding controller shown in Fig. 1.5. The parameters of the equivalent converter and its control system

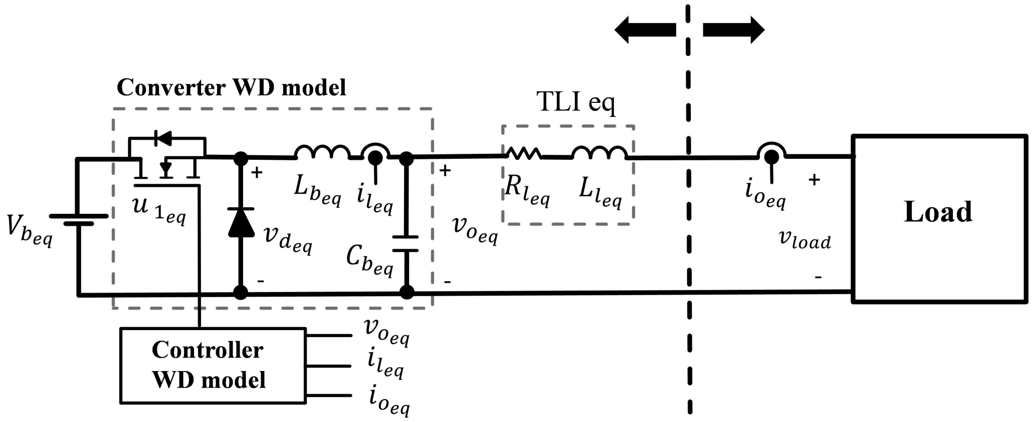

Figure 1.5: A WD Agg model of paralleled-connected DC microgrid

can be determined by weighted averaging of the detailed model parameters. For example, the equivalent buck inductance $L_{b_{eq}}$ can be calculated as:

$$L_{b_{eq}} = \sum_{j=1}^{n} \frac{\mu_j}{n} L_{b_j}, \tag{1.1}$$

where L_{b_j} is the jth converter buck inductance, and μ_j is:

$$\mu_j = \frac{i_{o_j}}{i_{o_{eq}}}, \tag{1.2}$$

with $i_{o_{eq}} = \sum_{j=1}^{n} i_{o_j}$. Then, the μ_j can be calculated based on the system parameters by writing differential equations of the detailed system. Likewise, other equivalent parameters of the WD Agg model can be determined.

Presenting a single equivalent converter and controller reduces the model complexity and computational burden while providing an accurate steady-state and transient behavior. Furthermore, the proposed WD Agg model does not have limiting assumptions such as an equal ratio of droop coefficients to the line inductance, making it more practical and realistic.

1.2.2 Weighted Dynamic Aggregation Model for DFIG Based Wind Farm

The weighted dynamic aggregation method is also used to model DFIG-based wind farms to propose a reduced-order model that mimics the behavior of the detailed

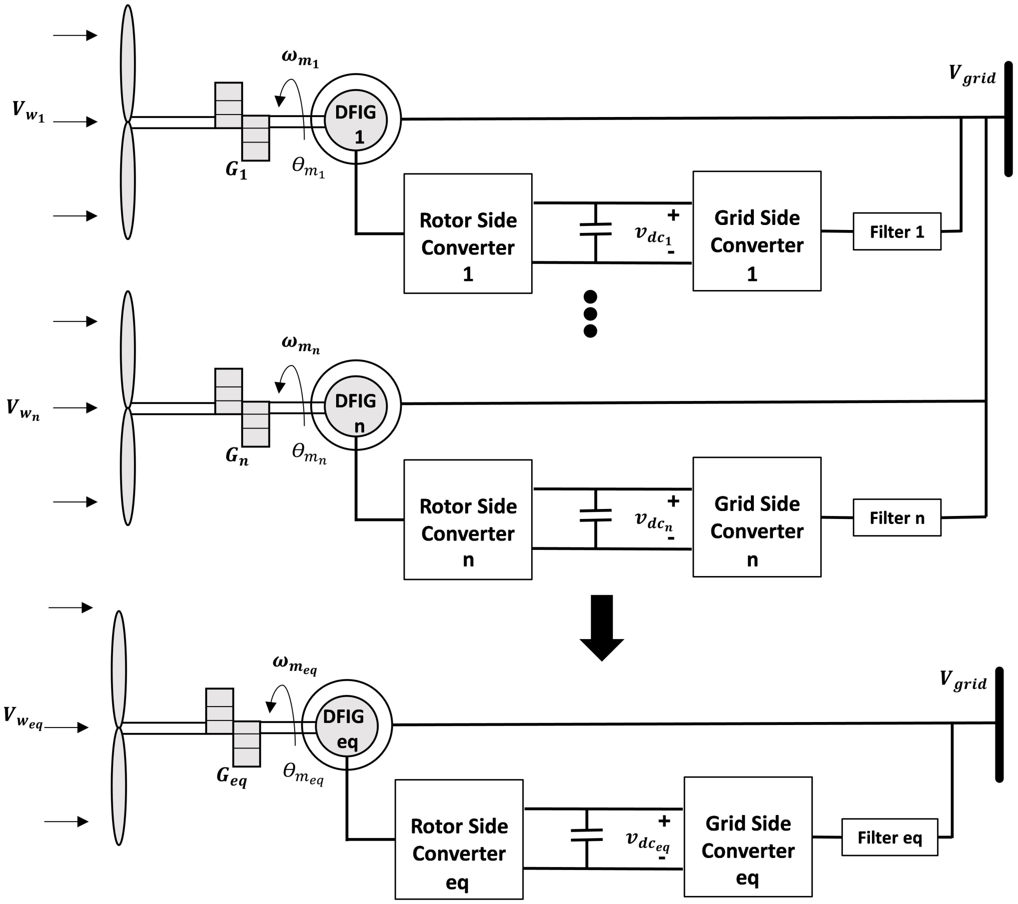

Figure 1.6: A WD Agg model of DFIG-based wind farm

wind farm. This method proposes an equivalent WTG with an equivalent mechanical turbine as a reduced-order model of the wind farm as shown in Fig. 1.6. With the equivalent turbine, a simpler model is established to provide a better understanding of the mechanical system behavior that has not been adequately addressed in previous methods. The mechanical equivalent parameters of the WD model are calculated based on the fact that the equivalent turbine should behave like the summation of all the wind turbines of that wind farm. For example, the equivalent area that the WD turbine covers A_{eq} is:

$$A_{eq} = \sum_{j=1}^{n} A_k, \tag{1.3}$$

where A_k is the area covered by kth turbine. The electrical equivalent parameters of the WD Agg model are also calculated by weighted averaging of the wind farm's corresponding parameters. It is shown that the weights of each WTG can be calculated based on the contribution of that WTG injected current to the grid.

The WD Agg model presents a straightforward approach due to its derivation set of aggregated dynamic equations. Because the WD Agg model incorporates the contribution of WTGs into the equivalent reduced-order model, the WD Agg model is significantly accurate in mimicking the behavior of the detailed wind farm. Furthermore, the simple wind farm equivalent generator is derived from a one-time calculation, leading to a considerably low computational burden and a simple model.

1.3 Thesis Objectives

The main objective of this thesis is to apply the Weighted Dynamic Aggregation method to two examples of DG systems: DC microgrids and DFIG-based wind farms. The WD Agg models are shown to be accurate in steady-state and transient behavior, computationally efficient, and practical in various dynamic behavior studies. For this purpose, the aforementioned systems are modelled and compared to the previously existing and detailed models in various steady-state and dynamic behavior studies. Briefly, the dissertation's objectives are:

1. To develop a DC-DC converter model with a control strategy that ensures proper load sharing and voltage regulation;

2. To derive a state-space model of a system consisting of n paralleled DC-DC converters feeding a CPL to be used in various stability analysis studies;

3. To propose an equivalent converter and controller as a new reduced-order WD Agg model of paralleled DC-DC converters and also to derive the state-space model of the WD Agg model to be compared with the existing reduced-order and detailed models in stability and sensitivity analysis;

4. To evaluate the functionality of the proposed WD Agg model through time-domain simulation and experiments in various scenarios that include different control parameters, output filter capacitance and input voltages;

5. To develop the $d-q$ model of a DFIG-based wind farm to ensure the DC link stability and to provide the desired active and reactive power according to the wind speed;

6. To derive the steady-state model and small-signal model of the WTG to provide the dynamic model of the wind farm;

7. To propose a WD Agg model for a DFIG-based wind farm consisting of equivalent electrical (generator and control system) side and mechanical part (the equivalent turbine);

8. To assess the steady-state and transient responses of a WD Agg model by simulating a wind farm with similar and unequal parameters in a voltage sag;

1.4 Thesis Outline

In Chapter 2, an overall description of an islanded DC microgrid feeding a CPL is discussed. The states and output of the studied system are controlled using a droop control loop in conjunction with a modified linear quadratic regulator (LQR) state feedback control loop. The open-loop and closed-loop state-space model of these paralleled buck converters is derived using a linear representation of a CPL. The weighted dynamic aggregation model of paralleled converters is proposed, and its equivalent parameters are obtained by considering the contribution of each converter's dynamic behavior. The performance of the proposed WD Agg model is assessed by studying an islanded DC microgrid with three parallel buck converters connected to a CPL, where most of the DC microgrid stability issues occur. The closed-loop eigenvalues' trajectory of the studied system is derived to address the stability and sensitivity issues. The functionality of the WD Agg model is assessed through simulation and experimental results in various scenarios, including considering equal and unequal parameters for the converters, controllers and input voltages at start-up and power step changes.

In chapter 3, a DFIG WTG and wind farm are studied. The desired operating point of the DFIG for the given wind speed is investigated. Then, the wind turbine and DFIG are modeled. Also, the space vector representation of a Doubly-Fed induction Machine is derived. The rotor side converter is designed to determine the operating condition of the system based on the wind speed. The grid side converter is designed to establish the DC link voltage and set the demanded reactive power. To provide the dynamic model of the WTG and wind farm, the small-signal model of WTG is derived via steady-state calculations at the operating condition. The $\mathrm{d}-\mathrm{q}$ presentation of the WTG and wind farm is derived. The WD Agg model is proposed for a DFIG-based wind farm, and its equivalent mechanical and electrical parameters are obtained. The WD Agg model is evaluated by time-domain simulation of the wind farm with similar and unequal parameters and during voltage sag.

Finally, Chapter 4 summarizes the contribution of the thesis and proposes a few other possibilities for future research.

Chapter 2

Droop Based DC Microgrid Analysis and Design

2.1 Introduction

A microgrid is a small, self-sustainable group of distributed energy resources that can work in grid-connected or islanded mode. Compared to AC microgrids, DC microgrids have higher efficiency, lower cost, and more straightforward control due to the absence of reactive power, frequency regulation, and skin effect issues [39, 40]. Many renewable energy sources and common loads are inherently DC type; thus, DC microgrids have better efficiency due to reduced power conversion stages. Moreover, DC microgrids are more straightforward to be designed with a plug-and-play feature. Therefore, islanded DC power systems are gaining more attraction in residential and industrial buildings, data centers, naval ships, submarines, electric vehicles, and remote area microgrids [41–46].

In DC microgrids, a large number of paralleled converters are deployed to meet the increasing energy demand and improve the efficiency and reliability of the system. However, parallel connection of DC converters leads to higher system complexity and introduces new stability issues [32].

2.1.1 Control Strategies

Any minor mismatch of the paralleled converters output voltage can generate circulating current that can lead to overloading the converters and deteriorating the system performance [47]. Therefore, the control system of parallel converters should establish proper load sharing and voltage regulation. To fulfill the aforementioned goals, master-slave and droop control methods are being used conventionally [48].

Master-Slave Control

In the master-slave method, one converter designates the voltage/current reference for all the other converters, based on the current status of the converters [49, 50]. As a result, fast communication is crucial for this method, which can be costly. Furthermore, the reliability and stability of the system are prone to a single point of failure, which is the master unit. The increasing trend in integrating parallel sources presents challenges in terms of stability and hierarchy control in this method [35].

Droop Control

The droop control system determines voltage/current reference by measuring the local variables of each converter; hence, communication links are not essential. Therefore, the droop control is more reliable, less expensive, and more flexible due to facilitating the plug-and-play capability [51]. Droop control is a virtual resistance added in the feedback path of voltage reference to decrease the output voltage as the load current increases or vice versa. Therefore, the local voltage reference of each converter in this method is calculated as:

$$V_{ref} = V_{bus} - R_d I_o, \tag{2.1}$$

where V_{bus} is the measured DC-bus voltage, R_d is the droop coefficient, and I_o is the output current of the corresponding converter. This makes converters farther away from an ideal source, which results in greater interaction between sources and loads. Moreover, the droop control provides active damping to the system [52].

However, the droop control method is a compromise between output voltage regulation and current sharing between the converters due to the resistances between the lines and the non-identical nature of each converter. In other words, a larger droop coefficient leads to better current-sharing while deteriorating the voltage regulation. Therefore, additional secondary control is required to improve the voltage regulation. Droop control is utilized as the control strategy in this chapter.

2.1.2 Stability Challenges

Increasing the number of DC converters can lead to unpredictable system behaviors and can introduce new stability issues [32]. For example, it can be observed that unequal droop coefficients can lead to stability issues [35]. Therefore, maintaining the system's stability is another primary purpose of the control system.

Also, an output LC filter is often used between a DC-DC converter and its power source to comply with conducted emission and susceptibility standards [53]. However, the output LC filter of converters may resonate with other system components, which can deteriorate the system behavior or result in instability of the system [34].

Moreover, DC microgrid loads are connected to the DC-bus through regulated point-of-load converters, which make them behave as constant power loads (CPLs) [54]. CPLs are often the cause of instability and lack of equilibrium of dc microgrids due to their negative impedance characteristics [32, 33].

Therefore, an accurate and computationally efficient model of paralleled DC-DC converters in islanded DC microgrids is needed to study the system's behaviour and to design a stable system. Thus, paralleled converters with different characteristics connecting to a CPL are studied in this chapter. A state-space model of the system is derived to analyze large-scale paralleled converters with different parameters in various stability and sensitivity analysis.

2.2 System Description

Fig. 2.1 shows the block diagram of a DC microgrid formed by parallel DC-DC converters interconnected by unequal transmission lines using a droop control. The system comprises three primary components: paralleled converters, transmission lines, and loads.

Paralleled converters

Because sources can generate different voltages, DC-DC buck converters are utilized to connect sources to the DC microgrids and equalize the converters' output voltage to the local reference value.

An outer droop control loop is used in conjunction with an inner modified Linear Quadratic Regulator (LQR) state feedback loop to ensure proper load sharing and voltage regulation, as shown in Fig. 2.1.

Transmission Lines

In DC microgrids, sources come from relatively remote areas; as a result, the impedance of transmission lines cannot be ignored. Therefore, transmission lines are modeled as a series combination of resistance and inductance (R_l,L_l) as shown in Fig. 2.1.

Loads

Loads are also connected to the DC microgrid via DC-DC converters to provide the demanded constant power regardless of variations in the DC microgrid voltage. Hence, A CPL is considered as the system load. The relation between the voltage and the current of a CPL for a given operating point of ($I_{cpl} = P_{cpl}/V_{CPL}$) is:

$$i_{cpl} = \frac{P_{cpl}}{v_{CPL}}, \tag{2.2}$$

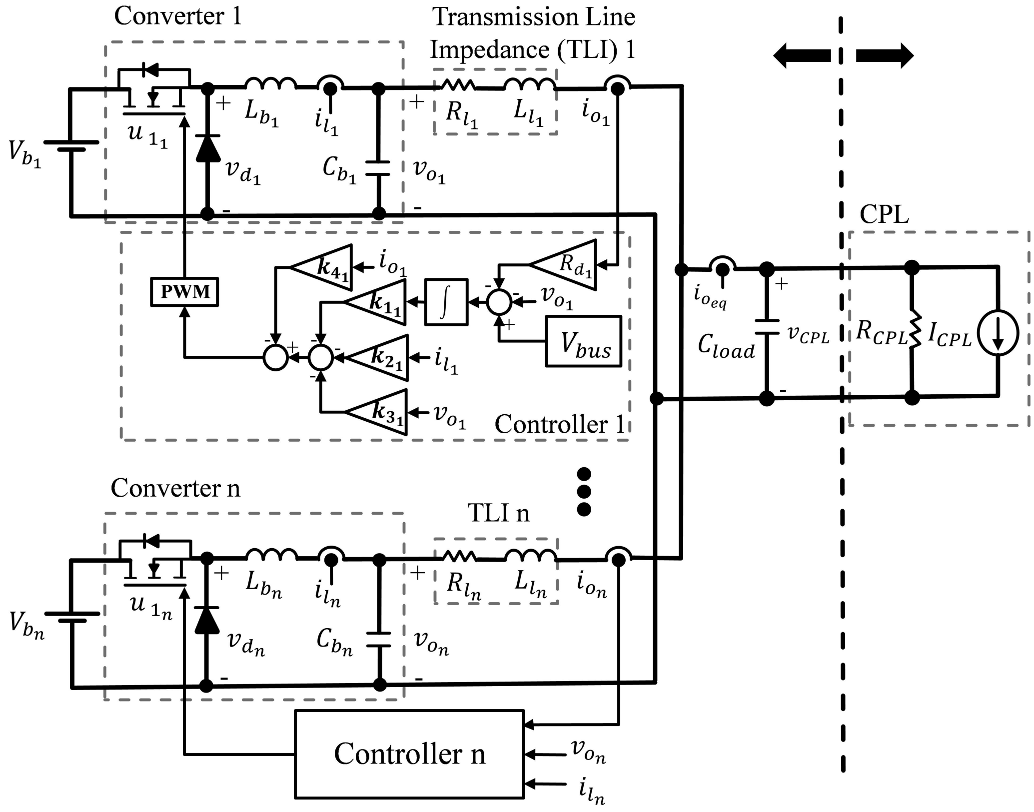

Figure 2.1: The studied DC microgrid with parallel converters feeding a linear CPL

where P_{cpl} and V_{CPL} are the demanded power and voltage of the load, respectively. Therefore, the rate of change in current can be obtained from 2.2 as:

$$\frac{\partial i_{cpl}}{\partial v_{CPL}} = -\frac{P_{cpl}}{V_{CPL}^2}. \tag{2.3}$$

Hence, the curve representing the current versus voltage at the operating point can be approximated by a straight line tangent to the curve as follows:

$$i_{cpl} = -\frac{P_{cpl}}{V_{CPL}^2} v_{CPL} + 2\frac{P_{cpl}}{V_{CPL}}. \tag{2.4}$$

Equation (2.4) indicates that a CPL can be modelled by a negative resistance (R_{cpl}) parallel with a constant current source (I_{cpl}) as shown in Fig. 2.1. The R_{cpl} and I_{cpl} are:

$$R_{cpl} = -\frac{V_{CPL}^2}{P_{cpl}}, \tag{2.5}$$

$$I_{cpl} = 2\frac{P_{cpl}}{V_{CPL}}. \tag{2.6}$$

CPLs are often connected in parallel and usually have the same structure; therefore, one CPL shown in Fig 2.1 is the aggregation of a cluster of the same CPLs in parallel connection.

2.2.1 Droop Control Loop Design

The control strategy plays a significant role in system performance and stability when a CPL is connected to the DC microgrid. The objective is to have a stable system with the desired power-sharing for all system operating conditions and through CPL reference power changes. Detailed explanations regarding system conditions are:

- Different system operating conditions stem from the unidentical converters with unequal controller and input voltage parameters. This phenomenon causes a different range of current levels for which the controller must be able to operate.

- The DGs are connected to the DC bus via output LC filters, which degrade the system stability. The resonance phenomenon of the LC filter should be controlled to avoid undesirable oscillations during various operating conditions of the system.

- Components of the system such as CPLs have nonlinearities, which can cause current distortion. The controller must be able to minimize the impacts of these phenomena on the quality of the injected current.

- The reference power of the CPL may have several step changes because it models the aggregation of parallel CPLs with the same structure. The controller should be able to update the current level of the converter to provide adequate power for the CPLs.

Control Approach

As mentioned earlier, the local voltage reference of each converter is determined by the droop coefficient as obtained in (2.1). In islanded DC microgrids, the DC bus

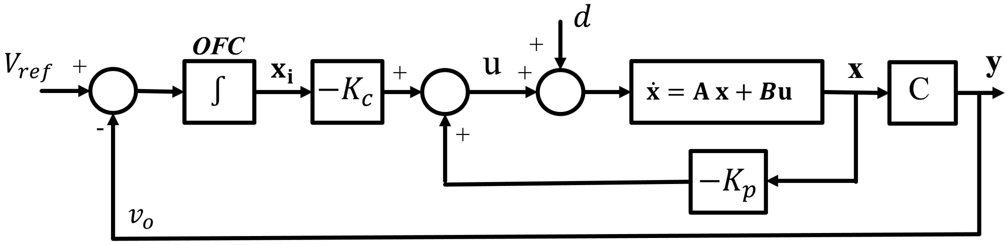

Figure 2.2: The proposed closed-loop structure

voltage should be stiffed and injected currents' quality is important. Therefore, a simple proportional (P) or proportional-integrating (PI) type of controller may lead to a non-zero steady-state error. Moreover, current disturbances caused by the output LC filter and CPL nonlinearities cannot be rejected with these controllers. A closed-loop structure shown in Fig 2.2 is selected to ensure that the actual value of the reference voltage is achieved in the desired operating condition and the disturbance is completely rejected. This control loop is designed based on the fact that if a certain signal must be tracked or rejected without steady-state error, the signal dynamic must be inside the control loop [55].

The power distribution system in an islanded DC microgrid should be stable independently of the load side. Therefore, v_{CPL} can be regarded as a disturbance that has the same dynamics as the input signal since v_{CPL} state belongs to the load side of the system. To find the optimal controller parameters, a tuning method based on the classical notion of LQR of optimal control theory is employed. The LQR control method originally formulated for a regulation problem has been extended to solve the basic droop control tracking problem. The LQR formulation presented in this section provides an easy yet powerful method of tuning controller gains of parallel converters to achieve the aforementioned goals of the control system.

Concept of Linear Quadratic Regulator (LQR)

The state-space representation of a linear time-invariant system can generally be written as:

$$\dot{\mathbf{x}} = \mathbf{A}\mathbf{x} + \mathbf{B}\mathbf{u}, \quad x(0) = x_0, \tag{2.7}$$

$$\mathbf{y} = \mathbf{C}\mathbf{x} + \mathbf{D}\mathbf{u}, \tag{2.8}$$

where $\mathbf{A} \in R^{(n\times n)}$, $\mathbf{B} \in R^{(n\times m)}$, $\mathbf{C} \in R^{(p\times n)}$, $\mathbf{D} \in R^{(p\times m)}$ are constant matrices, $\mathbf{u}$ is the control signal, $\mathbf{x}$ is the state vector, and $\mathbf{y}$ is the system's output. A conventional LQR problem aims to design a full-state feedback law in the form of $u = -\mathbf{K}\mathbf{x}$ that optimally regulates the output and state of this system [56]. In the LQR problem, the quadratic cost function is defined as:

$$J(u) = \int\limits_0^\infty (\mathbf{x}^T\mathbf{Q}\mathbf{x} + \mathbf{u}^T\mathbf{R}\mathbf{u})dt, \tag{2.9}$$

where $\mathbf{Q} = \mathbf{Q}^T \in R^{(n\times n)}$ is a positive (semi) definite and $\mathbf{R} = \mathbf{R}^T \in R^{(m\times m)}$ is a positive definite matrix. Matrix Q and R in the cost function are predefined constants selected based on the importance of each state or input. Because the LQR method minimizes the cost function, the greater each term of the Q and R matrices, the smaller the energy the corresponding state and the input signal will have during the transients. The optimal $\mathbf{K}$ for solving the 2.9 is:

$$\mathbf{K} = \mathbf{R}^{-1}\mathbf{B}^T\mathbf{F}, \tag{2.10}$$

where the symmetric matrix $\mathbf{F} = \mathbf{F}^T \in R^{(n\times n)}$ is obtained by solving the following equation:

$$\mathbf{A}^T\mathbf{F} + \mathbf{F}\mathbf{A} + \mathbf{Q} - \mathbf{F}\mathbf{B}\mathbf{R}^{-1}\mathbf{B}^T\mathbf{F} = 0. \tag{2.11}$$

The closed-loop model of this system with the state feedback law u = -$\mathbf{K}\mathbf{x}$ can be written as:

$$\dot{\mathbf{x}} = (\mathbf{A} - \mathbf{B}\mathbf{K})\mathbf{x} = \mathbf{A}_{cl}\mathbf{x}, \tag{2.12}$$

where the eigenvalues of the $\mathbf{A}_{cl}$ are the closed-loop poles.

The LQR solution is traditionally used to regulate state variables; however, the control system's output should usually track specific reference commands. Therefore, the modified LQR solution is suggested to find the optimal controller gains which regulate the state variables and track the input signal in [57]. To achieve this purpose, an extra output feedback controller (OFC), in addition to the state-feedback controller (SFC), is utilized as shown in Fig. 2.2.

Proposed control loop

The buck converter shown in Fig. 2.1 can be modelled as:

$$\begin{aligned} L_b \frac{di_l}{dt} &= uV_b - v_o, \\ C_b \frac{dv_o}{dt} &= i_l - i_o, \end{aligned} \tag{2.13}$$

where u is the duty cycle, L_b is the inductance, and C_b is the capacitance of the corresponding buck converter. v_o is the voltage across C_b, i_l is the current flow through L_b, and i_o is the output current of the converter. The model of the transmission line can be shown by:

$$L_l \frac{di_o}{dt} = v_o - R_l i_o - v_{CPL}, \tag{2.14}$$

where L_l and R_l are the equivalent inductance and resistance of the transmission lines and load input filter, respectively. The CPL can be modelled by:

$$C_{load} \frac{dv_{CPL}}{dt} = \sum_{j=1}^{n} i_{o_j} - I_{cpl} - \frac{v_{CPL}}{R_{cpl}}, \tag{2.15}$$

where C_{load} is the input filter capacitance of the load and v_{CPL} is the voltage across C_{load}. Therefore, the state-space representation of a buck converter feeding a CPL can be described as:

$$\dot{\mathbf{x}} = \mathbf{A}\mathbf{x} + \mathbf{B}_1 u + \mathbf{B}_2 I_{CPL}, \tag{2.16}$$

$$\dot{\mathbf{y}} = \mathbf{C}\mathbf{x}, \tag{2.17}$$

where $\mathbf{x} = \begin{bmatrix} i_l & v_o & i_o & v_{CPL} \end{bmatrix}^T$, $\mathbf{B}_1 = \begin{bmatrix} \frac{V_b}{L_b} & 0 & 0 & 0 \end{bmatrix}^T$, $\mathbf{B}_2 = \begin{bmatrix} 0 & 0 & 0 & \frac{-1}{C_{load}} \end{bmatrix}^T$, $C = \begin{bmatrix} 0 & 1 & 0 & 0 \end{bmatrix}$, and A is:

$$\mathbf{A} = \begin{bmatrix} 0 & \frac{-1}{L_b} & 0 & 0 \\ \frac{1}{c_b} & 0 & \frac{-1}{c_b} & 0 \\ 0 & \frac{1}{L_l} & \frac{-R_l}{L_l} & \frac{-1}{L_l} \\ 0 & 0 & \frac{1}{C_{load}} & \frac{-1}{R_{cpl}C_{load}} \end{bmatrix}. \tag{2.18}$$

The reference signal V_{ref} shown in Fig. 2.2 comes from (2.1). Therefore, The output of the OFC $\dot{\mathbf{x}}_i$ can be written as:

$$\dot{\mathbf{x}}_i = V_{ref} - v_o = V_{bus} - R_d i_o - v_o = V_{bus} - C_e x, \tag{2.19}$$

where $C_e = \begin{bmatrix} 0 & 1 & R_d & 0 \end{bmatrix}$ and $\mathbf{x}_i$ is the state vector of the OFC. Therefore, the state space equations of the system and the output feedback controller, when augmented together can be described as the closed-loop state-space equations

$$\dot{\mathbf{x}}_c = \mathbf{A}_c\mathbf{x}_c + \mathbf{B}_{c_1}u + \mathbf{B}_{c_2}I_{CPL} + \mathbf{B}_{c_3}V_{bus}, \tag{2.20}$$

$$y = \mathbf{C}_c\mathbf{x}_c, \tag{2.21}$$

where $\mathbf{x}_c = \begin{bmatrix} \mathbf{x} & \mathbf{x}_i \end{bmatrix}^T$ is the vector of the state variables, and the matrices are

$$\mathbf{A}_c = \begin{bmatrix} A & 0 \\ C_e & 0 \end{bmatrix}, \quad \mathbf{B}_{c_1} = \begin{bmatrix} B_1 \\ 0 \end{bmatrix}, \quad \mathbf{B}_{c_2} = \begin{bmatrix} B_2 \\ 0 \end{bmatrix}, \quad \mathbf{B}_{c_3} = \begin{bmatrix} 0 \\ 1 \end{bmatrix}, \quad \mathbf{C}_c = \begin{bmatrix} C & 0 \end{bmatrix}. \tag{2.22}$$

Note that the control signal u can be expressed as:

$$u = -\begin{bmatrix} k2 & k3 & k4 & 0 & k1 \end{bmatrix} \begin{bmatrix} \mathbf{x} \\ \mathbf{x}_i \end{bmatrix} = -\mathbf{K}\mathbf{x}_c, \tag{2.23}$$

which is the standard form of a state-feedback law. To avoid excessive usage of sensors, the load input filter v_{CPL} is not used as a feedback signal in the state-feedback loop. Analysis of the design shows that the controller operates desirably without using the load side capacitor voltage.

The LQR concept can be extended to directly address the optimal tracking problem as explained in [57]. The LQR method can provide a solution for the combined system under the assumption that $(\mathbf{A}_c, \mathbf{B}_{c_1})$ is stabilizable, $\mathbf{R} > 0$, and $\mathbf{Q} \geq 0$. The solution is obtained from (2.11) and is conveniently calculated in Matlab using the command $\mathbf{K} = lqr(\mathbf{A}_c, \mathbf{B}_{c_1}, \mathbf{Q}, \mathbf{R})$. The LQR technique transforms the problem of selecting closed-loop poles of $\mathbf{A}_{cl}$ into selecting the matrices $\mathbf{Q}$ and $\mathbf{R}$. In a single-input system, R can be scaled to unity without losing generality.

The $\mathbf{Q}$ matrix is a non-negative diagonal matrix with the same number of elements as the controller gain K, i.e. Q = diag(q1, q2, q3, q4, q5). The q_j attributes are selected based on the fact that increasing each q_j element decreases the deviation of the corresponding state from zero. Therefore, a systematic search can be used to discover a suitable selection that results in a desirable performance of the closed-loop system. It is noteworthy that stability is guaranteed for any choice of non-negative $\mathbf{Q}$, and the selection of q_j attributes only affects the transient response of the closed-loop system. Thus, tuning the controller parameters is achieved by subsequent increases in q_j attributes and observing their impact on the system's speed, overshoot, current quality, etc.

2.2.2 State-Space Model of Parallel DC-DC Converters

Differential equations of the system are derived for stability analysis purposes. A stiff DC source is considered as the input voltage of the converters. The state-space representation of the linear DC microgrid system can be described as:

$$\dot{\mathbf{x}} = \mathbf{A}\mathbf{x} + \mathbf{B}_1\mathbf{u} + \mathbf{B}_2 I_{cpl}, \tag{2.24}$$

where $\mathbf{x} = \begin{bmatrix} i_{l_1} & v_{o_1} & i_{o_1} & \cdots & i_{l_n} & v_{o_n} & i_{o_n} & v_{CPL} \end{bmatrix}^T$, $\mathbf{u} = \begin{bmatrix} u_{1_1} & \cdots & u_{1_n} \end{bmatrix}$, $\mathbf{B}_1 = \begin{bmatrix} \frac{V_{b_1}}{L_{b_1}} & 0 & 0 & \cdots & \frac{V_{b_n}}{L_{b_n}} & 0 & 0 & 0 \end{bmatrix}^T$, $\mathbf{B}_2 = \begin{bmatrix} 0 & 0 & 0 & \cdots & 0 & 0 & 0 & \frac{-1}{C_{load}} \end{bmatrix}^T$, and

A is:

$$\mathbf{A} = \begin{bmatrix} \mathbf{A}_1 & 0 & \cdots & 0 & \mathbf{A}_{1_L} \\ 0 & \mathbf{A}_2 & \cdots & 0 & \mathbf{A}_{2_L} \\ \vdots & \vdots & \ddots & \vdots & \vdots \\ 0 & 0 & \cdots & \mathbf{A}_n & \mathbf{A}_{n_L} \\ \mathbf{A}_{1_C} & \mathbf{A}_{2_C} & \cdots & \mathbf{A}_{n_c} & \frac{-1}{R_{cpl}C_{load}} \end{bmatrix}. \tag{2.25}$$

where $\mathbf{A}_{j_L} = \begin{bmatrix} 0 & 0 & \frac{-1}{L_{l_j}} \end{bmatrix}^T$, $\mathbf{A}_{j_C} = \begin{bmatrix} 0 & 0 & \frac{1}{C_{load}} \end{bmatrix}$, and:

$$\mathbf{A}_j = \begin{bmatrix} 0 & \frac{-1}{L_{b_j}} & 0 \\ \frac{1}{c_{b_j}} & 0 & \frac{-1}{c_{b_j}} \\ 0 & \frac{1}{L_{l_j}} & \frac{-R_{l_j}}{L_{l_j}} \end{bmatrix}, \tag{2.26}$$

for $j = 1, 2, ..., n$.

The detailed system's closed-loop model is shown in Fig. 2.3 where the modified LQR technique is used to design a state feedback law $u = -\mathbf{K}\mathbf{x}$ to optimally regulate the states and the output of the studied system to zero. The state-space model of the closed-loop system can be shown by:

$$\dot{\mathbf{x}}_e = \mathbf{A}_d \mathbf{x}_e + \mathbf{B}_d u_2 + \mathbf{B}_r r, \tag{2.27}$$

where $\mathbf{x}_e = \begin{bmatrix} x & u_{1_1} & \cdots & u_{1_n} \end{bmatrix}^T$, $u_2 = I_{CPL}$, $r = V_{bus}$. A_d is:

$$\mathbf{A}_d = \begin{bmatrix} \mathbf{A} & \mathbf{B}_{1_1} & \cdots & \mathbf{B}_{1_n} \\ \mathbf{A}_{d_1} & -\mathbf{C}_{u_1}\mathbf{B}_{1_1} & \cdots & -\mathbf{C}_{u_1}\mathbf{B}_{1_n} \\ \vdots & \vdots & \ddots & \vdots \\ \mathbf{A}_{d_n} & -\mathbf{C}_{u_n}\mathbf{B}_{1_n} & \cdots & -\mathbf{C}_{u_n}\mathbf{B}_{1_n} \end{bmatrix}, \tag{2.28}$$

with:

$$\mathbf{C}_{u_j} = -k_{2_j}\mathbf{C}_{1_j} - k_{3_j}\mathbf{C}_{2_j} - k_{4_j}\mathbf{C}_{3_j}, \tag{2.29}$$

where $i_{l_j} = \mathbf{C}_{1_j} \times \mathbf{x}$, $v_{o_j} = \mathbf{C}_{2_j} \times \mathbf{x}$, $i_{o_j} = \mathbf{C}_{3_j} \times \mathbf{x}$, and $\mathbf{B}_{1_j}$ is the jth column of $\mathbf{B}_1$. k_{1_j}, k_{2_j}, k_{3_j} and k_{4_j} are the controller coefficients of jth converter shown in Fig. 2.3 and calculated in (2.23). $\mathbf{A}_{d_j}$ is:

$$\mathbf{A}_{d_j} = k_{1_j}\mathbf{C}_{e_j} - \mathbf{C}_{u_j}\mathbf{A}, \tag{2.30}$$

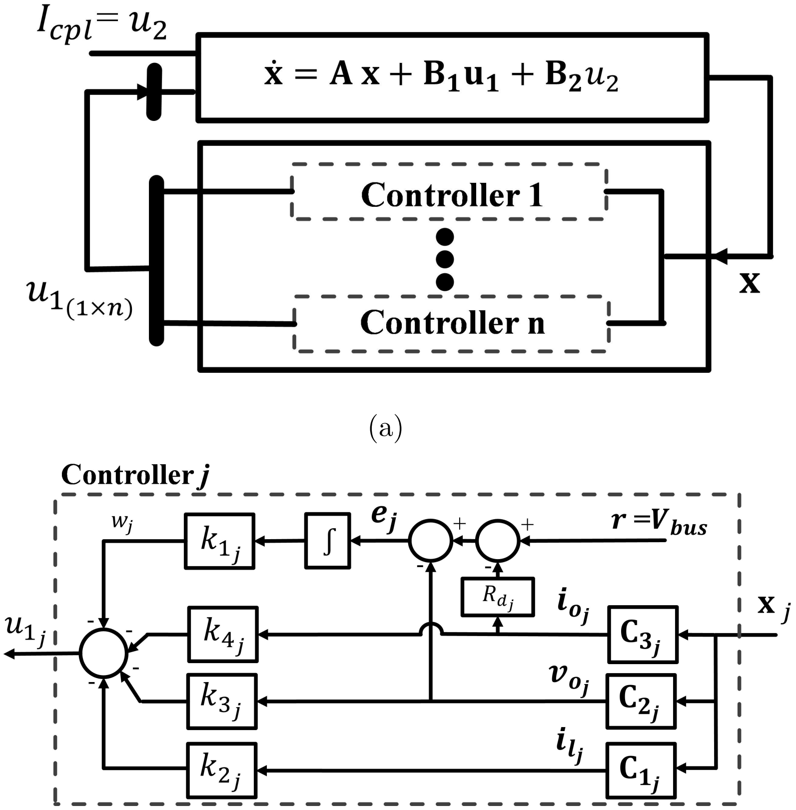

(a)

(b)

Figure 2.3: The closed-loop model of studied system: (a) System model, (b) Controller of jth converter model

where $\mathbf{C}_{e_j} = R_{d_j}\mathbf{C}_{3_j} + \mathbf{C}_{2_j}$, R_{d_j} is the droop coefficient of jth converter. $\mathbf{B}_d$ and $\mathbf{B}_r$ are:

$$\mathbf{B}_d = \begin{bmatrix} \mathbf{B}_2 \\ -\mathbf{C}_{u_1}\mathbf{B}_2 \\ \cdots \\ -\mathbf{C}_{u_n}\mathbf{B}_2 \end{bmatrix}, \quad \mathbf{B}_r = \begin{bmatrix} 0 \\ -k_{1_1} \\ \cdots \\ -k_{1_n} \end{bmatrix} \tag{2.31}$$

2.3 Weighted Dynamic Aggregation Model of Parallel DC-DC Converters

This section develops a single equivalent converter and an equivalent control system that accurately mimics the detailed model dynamics. The equivalent model demonstrated in Fig. 2.4 consists of an equivalent converter, controller and its corresponding

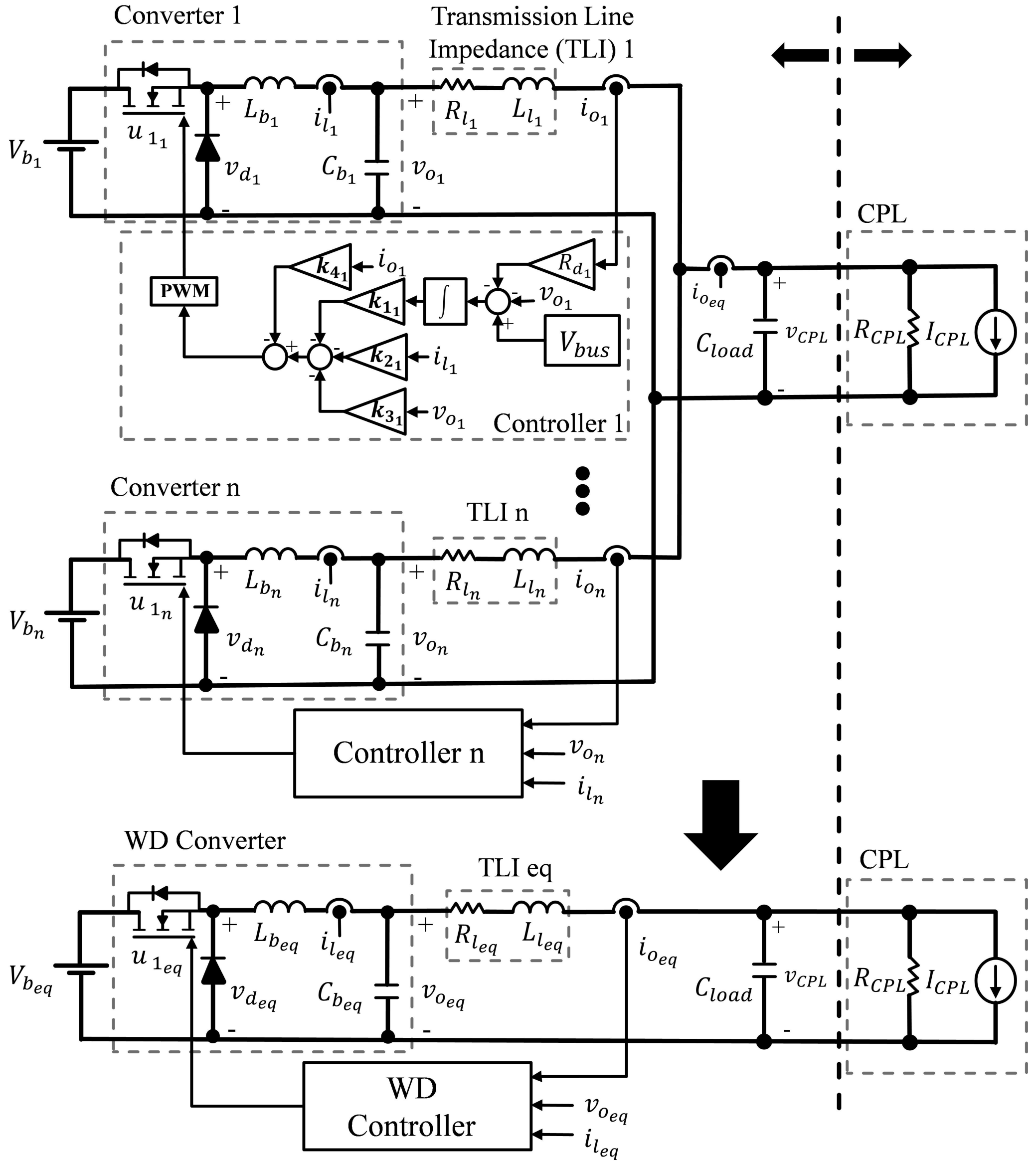

Figure 2.4: The proposed weighted dynamic aggregation (WD Agg) model of a DC microgrid with parallel converters

transmission line. The proposed equivalent WD Agg converter model should deliver $P_{WD} = \sum_{j=1}^{n} P_j$ to the load, where P_j and P_{WD} are the converter j and the WD Agg converter generated power, respectively. Because the parallel converters are connected to a single PCC bus, the contribution of each converter to the dynamic behavior of the detailed model can be determined based on the current each converter injects into the PCC bus.

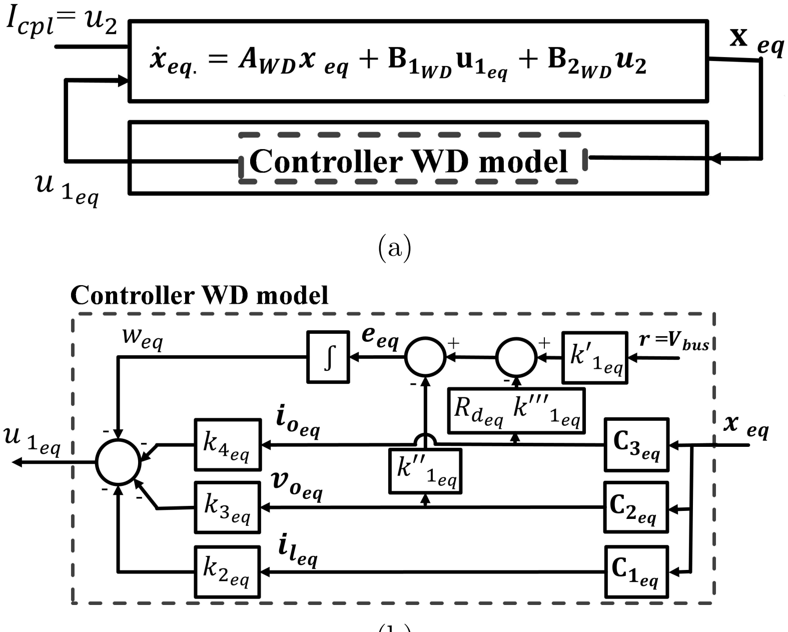

(a)

(b)

Figure 2.5: The closed-loop block diagram of WD Agg model: (a) Equivalent system model, (b) Controller of WD Agg model

2.3.1 Weighted Dynamic Aggregation Method Justification

Equivalent WD agg Converter Model

To find an equivalent converter for the detailed system, the differential equation of jth converter output current can be derived as:

$$v_{o_j} - v_{CPL} = R_{l_j} i_{o_j} + L_{l_j} \frac{di_{o_j}}{dt}. \tag{2.32}$$

Using the contribution weight of converters μ_j defined as $i_{o_{eq}} \mu_j = i_{o_j}$ in (2.32) for $j = 1, 2, ..., n$, and averaging n equations to find i_{Load} yields:

$$\sum_{j=1}^{n} \frac{v_{o_j}}{n} - v_{CPL} = \sum_{j=1}^{n} \frac{\mu_j}{n} R_{l_j} i_{o_{eq}} + \sum_{j=1}^{n} \frac{\mu_j}{n} L_{l_j} \frac{di_{o_{eq}}}{dt}, \tag{2.33}$$

where:

$$\mu_j = \frac{i_{o_j}}{i_{o_{eq}}}, \tag{2.34}$$

with $i_{o_{eq}} = \sum_{j=1}^{n} i_{o_j}$. Assuming I and $\tilde{i}$ as the steady-state and small-signal notations respectively, $\mu_j = (I_{o_j} + \tilde{i}_{o_j})/(I_{o_{eq}} + \tilde{i}_{o_{eq}}) \cong I_{o_j}/I_{o_{eq}}$. The differential equation of the equivalent converter output current can also be derived as:

$$v_{o_{eq}} - v_{CPL} = R_{l_{eq}} i_{o_{eq}} + L_{l_{eq}} \frac{di_{o_{eq}}}{dt}. \tag{2.35}$$

By comparing (2.33) and (2.35), it can be readily seen that an equivalent converter output voltage can be written as $v_{o_{eq}} = \sum_{j=1}^{n} v_{o_j}/n$, and an equivalent transmission line parameters can be calculated as:

$$R_{l_{eq}} = \sum_{j=1}^{n} \frac{\mu_j}{n} R_{l_j}, \tag{2.36}$$

$$L_{l_{eq}} = \sum_{j=1}^{n} \frac{\mu_j}{n} L_{l_j}. \tag{2.37}$$

The differential equation of jth converter output voltage can be derived as:

$$\frac{1}{C_{b_j}} i_{l_j} - \frac{1}{C_{b_j}} i_{o_j} = \frac{dv_{o_j}}{dt}. \tag{2.38}$$

Using the contribution weight of converters μ'_j defined as $i_{l_{eq}}\mu'_j = i_{l_j}$, and $i_{o_{eq}}\mu_j = i_{o_j}$ in (2.38) for $j = 1, 2, ..., n$, and summing the equations to find $i_{L_{eq}}$:

$$\frac{1}{n}\sum_{j=1}^{n} \frac{\mu'_j}{C_{b_j}} i_{l_{eq}} - \frac{1}{n}\sum_{j=1}^{n} \frac{\mu_j}{C_{b_j}} i_{o_{eq}} = \frac{1}{n}\sum_{j=1}^{n} \frac{dv_{o_j}}{dt}, \tag{2.39}$$

where $\mu'_j = i_{l_j}/i_{l_{eq}} \cong I_{l_j}/I_{l_{eq}}$ with $i_{l_{eq}} = \sum_{j=1}^{n} i_{l_j}$. The differential equation of the equivalent converter output voltage can also be derived as:

$$\frac{1}{C'_{b_{eq}}} i_{l_{eq}} - \frac{1}{C_{b_{eq}}} i_{o_{eq}} = \frac{dv_{o_{eq}}}{dt}. \tag{2.40}$$

By comparing (2.39) and (2.40), an equivalent buck capacitance can be calculated as:

$$C_{b_{eq}} = \frac{1}{\frac{1}{n}\sum_{j=1}^{n} \frac{\mu'_j}{C'_{b_j}}} = \frac{1}{\frac{1}{n}\sum_{j=1}^{n} \frac{\mu_j}{C_{b_j}}}. \tag{2.41}$$

To realize the equivalent filter capacitance by a single value, it is required $\mu'_j = \mu_j$, then $C'_{b_j} = C_{b_j}$.

The differential equation of jth converter inductance current can be derived as:

$$v_{d_j} - v_{o_j} = L_{b_j} \frac{di_{l_j}}{dt}. \tag{2.42}$$

Deriving (2.42) for $j = 1, 2, ..., n$, and summing the equations to find $i_{L_{eq}}$:

$$\sum_{j=1}^{n} \frac{v_{d_j}}{n} - \sum_{j=1}^{n} \frac{v_{o_j}}{n} = \sum_{j=1}^{n} \frac{\mu_j}{n} L_{b_j} \frac{di_{l_{eq}}}{dt}, \tag{2.43}$$

The differential equation of the equivalent converter inductance current can also be derived as:

$$v_{d_{eq}} - v_{o_{eq}} = L_{b_{eq}} \frac{di_{l_{eq}}}{dt}. \tag{2.44}$$

By comparing (2.43) and (2.44), an equivalent buck inductance and $v_{d_{eq}}$can be calculated as:

$$L_{b_{eq}} = \sum_{j=1}^{n} \frac{\mu_j}{n} L_{b_j}, \tag{2.45}$$

$$v_{d_{eq}} = \sum_{j=1}^{n} \frac{v_{d_j}}{n}. \tag{2.46}$$

Equivalent WD agg Controller Model

The differential equation of jth controller shown in Fig. 2.3 can be derived as:

$$v_{d_j} = (-k_{2_j} i_{l_j} - k_{3_j} v_{o_j} - k_{4_j} i_{o_j} - w_j) v_{b_j}, \tag{2.47}$$

with:

$$w_j = \int (V_{bus} - v_{o_j} - R_{d_j} i_{o_j}) k_{1_j} dt. \tag{2.48}$$

Deriving (2.47) for $j = 1, 2, ..., n$, and summing the equations to find equivalent controller parameters:

$$\sum_{j=1}^{n} \frac{v_{d_j}}{n} = (-\sum_{j=1}^{n} \frac{k_{2_j}}{n} \mu_j \gamma_j i_{l_{eq}} - \sum_{j=1}^{n} \frac{k_{3_j}}{n} \alpha_j \gamma_j v_{o_{eq}} - \sum_{j=1}^{n} \frac{k_{4_j}}{n} \mu_j \gamma_j i_{o_{eq}} - \sum_{j=1}^{n} \frac{w_j}{n} \gamma_j) V_{b_{eq}}, \tag{2.49}$$

where $\alpha_j = v_{o_j}/v_{o_{eq}} \cong V_{o_j}/V_{o_{eq}}$, $V_{o_{eq}} = \sum_{j=1}^{n} v_{o_j}/n$, $\gamma_j = V_{b_j}/V_{b_{eq}}$, and $V_{b_{eq}} = \sum_{j=1}^{n} V_{b_j}/n$. By substituting (2.48) in (2.49):

$$\sum_{j=1}^{n} w_j \gamma_j = \int (V_{bus} \sum_{j=1}^{n} \gamma_j k_{1_j} - \sum_{j=1}^{n} \alpha_j \gamma_j k_{1_j} v_{o_{eq}} - \sum_{j=1}^{n} \beta_j \mu_j \gamma_j k_{1_j} R_{d_{eq}} i_{o_{eq}}) dt, \tag{2.50}$$

where $\beta_j = R_{d_j}/R_{d_{eq}}$. $R_{d_{eq}}$ is the equivalent droop resistance of WD Agg model, which can be calculated by writing the KVL equation of the system in terms of the equivalent output voltage and output current as:

$$R_{d_{eq}} = \frac{V_{bus} - V_{o_{eq}}}{I_{o_{eq}}}. \tag{2.51}$$

The differential equation of the equivalent controller shown in Fig. 2.5 can also be derived as:

$$\frac{v_{d_{eq}}}{V_{b_{eq}}} = -k_{2_{eq}} i_{l_{eq}} - k_{3_{eq}} v_{o_{eq}} - k_{4_{eq}} i_{o_{eq}} - w_{eq}, \tag{2.52}$$

where:

$$w_{eq} = \int (V_{bus} k'_{1_{eq}} - k''_{1_{eq}} v_{o_{eq}} - k'''_{1_{eq}} R_{d_{eq}} i_{o_{eq}}) dt. \tag{2.53}$$

By comparing (2.49) and (2.52), an equivalent controller parameters k_{2_j}, k_{3_j} and k_{4_j} can be calculated as:

$$k_{2_{eq}} = \sum_{j=1}^{n} \frac{\mu_j \gamma_j k_{2_j}}{n}, \quad k_{3_{eq}} = \sum_{j=1}^{n} \frac{\alpha_j \gamma_j k_{3_j}}{n}, \quad k_{4_{eq}} = \sum_{j=1}^{n} \frac{\mu_j \gamma_j k_{4_j}}{n}. \tag{2.54}$$

Also by comparing (2.50) and (2.53), an equivalent controller parameters k'_{1_j}, k''_{1_j} and k'''_{1_j} can be calculated as:

$$k'_{1_{eq}} = \sum_{j=1}^{n} \frac{\gamma_j k_{1_j}}{n}, \quad k''_{1_{eq}} = \sum_{j=1}^{n} \frac{\alpha_j \gamma_j k_{1_j}}{n}, \quad k'''_{1_{eq}} = \sum_{j=1}^{n} \frac{\beta_j \mu_j \gamma_j k_{1_j}}{n}. \tag{2.55}$$

Based on the above equations, it can be concluded that the equivalent reduced-order converter parameters can be calculated by weighted averaging of corresponding parameters of the detailed system using the obtained weights. As (2.34) shows, the weight of jth converter is the ratio of the jth output current to the summation of all output currents.

2.3.2 Equivalent Parameters

To find the equivalent parameters of WD Agg converter and its corresponding controller, the weights of jth converter α_j, β_j, γ_j, and μ_j should be calculated. The

Table 2.1: The converters' weights and proposed WD Agg converter parameters

Parameter	**Value**	**Parameter**	**Value**
α_j	$V_{o_j}/V_{o_{eq}}$	$R_{d_{eq}}$	$(V_{bus} - V_{o_{eq}})/I_{o_{eq}}$
β_j	$R_{d_j}/R_{d_{eq}}$	$V_{b_{eq}}$	$\sum_{j=1}^{n} V_{b_j}/n$
μ_j	$\frac{1}{R_{d_j}+R_{l_j}}/\sum_{j=1}^{n} \frac{1}{R_{d,j}+R_{l_j}}$	$k'_{1_{eq}}$	$\sum_{j=1}^{n} \gamma_j k_{1_j}/n$
γ_j	$V_{b_j}/V_{b_{eq}}$	$k''_{1_{eq}}$	$\sum_{j=1}^{n} \alpha_j \gamma_j k_{1_j}/n$
$R_{l_{eq}}$	$\sum_{j=1}^{n} \mu_j R_{l_j}/n$	$k'''_{1_{eq}}$	$\sum_{j=1}^{n} \beta_j \mu_j \gamma_j k_{1_j}/n$
$L_{l_{eq}}$	$\sum_{j=1}^{n} \mu_j L_{l_j}/n$	$k_{2_{eq}}$	$\sum_{j=1}^{n} \mu_j \gamma_j k_{2_j}/n$
$L_{b_{eq}}$	$\sum_{j=1}^{n} \mu_j L_{b_j}/n$	$k_{3_{eq}}$	$\sum_{j=1}^{n} \alpha_j \gamma_j k_{3_j}/n$
$C_{b_{eq}}$	$n/\sum_{j=1}^{n} \frac{\mu_j}{c_{b_j}}$	$k_{4_{eq}}$	$\sum_{j=1}^{n} \mu_j \gamma_j k_{4_j}/n$

steady-state output voltage of converters will be equal to V_{ref}. Substituting (2.1) in (2.32) and calculating the steady-state output current:

$$i_{o_j}(s) = \frac{V_{CPL}(s)}{R_{d_j} + R_{l_j}}. \tag{2.56}$$

Therefore, the output current ratio of converter j to the load output current can be calculated by rewriting (2.56) for $j = 1, 2, ..., n$:

$$\mu_j = \frac{I_{o_j}}{I_{o_{eq}}} = \frac{\frac{1}{R_{d_j}+R_{l_j}}}{\sum_{j=1}^{n} \frac{1}{R_{d_j}+R_{l_j}}}, \tag{2.57}$$

where μ_j represents the contribution of the jth converter to the incremental changes in the load. Also, other weights can be calculated as $\alpha_j = V_{o_j}/V_{o_{eq}} \simeq 1$, $\beta_j = R_{d_j}/R_{d_{eq}}$, and $\gamma_j = V_{b_j}/V_{b_{eq}}$ based on the system parameters. Therefore, the equivalent unit parameters can be calculated using the weighted averaging of the unit parameters using the corresponding weights shown in Table 2.1.

2.3.3 Final Proposed Equivalent WD Closed loop System Model

The closed-loop state-space model of the weighted dynamic model can be shown by:

$$\begin{bmatrix} \dot{\mathbf{x}}_{eq} \\ \dot{u}_{1_{eq}} \end{bmatrix} = \mathbf{A}_{WD} \begin{bmatrix} \mathbf{x}_{eq} \\ u_{1_{eq}} \end{bmatrix} + \begin{bmatrix} \mathbf{B}_2 \\ -\mathbf{C}_{u_{eq}} \mathbf{B}_2 \end{bmatrix} u_2 + \begin{bmatrix} 0 \\ k'_{1_{eq}} \end{bmatrix} r, \tag{2.58}$$

where $\mathbf{x}_{eq} = \begin{bmatrix} i_{l_{eq}} & v_{o_{eq}} & i_{o_{eq}} & v_{cpl} \end{bmatrix}^T$ and $\mathbf{A}_{WD(5\times5)}$ is:

$$\mathbf{A}_{WD} = \begin{bmatrix} \mathbf{A} & \mathbf{B}_1 \\ -\mathbf{C}_{e_{eq}} - \mathbf{C}_{u_j}\mathbf{A} & -\mathbf{C}_{u_{eq}}\mathbf{B}_1 \end{bmatrix}, \tag{2.59}$$

where $\mathbf{A}$ and $\mathbf{B}_1$ are:

$$\mathbf{A} = \begin{bmatrix} 0 & \frac{-1}{L_{beq}} & 0 & 0 \\ \frac{1}{c_{beq}} & 0 & \frac{-1}{c_{beq}} & 0 \\ 0 & \frac{1}{L_{leq}} & \frac{-R_{leq}}{L_{leq}} & \frac{-1}{L_{leq}} \\ 0 & 0 & \frac{1}{C_{load}} & \frac{-1}{R_{cpl}C_{load}} \end{bmatrix}, \mathbf{B}_1 = \begin{bmatrix} \frac{V_{beq}}{L_{beq}} \\ 0 \\ 0 \\ 0 \end{bmatrix}, \mathbf{B}_2 = \begin{bmatrix} 0 \\ 0 \\ 0 \\ \frac{-1}{C_{load}} \end{bmatrix}. \tag{2.60}$$

Also, $\mathbf{C}_{u_{eq}}$ is:

$$\mathbf{C}_{u_{eq}} = -k_{2_{eq}}\mathbf{C}_{1_{eq}} - k_{3_{eq}}\mathbf{C}_{2_{eq}} - k_{4_{eq}}\mathbf{C}_{3_{eq}}, \tag{2.61}$$

where $i_{l_{eq}} = \mathbf{C}_{1_{eq}} \times \mathbf{x}_{eq}$, $v_{o_{eq}} = \mathbf{C}_{2_{eq}} \times \mathbf{x}_{eq}$, $i_{o_{eq}} = \mathbf{C}_{3_{eq}} \times \mathbf{x}_{eq}$. $k_{2_{eq}}$, $k_{3_{eq}}$ and $k_{4_{eq}}$ are the equivalent controller coefficients of WD Agg converter shown in Fig. 2.5. Also $\mathbf{C}_{e_{eq}}$ is:

$$\mathbf{C}_{e_{eq}} = k'''_{1_{eq}} R_{d_{eq}} \mathbf{C}_{3_{eq}} + \mathbf{k}''_{1_{eq}} C_{2_{eq}}. \tag{2.62}$$

Moreover, the equivalent controller parameters of the proposed WD Agg converter can be determined by the weighted averaging of the converters' controller parameters calculated in (2.54) and (2.55). Consequently, (2.58) can be used as a reduced-order model of the detailed system to study the stability and sensitivity of the system in various power systems.

2.4 Results and Discussion

To evaluate the proposed WD model, the detailed and the reduced-order model of three paralleled converters connected to a CPL shown in Fig. 2.1 is studied in various experimental and simulation scenarios. These scenarios consist of unequal parameters and conditions for the paralleled converters for a realistic and challenging study. The system parameters can be found in Table 2.2. The results are discussed in two parts. The first part evaluates the proposed model accuracy in the stability analysis by

Table 2.2: The studied system specifications

Parameter	Value	Parameter	Value
$V_{bus}(V)$	80	R_{load} (Ω)	16
P_{load} (W)	200	C_{load} (μF)	390
$V_{b_1}, ..., V_{b_3}$ (V)	100,100,100	$R_{l_1}, ..., R_{l_3}$ (Ω)	0.163, 0.113, 0.118
$L_{l_1}, ..., L_{l_3}$ (mH)	1.2, 1, 0.9	$L_{b_1}, ..., L_{b_3}$ (mH)	2.2, 1.8, 1.9
$C_{b_1}, ..., C_{b_3}$ (μF)	2.3, 2.7, 2.5	$R_{d_1}, ..., R_{d_3}$	0.6, 1.35, 0.7
$k_{1_1}, ..., k_{1_3}$	0.08, 0.08, 0.08	$k_{2_1}, ...k_{2_3}$	0.1478, 0.1478, 0.1478
$k_{3_1}, ..., k_{3_3}$	0.0012, 0.0012, 0.0012	$k_{4_1}, ..., k_{4_3}$	-0.1213, -0.1213, -0.1213
l_{cpl} $(mH\ )$	2.2	C_{cpl} (μF)	2.5
k_{PI_1}	P=0.0005, I=0.05	k_{PI_2}	P=0.1, I=1

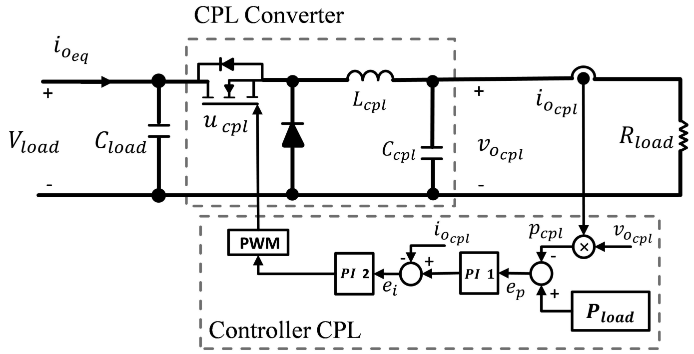

Figure 2.6: CPL converter and controller

analyzing the bode diagram, the root locus plot, and the trajectory of closed-loop eigenvalues with various converter parameters. The second part compares the steady-state and transient behavior of the detailed system with the proposed model at the startup and under two step changes in the CPL reference power shown in Fig. 2.6.

2.4.1 Closed-loop System Stability and Eigenvalue Analysis

To assess the proposed method throughout different frequencies, the bode diagrams of the detailed, WD Agg, MTS, and Tahim models are plotted in Fig. 2.7 for both open-loop and closed-loop systems. Figure 2.7 only presents the closed-loop response of MTS and Tahim models because an ideal voltage source and an impedance are considered as the converter and its corresponding controller in MTS and Tahim models. Fig. 2.7 demonstrates the WD Agg model's superiority in mimicking the detailed

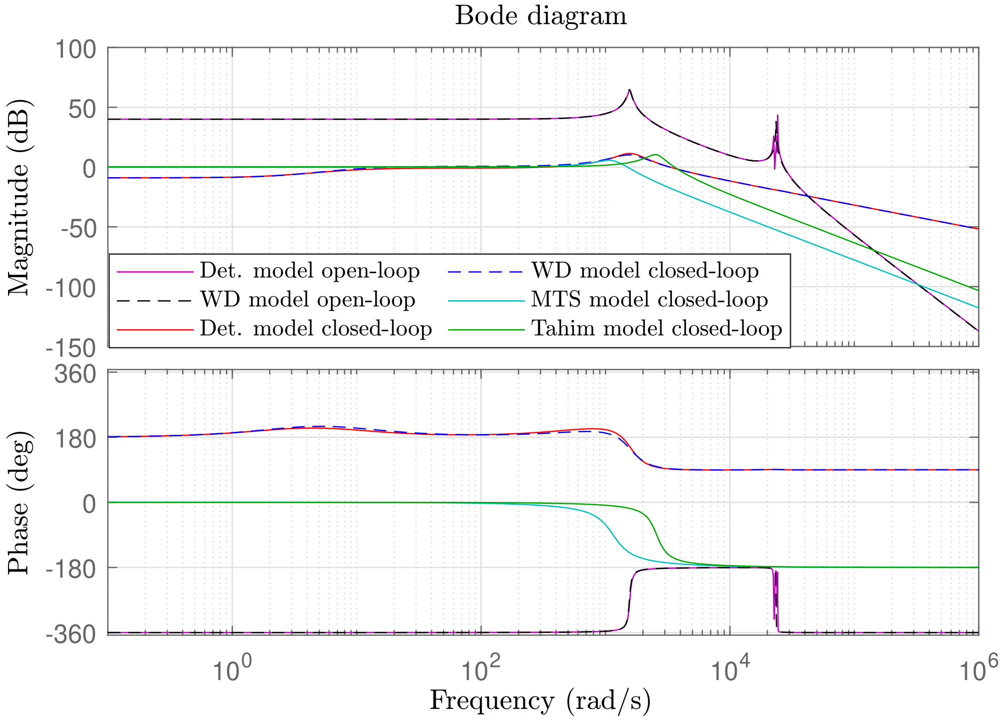

Figure 2.7: Bode diagram comparison of the Detailed model, WD Agg model, MTS model, and Tahim model

model's frequency response compared to the other existing models.

To study the system's stability through variation of feedback controller parameters, the root locus plot of the detailed model, WD Agg model, MTS model and Tahim model are plotted in Fig. 2.8. Root locus plots can be used for designing controller parameters and filter. According to Fig. 2.8, the WD Agg model replicates the root locus trajectory of the detailed model more accurately, whereas the MTS and Tahim models are independent of control parameters. Moreover, Fig. 2.8 shows that a weighted average of the corresponding roots in the detailed model provides an equivalent root in WD Agg model.

Controller parameters can significantly impact the system stability; therefore, the trajectory of the closed-loop eigenvalues of the system with variation of k_{2_j} and k_{4_j} values are plotted in Fig. 2.9 and Fig. 2.10, respectively. Fig. 2.9 shows the trajectory of the eigenvalues of the closed-loop system with $k_{2_j} = 0.05$ to 0.3 and it reveals

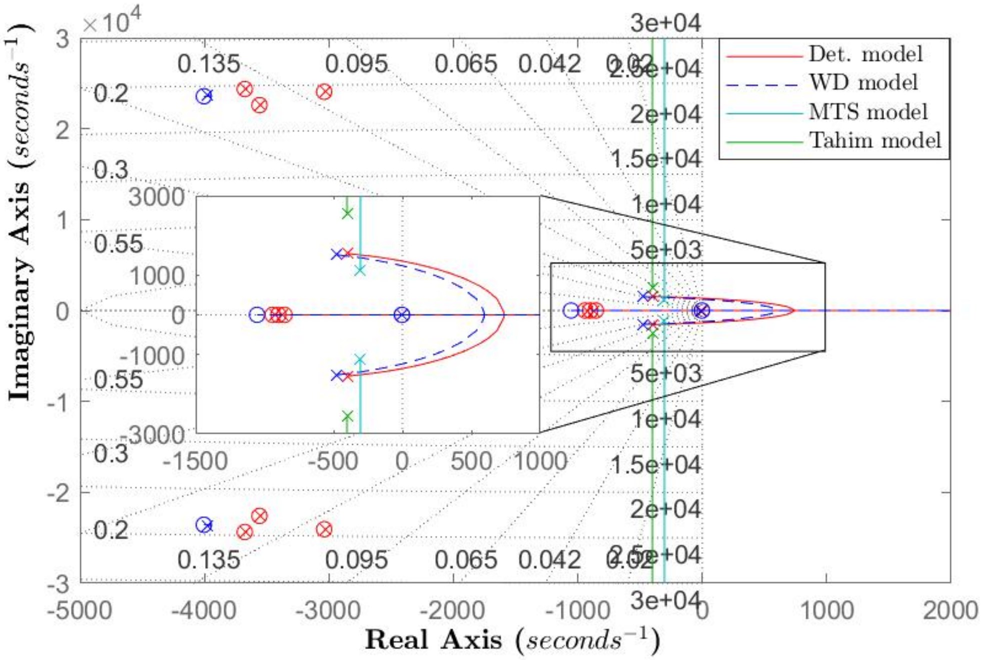

Figure 2.8: Root locus diagram of Detailed model, WD Agg model, MTS model, and Tahim model

that the system becomes stable for k_{2_j} values greater than 0.123 for both detailed and WD Agg models. Likewise, the trajectory of the closed-loop eigenvalues of the system with $k_{4_j} = -0.001$ to -0.4 is plotted in Fig. 2.10. Considering both detailed and WD Agg models, Fig. 2.10 shows that the system becomes unstable at k_{4_j} values smaller than -0.145. Hence, the proposed aggregated model can be used to tune the gain of the converters and to achieve a stable and optimal performance.

Similarly, the impact of other system parameters on stability can also be explored. For instance, Fig. 2.11 shows the trajectory of closed-loop eigenvalues of the system with changing C_{load} from $1\mu F$ to $1mF$. As shown, the system moves toward instability if C_{load} is smaller than $37.5\mu F$. Thus, the result of Fig. 2.11 can be used to develop a suitable filter for the load. The eigenvalue trajectory of the WD Agg model, presented in Figs. 2.9 to 2.11 correlates with the corresponding eigenvalue trajectory of the detailed model, which validates the accuracy of the WD Agg model in eigenvalue analysis.

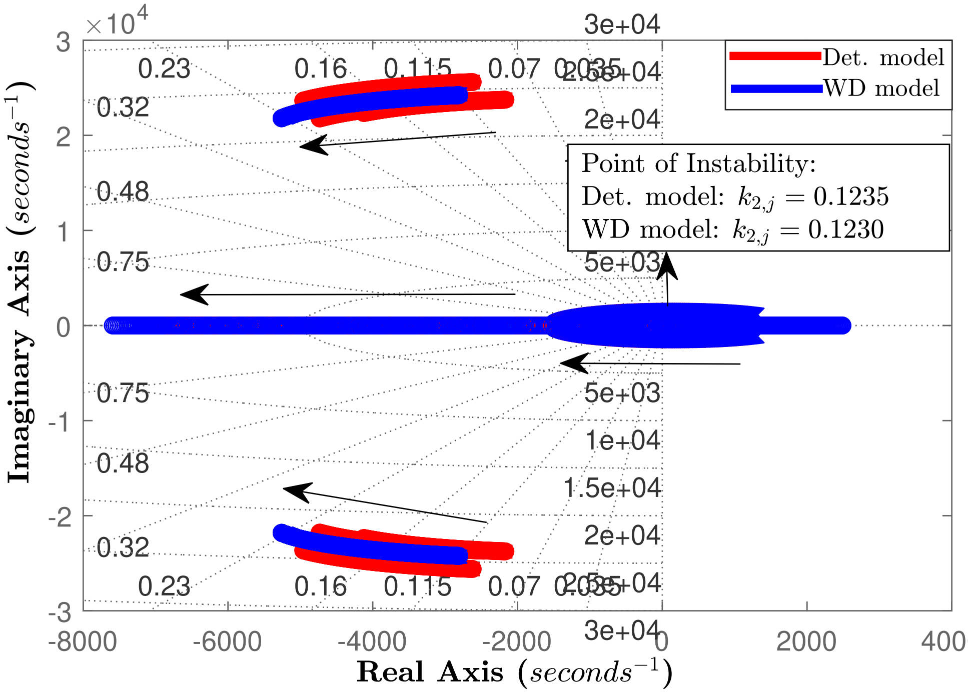

Figure 2.9: Closed-loop eigenvalues comparison of the detailed and the proposed WD Agg models with $k_{2_j} = 0.05$ to 0.3

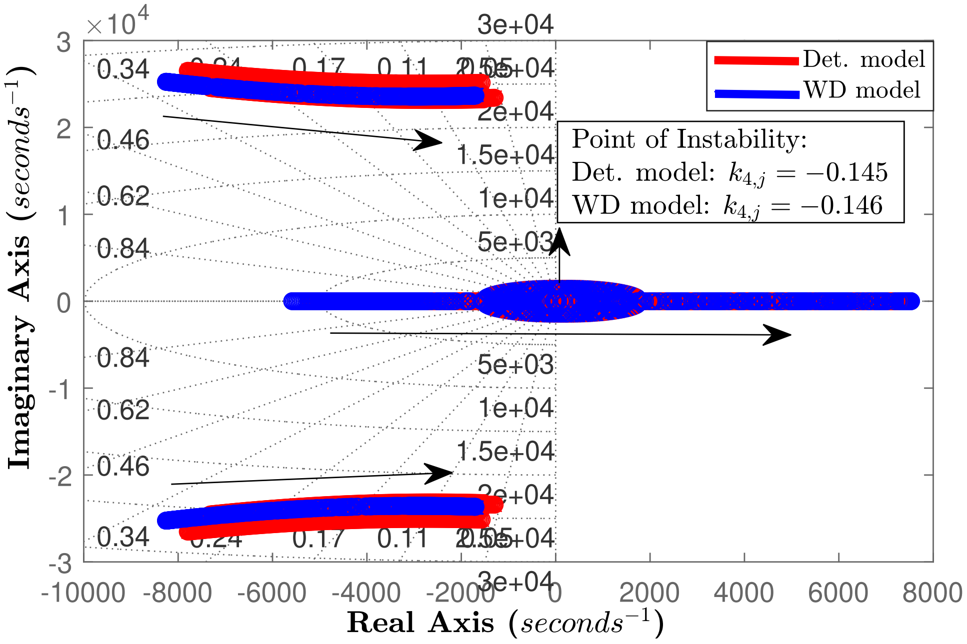

Figure 2.10: Closed-loop eigenvalues comparison of the detailed and the proposed WD Agg models with $k_{4_j} = -0.001$ to -0.4

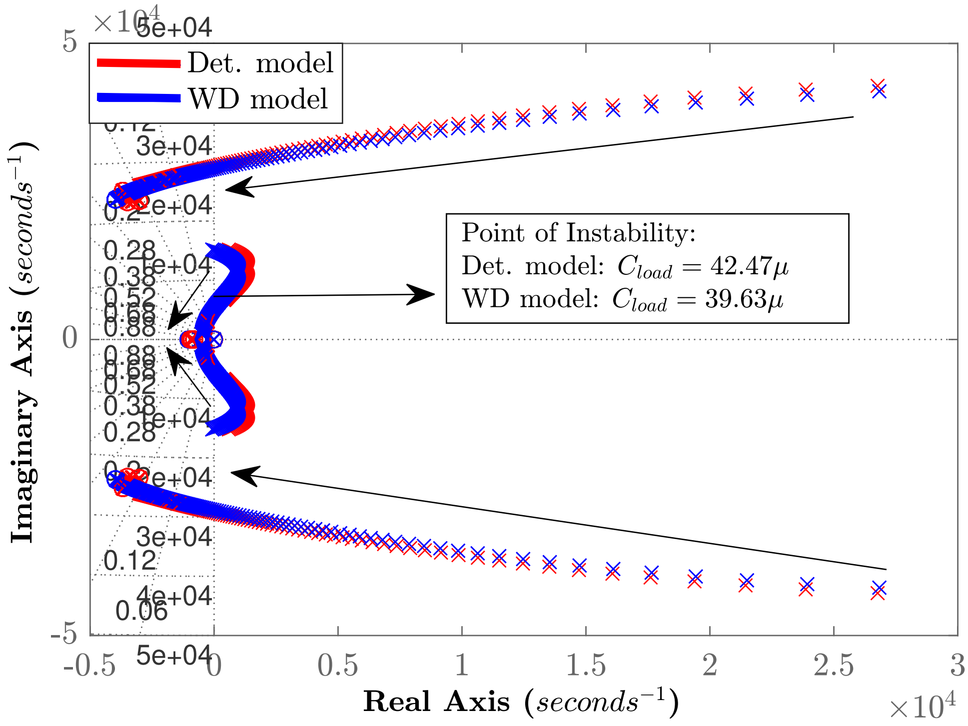

Figure 2.11: Closed-loop eigenvalues comparison of the detailed and the proposed WD Agg models with $C_{load} = 1\mu F$ to $1mF$

Table 2.3: Experimental Parameters

	Exp. 4	*Exp.* 5	*Exp.* 6
$V_{b_1}, ..., V_{b_3}$	100,100,100	100,100,100	120,110,100
$k_{1_1}, ..., k_{1_3}$	0.08,0.08,0.08	0.08,0.12,0.096	0.08,0.11,0.96
$k_{2_1}, ..., k_{2_3}$	0.1692, 0.1854, 0.1525		
$k_{3_1}, ..., k_{3_3}$	0.0008, 0.0012, 0.0010		
$k_{4_1}, ..., k_{4_3}$	-0.1233, -0.1437, -0.1381		

2.4.2 Steady-State and Transient Behavior Comparison

To evaluate the performance of the proposed WD Agg model, an islanded DC microgrid with three parallel buck converters connected to a CPL is built. System parameters are defined in Table 2.2, and the system is shown in Fig. 2.12. Experimental and simulation results of the steady-state and transient behavior of the output current and voltage of the parallel buck converters are plotted in Figs. 2.13 to 2.18.

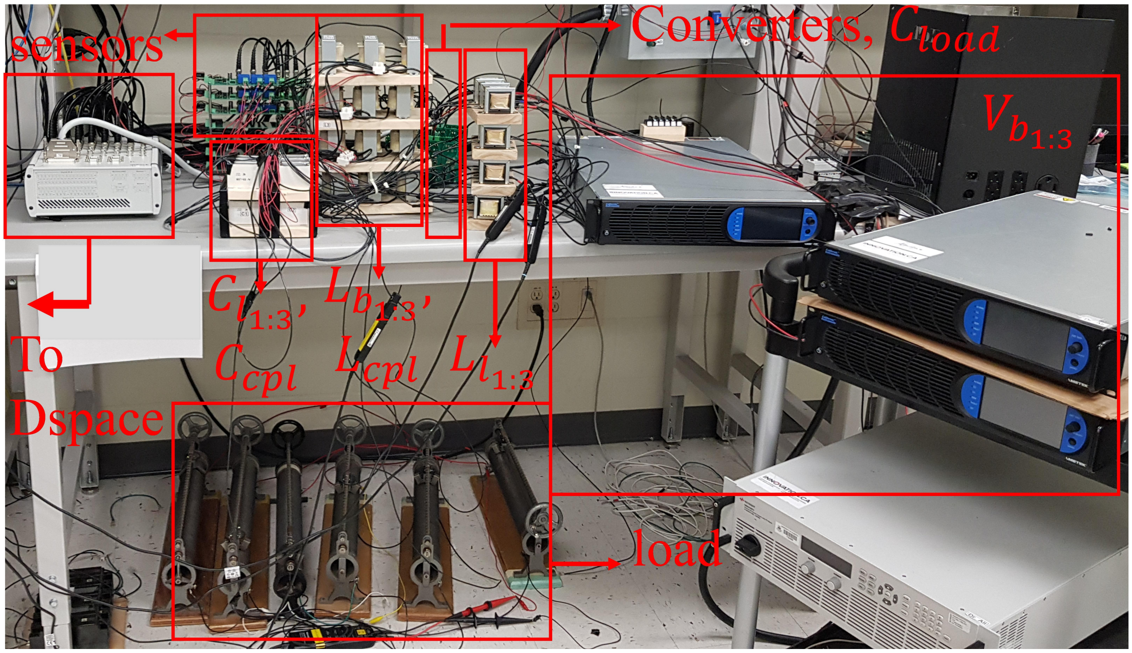

Figure 2.12: Experimental setup of the three parallel buck converters connected to CPL

Figure 2.13a demonstrates the experimental and simulation results of the output current and voltage at the start-up and load power change from 200w to 250w at t=7.8s for the detailed model and simulated WD Agg model. To evaluate the WD Agg model performance, the aforementioned steady-state and transient behavior of the simulated detailed model and WD Agg model is compared to the corresponding MSM and Tahim model results in Fig. 2.13b. As shown, the output currents of the MSM and Tahim models are discontinuous due to modeling the converters with a voltage source and an impedance.

The variable error with respect to the detailed system is shown in Fig. 2.14. An error index is defined as the integral of the error value between the reduced-order model and the detailed system responses:

$$EI = \left| \int_{t=t_0}^{t=t_1} (F_{\text{detailed}} - F_{\text{model}})\, dt \right|, \tag{2.63}$$

where F can be any response curve. The EI is calculated for I_{CPL}, $I_{o_{eq}}$, v_{CPL}, $V_{o_{eq}}$, and power P for all methods between $t_0 = 1$ to $t_1 = 12$. The results are listed

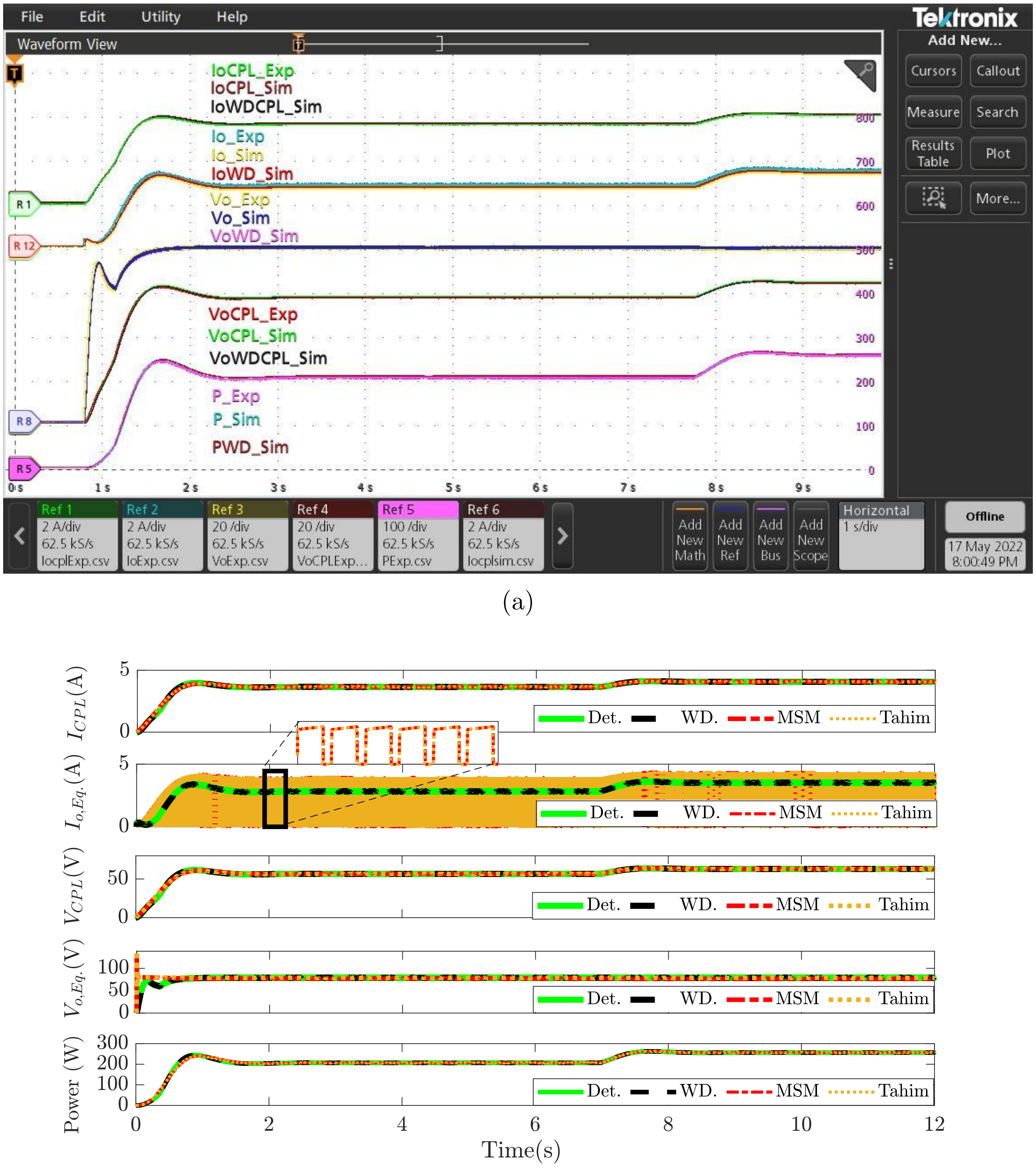

(a)

(b)

Figure 2.13: Exp. 1: Steady-state and transient behavior comparison of (a) experimental and simulation detailed model and WD Agg model (b) simulation detailed model, WD Agg model, MSM model, and Tahim model at the start-up and load power changes from 200W to 250W

in Table. 2.4, which shows that the WD Agg model provides at least 12 times more accurate output CPL voltage. Figures 2.13 and 2.14 indicate that the WD Agg model

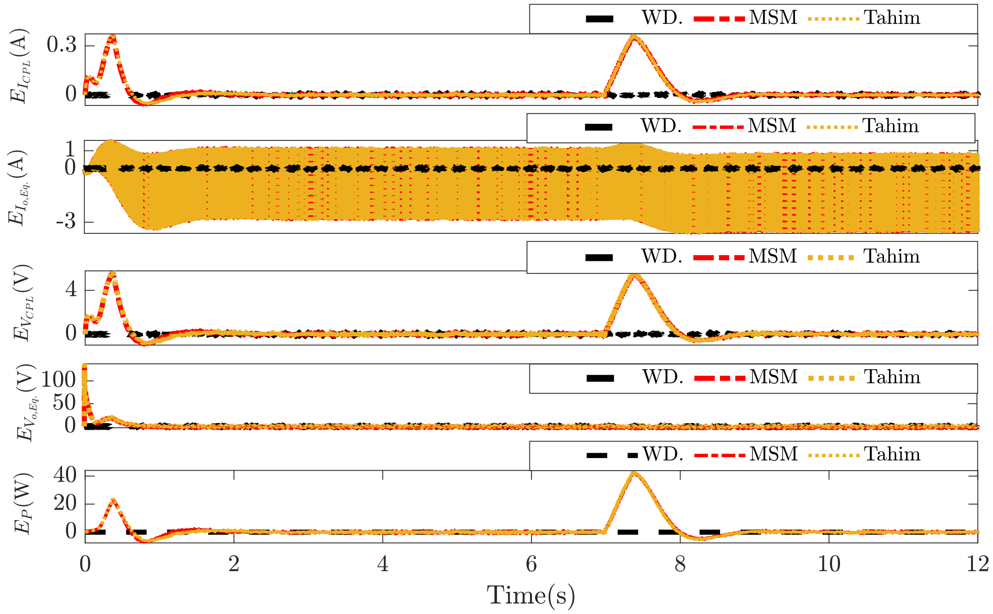

Figure 2.14: Exp.1: Steady-state and transient response variable error comparison with respect to the detailed system

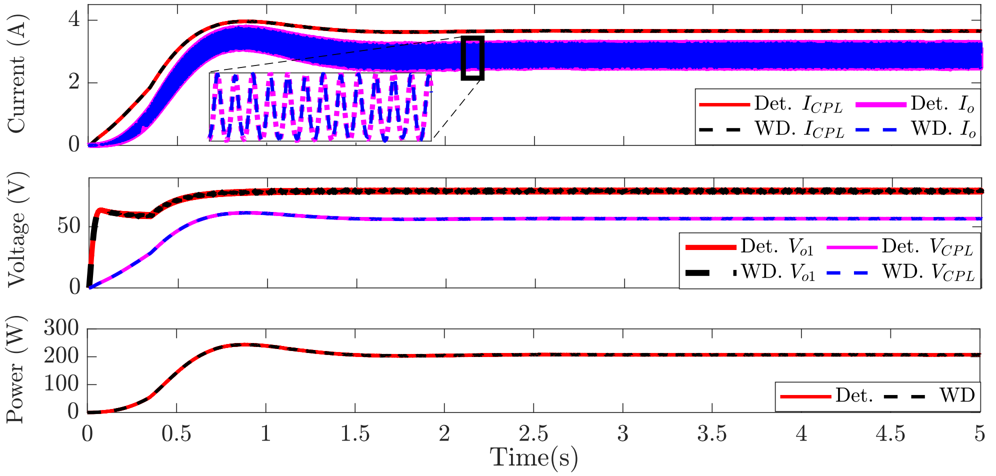

Figure 2.15: Steady-state and transient behavior of the simulation detailed and WD Agg models at the start-up with $C_{load} = 1\mu F$

is more accurate than the MSM and Tahim models at reproducing the behavior of the detailed model in steady-state and during transients at the start-up duration and load power changes.

To evaluate the behavior of the WD Agg model in an unstable condition, the detailed and WD Agg model are simulated with $C_{load} = 1\mu F$ at the start-up shown

Table 2.4: Calculated error indexes for I_{CPL}, $I_{o_{eq}}$, V_{CPL}, $V_{o_{eq}}$, and power P

Error Index	I_{CPL}	$I_{o_{eq}}$	v_{CPL}	$V_{o_{eq}}$	P
EI_{WD}	0	0	1.1	0.003	0
EI_{Tahim}	1.52	24.52	29.87	8.1	60
EI_{MSM}	1.51	24.36	14.15	7.9	57

in Fig. 2.15. As shown in Fig. 2.11, system becomes unstable for C_{load} values smaller than $37.5\mu F$. Fig. 2.15 shows that the WD Agg model resembles the steady-state and transient behavior of the detailed model in unstable conditions.

To assess the WD Agg model with different response times through load power changes from 200W to 250W and from 250W to 300W, the steady-state and transient results of the experimental and simulation detailed model are compared to the respective WD Agg model results in Figure 2.16 for $k_{1_j} = 0.04, 0.32$ with $j = 1, 2, 3$. The results obtained with various k_{1_j} values indicate that higher gains lead the system toward a faster response but lower stability margin. As shown in Fig. 2.13 to 2.16, when the controller parameters of paralleled converters are the same, the simulated WD Agg model results match the detailed model experimental and simulation results at the start-up and with various k_{1_j} and C_{load} parameters.

To study the behavior of the proposed WD Agg model for the system with unequal control parameters, the updated system parameters outlined in Table 2.3 are used in experiments 4 to 6. In the fourth experiment, unequal k_{2_j}, k_{3_j}, and k_{4_j} parameters are used for the paralleled converters, and the results are shown in Fig. 2.17a for the load power change from 200W to 250W at t=8.5s. As shown in Fig. 2.16, k_{1_j} affects the response behavior of the jth converter output voltage more significantly because k_{1_j} controls the tracking error of the system shown in Fig. 2.3. thus, the steady-state and transient behavior of the load voltage with unequal k_{1_j} is plotted in Fig. 2.17b.

In Exp. 5, all the control parameters of the parallel converters are unequal, and the results are shown for the following load power changes from 200W to 250W at t=8.5s and from 250W to 300W at t=14.5s. Figure 2.17 suggests that the steady-state and

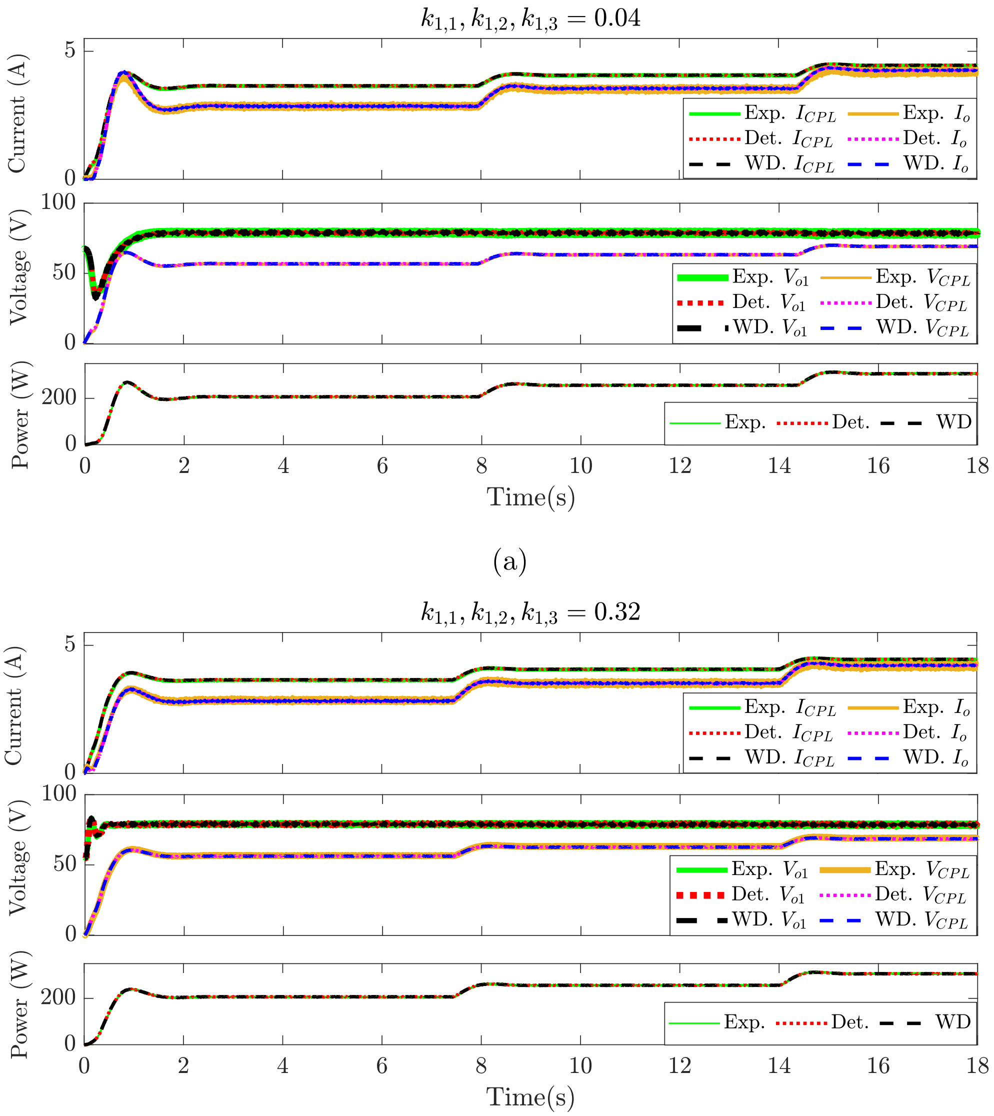

(a)

(b)

Figure 2.16: Exp. 2 and 3: Steady-state and transient results of the experimental and simulation detailed model and WD Agg model with (a) $k_{1_j} = 0.04$ (b) $k_{1_j} = 0.32$ for $j = 1, 2, 3$

transient results of the WD Agg model mimic the behavior of the detailed model in both experimental and simulation results for the system with unequal converters and control parameters.

To make the system more realistic and challenging, different input voltages are assumed for Exp. 6. Fig. 2.18 shows the steady-state and transient behavior of the experimental and simulation detailed and WD Agg models with unequal input volt-

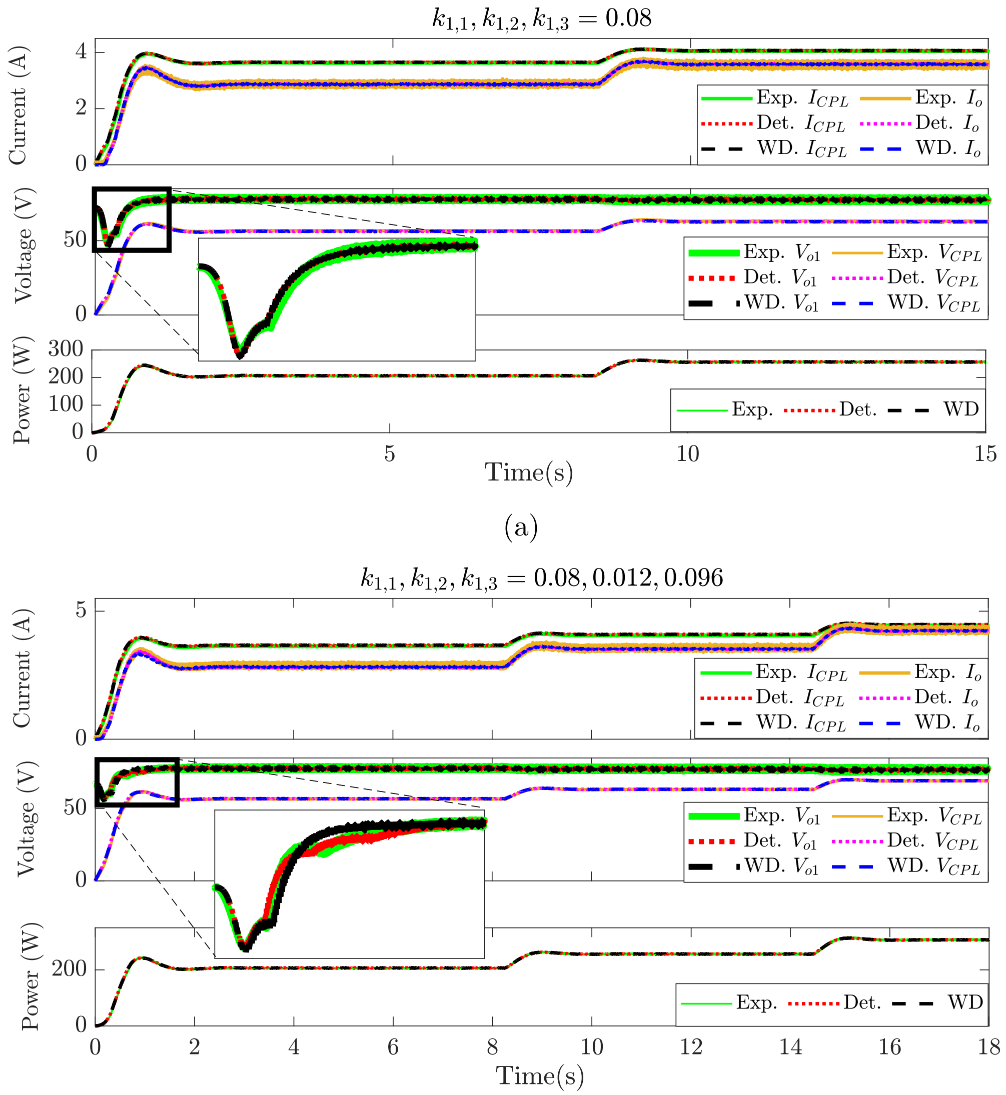

(a)

(b)

Figure 2.17: Exp. 4 and 5: Steady-state and transient results of the experimental and simulation detailed model and WD Agg model with unequal control parameters (a) except k_{1_j} and (b) including $k_{1,j}$

ages $V_{b_1}, V_{b_2}, V_{b_3} = 120, 110, 100$ and unequal control parameters for the load power change from 200W to 250W at t=4.5s. The results shown in Fig. 2.16 to 2.18 verify the WD Agg model performance accuracy in the steady-state and transient behavior for the system with unequal converter, controller, and input voltage parameters.

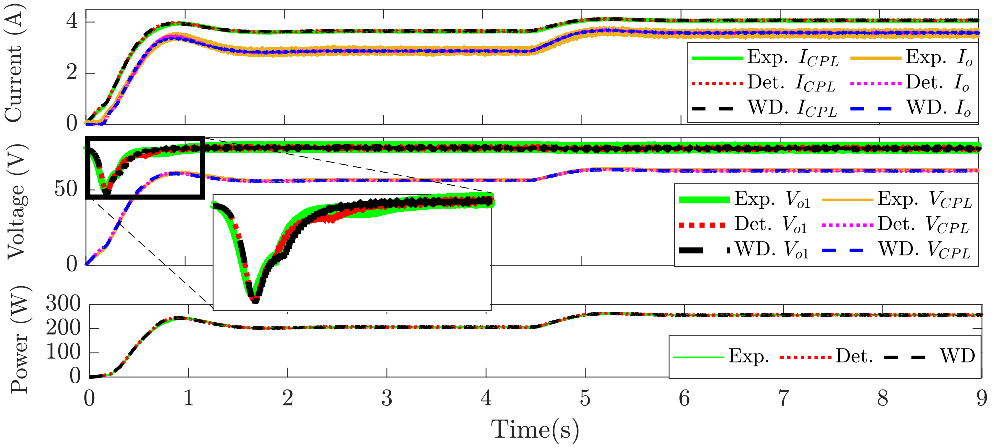

Figure 2.18: Exp. 6: Steady-state and transient results of the experimental and simulation detailed and WD Agg models with unequal control parameters including k_{1_j}, and unequal input voltages $V_{b_1}, V_{b_2}, V_{b_3} = 120, 110, 100$

2.5 Conclusions

The WD Agg model is presented in this chapter to reduce the complexity and computational burden of studying n droop controlled DC-DC converters in islanded microgrids. The converters are paralleled at a PCC bus and can have equal and unequal parameters values. The proposed WD Agg model provides an equivalent single converter, controller, and transmission line model as a reduced-order model of the detailed system. The equivalent parameters of the system are derived by weighted averaging of detailed model parameters, where the weight of each converter is quantified based on the contribution of that converter's dynamic behaviour to the detailed model's overall dynamic behaviour. The proposed model is evaluated by analyzing three paralleled buck converters connected to a CPL in various scenarios, including varied control parameters, different output filter capacitance, unequal converter and controller parameters, and unequal input voltages. The comparison results are discussed in two sections: eigenvalue analysis and steady-state and transient behavior comparison. The bode diagrams, root locus, and eigenvalue trajectories of the system with different control parameters and output filter capacitance verify the accuracy of the WD Agg model in stability analysis, sensitivity analysis, and designing a proper filter for the load. The detained results from the experimented setup and simulation verify the accuracy of the proposed WD Agg model with unequal converter and controller parameters and input voltages in steady-state and transient behavior of the system at the start-up and CPL power changes. It is shown that the error of the proposed WD agg method is at least 12 times less than Tahim and MSM models. Based on the simulation and experimental results, the WD Agg model can readily be used in stability analysis, sensitivity analysis, and designing studies in parallel DC-DC power systems.

Chapter 3

Doubly-Fed Induction Generator Based Wind Farm Analysis and Design

3.1 Introduction

Nowadays, wind power is one of the promising renewable energy sources that is mainly used to generate electricity. Wind Turbine Generators (WTGs) capture wind energy using aerodynamic blades and convert it into mechanical power by rotating the shaft inside the nacelle. To convert power effectively, the tip speed of the blade is required to be less than half of the sound speed. Therefore, the rotational speed will decrease when the diameter of the blade increases. This phenomenon might result in bulky generators, which increase the installation costs. Employing a gearbox is one of the most weight-efficient solutions to convert the low-speed, high-torque mechanical power to a higher speed, which is required for the electrical generator [58].

Initially, wind power had relatively little impact on the power grid system because the wind turbines used a squirrel cage induction generator (SCIG) directly connected to the network. In SCIG-based systems, all power pulsations captured from the wind were almost directly transferred to the grid, and there was no controllability on the delivered active and reactive power [15]. Increased penetration of wind turbines and their power level capacities dictates the use of power electronics to change the

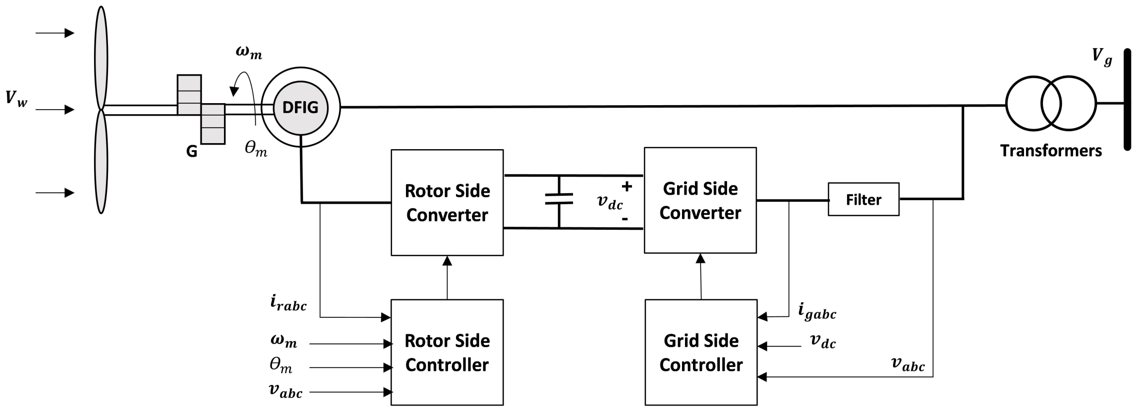

Figure 3.1: DFIG WTG schematics

characteristics of wind turbines from an unregulated energy source to an active power generator. Today, the variable speed Doubly-Fed Induction Generator (DFIG) with a large gearbox and a partial-scale power converter is employed in many wind farms.

Fig. 3.1 depicts a DFIG wind turbine schematics. The stator magnetic field is created by directly supplying the windings of the DFIG by three-phase voltages from the grid at constant amplitude V_s and frequency ω_s. To achieve a satisfactory rotor speed, the rotor windings are connected to the grid by a back-to-back power electronic converter that provides three-phase voltages with different amplitude V_r and frequency ω_r at steady-state. The mechanical speed of the generator is:

$$\omega_m = \omega_s - \omega_r. \tag{3.1}$$

Also, the slip of the generator is:

$$s = \frac{\omega_r}{\omega_s}. \tag{3.2}$$

There are three operating modes for the DFIG based on the rotor speed:

$$\begin{cases} \omega_r > 0 \rightarrow s > 0 \rightarrow & \text{Subsynchronous operation.} \\ \omega_r < 0 \rightarrow s < 0 \rightarrow & \text{Hypersynchronous operation.} \\ \omega_r = 0 \rightarrow s = 0 \rightarrow & \text{Synchronous operation.} \end{cases} \tag{3.3}$$

Therefore, the AC-DC-AC converter and its corresponding controller determine the overall DFIG operating point and power exchange between the rotor and the grid.

Also, the converter/generator of all wind turbines is usually connected to the power grid through a step-up transformer. The volume and losses of the entire system significantly depend on its transformers and filters.

Furthermore, the AC-DC-AC converter system should be cost-effective, easy to maintain, and reliable. It also might need extra components to store active power and boost the voltage from the generator side to the grid side.

3.1.1 Control Variables of AC-DC-AC Converter

To prevent overloading in case of strong winds, it is necessary to waste part of the excess energy of the wind. Therefore, all wind turbines are designed to limit the generated mechanical power by the wind. Three common ways of limiting wind power are stall control, active stall control, and pitch control [59].

In the stall control, the blades are bolted onto the hub at a fixed angle that is designed to adjust the angle at which the wind strikes the blades by rotating around the blade axis. Although the principle is easy to state, it requires a very complex aerodynamic design to avoid stall-induced vibrations. At the active-stall method, the blade angle is adjusted to reduce the rotational speed at low wind speed. When the machine reaches its rated power, the angle at which the wind strikes the blade increases to make the blades go into a deeper stall. This method can be expensive and complex for small wind farms. On a pitch-controlled wind turbine, the output power of the turbine is monitored. When the output power exceeds its limit, the blades slightly pitch out of the wind until the wind drops. To maximize the output power in this method, the blades pitch according to the wind speed to keep the rotor blades at the optimum angle. Among these power limitation methods, pitch control has the best power limitation performance [59].

The rotational speed of the blades is another control variable of DFIG wind turbines. In the SCIG-based WTGs, the rotational speed is fixed during the entire range of wind speeds. The advantages of fixed-speed turbines include their simplicity, robustness, and low-cost electrical components. However, their drawbacks which outweigh their merits, are uncontrollable electrical power, large mechanical stresses during strong gusts, and limited output power quality. Therefore, the rotational speed of the blades is controlled via a rotor side controller in DFIG-based wind turbines. To achieve the maximum power-extracting efficiency in the variable speed wind turbines, the rotational speed of the wind turbine is adapted to the wind speed to keep the tip speed ratio constant. Thus, wind power variations affect the rotor's speed, reducing the wind turbine's mechanical stress and acoustic noise.

Therefore, the rotor current is controlled by Rotor Side Converter (RSC) to regulate the torque of the wind turbine. The RSC will also contribute to adjusting the active power of the system in normal operating conditions and during grid faults. In normal operating conditions, the active power is set to extract the maximum power from the wind turbine, while in grid faults, the generated power is required to reduce quickly. Thus, the RCS should be able to handle the wide range of fundamental frequency and voltage amplitude of the generator output.

The DFIG system should also meet the grid's active and reactive requirements through the Grid Side Converter (GSC). Therefore, the generated power of the system is regulated in the GSC controller by means of controlling the amplitude of the system's output voltage. Stabilizing the DC bus is another objective of the GSC controller.

3.2 Doubly-Fed Induction Generator Wind Turbine Modeling

The DFIG WTG consists of a wind turbine, generator, AC-DC-AC converter, and control system.

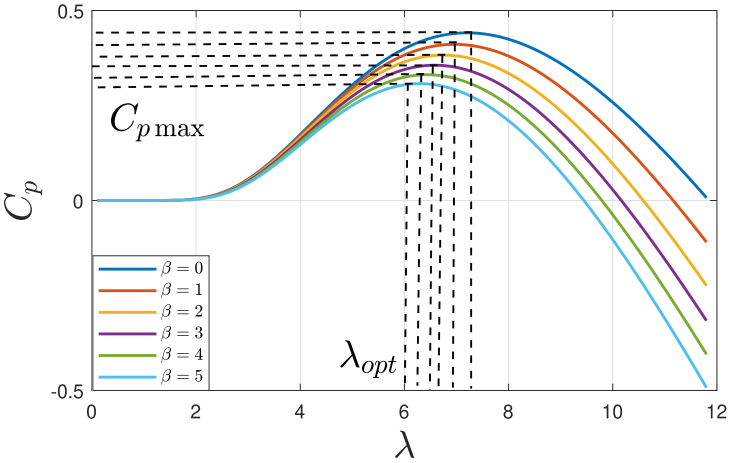

Figure 3.2: C_p Curves for a 250 kW pitch regulated wind turbine in different pitch angles β

3.2.1 Wind Turbine Aerodynamics

The wind power contained in the form of kinetic energy crossing the blades with the surface A is:

$$P_W = \frac{1}{2}\rho A V_W^3, \tag{3.4}$$

where ρ is the air density, and V_W is the wind speed. The wind turbine can only capture a part of wind power P_W:

$$P_m = \frac{1}{2}C_p(\lambda,\beta)\rho\pi R^2 V_W^3, \tag{3.5}$$

where R is the radius of the wind turbine blades, and $C_p(\lambda,\beta)$ is the turbine power coefficient. $C_p(\lambda,\beta)$ determines the effectiveness of the wind turbine in the transformation of the kinetic energy of the wind into mechanical energy, and it depends on the turbine structure. For a given wind turbine, C_p is a function of wind speed V_W, blade rotational speed ω_l, and the pitch angle β:

$$C_p(\lambda,\beta) = \frac{C_{p\,\mathrm{max}}}{\lambda_{opt}^2}\left(2\lambda_{opt} - \lambda\right)\lambda, \tag{3.6}$$

where the turbine Tip Speed Ratio (TSR) is defined as:

$$\lambda = \frac{R\omega_l}{V_W}, \tag{3.7}$$

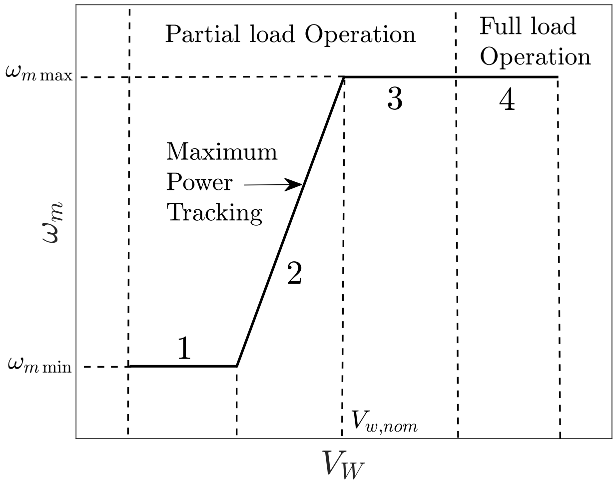

Figure 3.3: Wind turbine speed operating regions

and $C_{p\,\max}$ is the maximum value of C_p, and λ_{opt} is the optimum TSR where $C_p = C_{p\,\max}$. The calculus of C_p curve can be done by experimental measurements. Fig. 3.2 shows an example of $C_p(\lambda, \beta)$ curve for a 250 kW pitch regulated wind turbine.

The mechanical torque can be calculated from the P_m and mechanical speed of the generator ω_m:

$$T_m = \frac{P_m}{\omega_m} = \frac{\rho \pi R^2 V_W^3}{2\omega_m} C_p(\lambda, \beta) = \frac{\rho \pi R^3 V_W^2}{2\lambda} C_p(\lambda, \beta). \tag{3.8}$$

The wind turbine blades are linked to the hub, which is coupled to the slow shaft. The slow shaft is linked to the fast shaft through a gearbox which multiplies the rotational speed by factor G. The fast shaft is then connected to the generator.

Fig. 3.3 depicts the wind turbine mechanical speed ω_m as a function of the wind speed V_W to demonstrate four operating regions of the wind turbine. As a safety precaution, the minimum speed and, consequently, the sliding of the electrical machine is limited, so the turbine cannot rotate at speeds matching the resonant frequency of the tower. Also, the maximum speed limit is set to avoid damage to the blades and shaft during strong winds.

Therefore, the DFIG starts operating at the cut-in rotating speed $\omega_{m\,\min}$ in zone 1. When the wind speed exceeds the limit that provides the $\omega_{m\,\min}$, turbine blades rotate at their maximum aerodynamic capability to provide the maximum extracting power in Zone 2. As the wind speed increases in this zone, the mechanical rotation speed increases until it reaches the maximum rotation speed $\omega_{m\max}$. When wind speed reaches its nominal value, the blades rotate with $\omega_{m\max}$ in zone 3. In this zone, the DFIG operates at its rated mechanical power, and the energy captured from stronger winds should be kept at its nominal value. In zone 4, DFIG operates in full load; where the mechanical power should be limited by pitch or torque control in a way that torque is maintained at its nominal value and the pitch angle is adjusted to keep the mechanical speed at $\omega_{m\max}$.

The main objective of operation in zones 1 and 3 are maintaining the mechanical speed at predefined constant values. In other words, the DFIG operates with constant speed, which is $\omega_{m\min}$ for zone 1 and $\omega_{m\max}$ for zone 3. In zone 2, the speed of the turbine should be adjusted with regard to the wind speed to maintain a specific TSR λ_{opt} corresponding to the maximum power coefficient $C_{p\max}$. The Indirect Speed Controller (ISC) is used for zone 2 to extract the maximum power from the wind turbine [60]. In ISC, the electromagnetic torque reference T_e^* correlated to the maximum power curve is calculated considering $V_W = \frac{R\omega_l}{\lambda_{opt}}$:

$$T_e^* = \frac{1}{2}\rho\pi R^3 \frac{R^2\omega_l^2}{\lambda_{opt}^2}\frac{C_{p\max}}{\lambda_{opt}} = \frac{K_{opt}\omega_m^2}{G^3}, \tag{3.9}$$

where K_{opt} is:

$$K_{opt} = \frac{1}{2\lambda_{opt}^3}\rho\pi R^5 C_{p\max}. \tag{3.10}$$

3.2.2 Doubly-Fed Induction Machine (DFIM)

Fig. 3.4 shows the steady-state circuit of the DFIG. Assuming a symmetrical machine, only one phase of the stator and rotor is demonstrated while the other two phases are essentially equal. In this figure, R_s, R_r', $L_{\sigma s}$, $L_{\sigma r}'$, and L_m are stator resistance, rotor resistance, stator leakage inductance, rotor leakage inductance, and mutual inductance, respectively. Also, $\underline{I}_s$, $\underline{I}'_r$, $\underline{E}_s$, and $\underline{E}'_{rs}$ are stator current, rotor current,

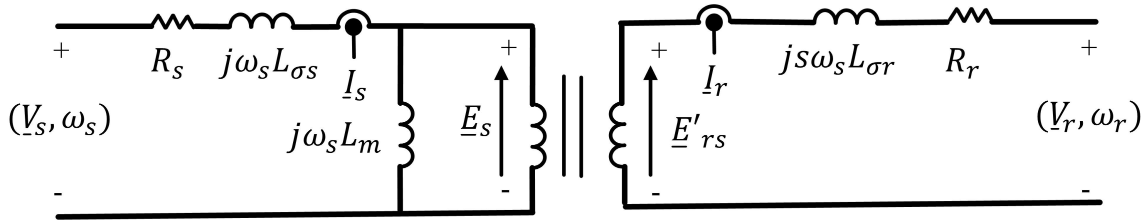

Figure 3.4: One-phase steady-state circuit of a DFIG

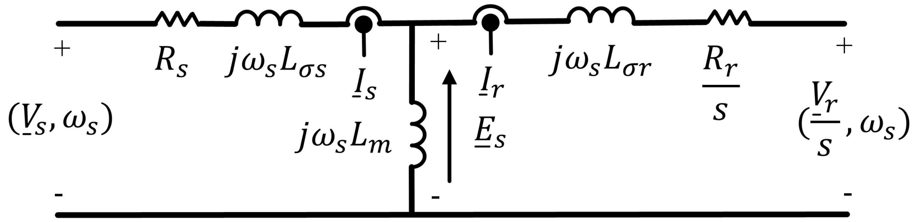

Figure 3.5: One-phase steady-state circuit of a DFIG referred to the stator

induced emf in the stator, and induced emf in the rotor, respectively. Because stator windings see the rotor field at its own synchronous frequency ω_s, it is favourable to represent the circuit referred to stator as shown in Fig. 3.5. Therefore, $\underline{V}_s$, $\underline{V}_r$, can be written as:

$$\underline{V}_s = R_s\underline{I}_s + j\omega_s L_{\sigma s}\underline{I}_s + j\omega_s L_m(\underline{I}_s + \underline{I}_r), \tag{3.11}$$

$$\frac{\underline{V}_r}{s} = \frac{R_r}{s}\underline{I}_r + j\omega_s L_{\sigma r}\underline{I}_r + j\omega_s L_m(\underline{I}_s + \underline{I}_r). \tag{3.12}$$

Also, the stator flux $\underline{\psi}_s$ and rotor flux $\underline{\psi}_r$ are:

$$\underline{\psi}_s = L_m(\underline{I}_s + \underline{I}_r) + L_{\sigma s}\underline{I}_s = L_s\underline{I}_s + L_m\underline{I}_r, \tag{3.13}$$

$$\underline{\psi}_r = L_m(\underline{I}_s + \underline{I}_r) + L_{\sigma r}\underline{I}_r = L_r\underline{I}_r + L_m\underline{I}_s, \tag{3.14}$$

where the stator inductance is $L_s = L_m + L_{\sigma s}$ and rotor inductance is $L_r = L_m + L_{\sigma r}$. The space vector theory is then applied to the machine's basic electric equations to find the system's representation in different rotating reference frames instead of the classic three-phase representation.

Space vector representation

The space vector theory is a common tool that can be applied to the AC machine's flux, voltage and current. For example, rotor current can be written as:

$$I_r = I_{ra}e^{j0} + I_{rb}e^{j\frac{2\pi}{3}} + I_{rc}e^{j\frac{4\pi}{3}}, \tag{3.15}$$

where I_{ra}, I_{rb}, and I_{rc} are the rotor current magnitude in phases a, b and c, respectively. Therefore, the I_r representation in the stationary reference frame is:

$$\frac{3}{2}[I_{r\alpha} + jI_{r\beta}] = (I_{ra} + I_{rb}\cos\frac{2\pi}{3} + I_{rc}\cos\frac{4\pi}{3}) + j(I_{rb}\sin\frac{2\pi}{3} + I_{rc}\sin\frac{4\pi}{3}). \tag{3.16}$$

The constant 3/2 is chosen to scale the $\alpha - \beta$ representation according to the peak amplitude of the abc magnitudes. Thus, the matrix representation of the I_r in a real-imaginary complex plane is:

$$\begin{bmatrix} I_{r\alpha} \\ I_{r\beta} \end{bmatrix} = \frac{2}{3}\begin{bmatrix} 1 & -\frac{1}{2} & -\frac{1}{2} \\ 0 & \frac{\sqrt{3}}{2} & -\frac{\sqrt{3}}{2} \end{bmatrix}\begin{bmatrix} I_{ra} \\ I_{rb} \\ I_{rc} \end{bmatrix}. \tag{3.17}$$

Similar equations can be written to find the stationary $\alpha - \beta$ frame representation of the other three-phase voltages, currents and fluxes. It is worth mentioning that $I_{r\alpha}$ and $I_{r\beta}$ have sinusoidal time-varying magnitudes at stator frequency. Hence, it is useful to find the representation of the I_r in the rotating reference frame $\mathrm{d} - \mathrm{q}$ which rotates at speed ω_s and its components are constant. The $\mathrm{d} - \mathrm{q}$ representation of the I_r is:

$$I_{r_{dq}} = I_{r_{\alpha\beta}}e^{-j\omega_s} = (I_{r\alpha} + jI_{r\beta})(\cos\omega_s + j\sin\omega_s). \tag{3.18}$$

The matrix representation of the I_r in qd frame is:

$$\begin{bmatrix} I_{rd} \\ I_{rq} \end{bmatrix} = \begin{bmatrix} \cos\omega_s & \sin\omega_s \\ -\sin\omega_s & \cos\omega_s \end{bmatrix}\begin{bmatrix} I_{r\alpha} \\ I_{r\beta} \end{bmatrix}. \tag{3.19}$$

Figure 3.6 shows the space vector representation of the I_r in abc, $\alpha - \beta$, and $\mathrm{d} - \mathrm{q}$ reference frames.

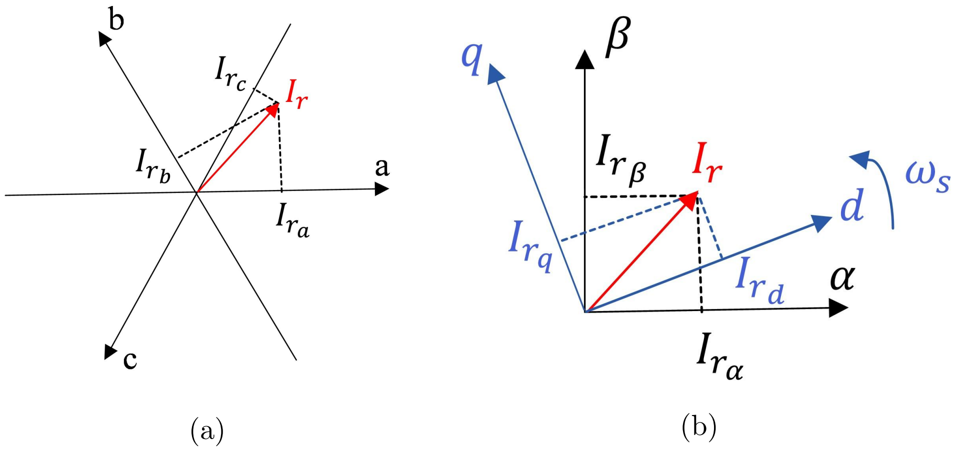

(a) (b)

Figure 3.6: Space vector representation of (a) abc (b) $\alpha - \beta$ and d − q frame

DFIG dynamic modeling

The d − q representation of $\overrightarrow{v_s}$ and $\overrightarrow{v_r}$ can be calculated by multiplying their $\alpha - \beta$ representation by $e^{-j\theta_s}$ and $e^{-j\theta_r}$ respectively:

$$\overrightarrow{v}_s^{dq} = R_s \overrightarrow{i_s}^{dq} + \frac{d\psi_s^{dq}}{dt} + j\omega_s \psi_s^{dq} \rightarrow \begin{cases} v_{ds} = R_s i_{ds} + \frac{d\psi_{ds}}{dt} - \omega_s \psi_{qs}, \\ v_{qs} = R_s i_{qs} + \frac{d\psi_{qs}}{dt} + \omega_s \psi_{ds}, \end{cases} \tag{3.20}$$

$$\overrightarrow{v}_r^{dq} = R_r \overrightarrow{i_r}^{dq} + \frac{d\psi_r^{dq}}{dt} + j\omega_r \psi_r^{dq} \rightarrow \begin{cases} v_{dr} = R_r i_{dr} + \frac{d\psi_{dr}}{dt} - \omega_r \psi_{qr}, \\ v_{qr} = R_r i_{qr} + \frac{d\psi_{qr}}{dt} + \omega_r \psi_{dr}. \end{cases} \tag{3.21}$$

The stator and rotor fluxes can also be calculated in d − q frame as:

$$\overrightarrow{\psi}_s^{dq} = L_s \overrightarrow{i_s}^{dq} + L_m \overrightarrow{i_r}^{dq} \rightarrow \begin{cases} \psi_{ds} = L_s i_{ds} + L_m i_{dr}, \\ \psi_{qs} = L_s i_{qs} + L_m i_{qr}, \end{cases} \tag{3.22}$$

$$\overrightarrow{\psi}_r^{dq} = L_r \overrightarrow{i_r}^{dq} + L_m \overrightarrow{i_s}^{dq} \rightarrow \begin{cases} \psi_{dr} = L_r i_{dr} + L_m i_{ds}, \\ \psi_{qr} = L_r i_{qr} + L_m i_{qs}. \end{cases} \tag{3.23}$$

The mechanical torque can be written as:

$$T_m = \frac{3}{2} p \frac{L_m}{L_s} (\psi_{qs} i_{dr} - \psi_{ds} i_{qr}), \tag{3.24}$$

where p is the number of machine poles. The electric circuit of the DFIG in d − q frame is presented in Fig. 3.7.

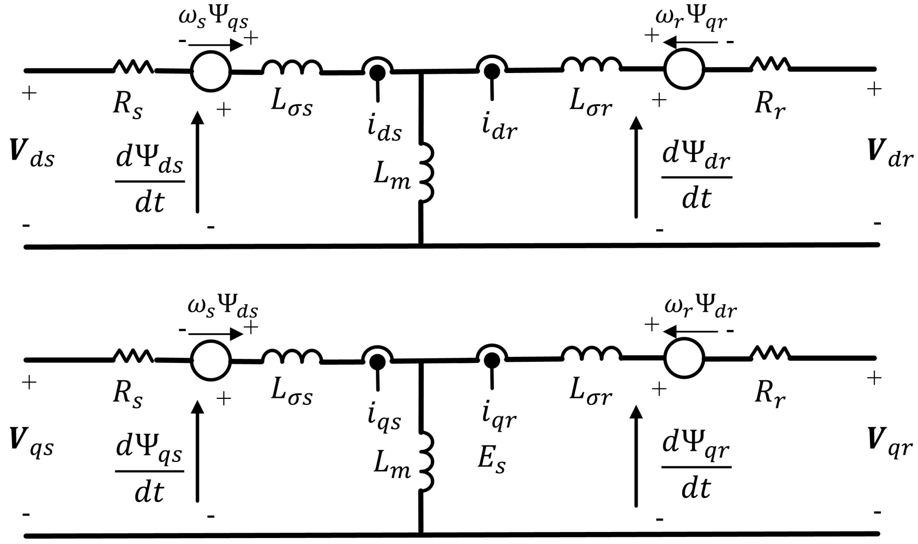

Figure 3.7: DFIG model in $\mathrm{d}-\mathrm{q}$ frame

3.2.3 AC-DC-AC converter and its Control System

The AC-DC-AC converter consists of an AC-DC Rotor Side Converter (RSC), a DC bus with a voltage v_{dc}, and a DC-AC Grid Side Converter (GSC).

Rotor Side Controller

As mentioned in section 3.1.1, the control system of a variable speed wind turbine determines the reference torque and pitch angle to keep the system in the safe operating mode, extract the maximum energy from the wind, and minimize the mechanical loads on the shaft. Therefore, the RSC controller is responsible for generating a three-phase voltage with adjustable amplitude and frequency to control the generated torque. Fig. 3.8 shows the vector control approach of the RSC controller presented in [61].

As shown in Fig. 3.8, the rotor voltage is regulated by means of controlling the rotor current in a synchronously rotating $\mathrm{d}-\mathrm{q}$ frame. In this frame, the d-axis is aligned with the stator flux [60]; therefore, the $\psi_{ds} = |\overrightarrow{\psi_s}|$ and $\psi_{qs} = 0$. By substituting (3.22)

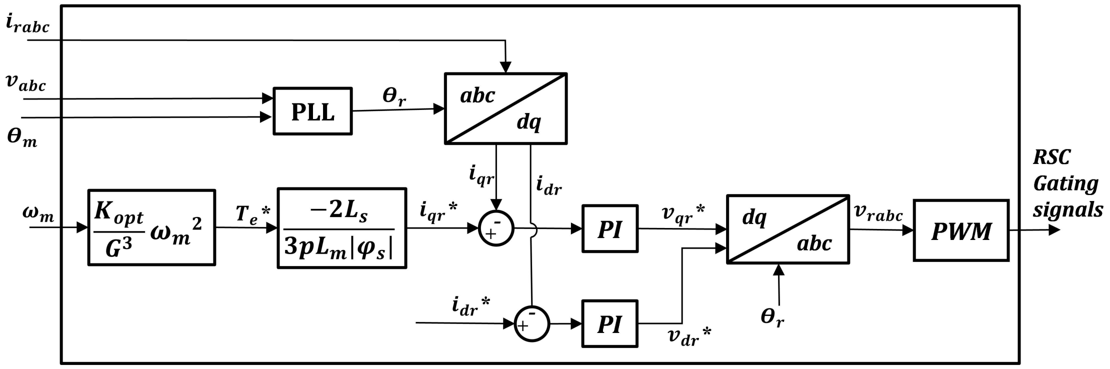

Figure 3.8: RSC controller

and (3.23) in (3.21) the rotor voltage can be rewritten as:

$$\begin{aligned} v_{dr} &= R_r i_{dr} + \sigma L_r \frac{di_{dr}}{dt} - \omega_r \sigma L_r i_{qr} + \frac{L_m}{L_s}\frac{d}{dt}|\psi_s|, \\ v_{qr} &= R_r i_{qr} + \sigma L_r \frac{di_{qr}}{dt} + \omega_r \sigma L_r i_{dr} + \omega_r \frac{L_m}{L_s}|\psi_s|, \end{aligned} \tag{3.25}$$

where $\sigma = 1 - {L_m}^2/(L_s L_r)$. Assuming a small voltage drop in stator resistance, it can be concluded that the term $\frac{d}{dt}|\psi_s| = 0$, because the stator flux is constant. Thus, the d − q representation of the rotor voltage can be regulated by using a PI controller for i_{dr} and i_{qr} as shown in Fig. 3.8.

To find the d − q representation of the i_{rabc}, the rotating speed θ_r should be calculated. As mentioned in (3.1), the θ_r can be obtained based on the θ_s and θ_m. Based on the (3.11) and (3.13), the θ_s can be obtained by subtracting 90° from the angle of the stator voltage . Therefore, a Phase-Lock Loop (PLL) technique is used for grid synchronization, increasing robustness, and rejecting small disturbances or harmonics [62].

To find the i_{qr}^*, (3.24) can be rewritten as:

$$T_m^* = -\frac{3}{2}p\frac{L_m}{L_s}|\psi_s| i_{qr}^*, \tag{3.26}$$

where T_m^* can be calculated by (3.9). Thus, the i_{qr} is proportional to the torque; consequently, its quadrature value is proportional to the speed of the machine.

As mentioned earlier, the stator flux is constant $|\overrightarrow{\psi_s}| \cong \sqrt{\frac{2}{3}\frac{\mathbf{V}_s}{\omega_s}}$ because the stator of the machine is connected directly to the grid. $\mathbf{V}_s$ is the rated rms value of stator

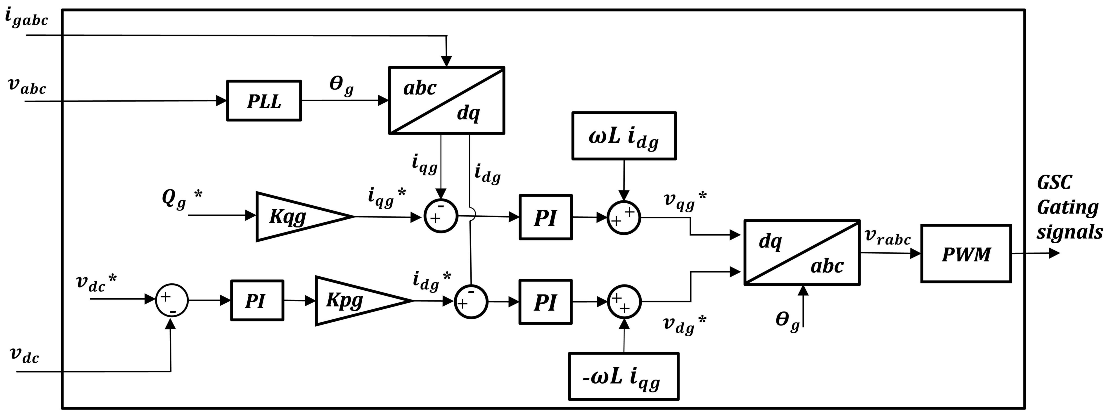

Figure 3.9: GSC controller

line-to-line voltage. The d − q representation of the $\overrightarrow{\psi_s}$ can be written as:

$$\begin{aligned} \psi_{ds} &= |\overrightarrow{\psi_s}| = L_s i_{ds} + L_m i_{dr}, \\ \psi_{qs} &= 0 = L_s i_{qs} + L_m i_{qr}. \end{aligned} \tag{3.27}$$

Hence, the stator flux level can be determined by distributing the required amount of current between the stator i_{ds} and rotor i_{dr}. It is typical to set the rotor current $i^*_{dr} = 0$ to use all of the RSC capacity for active power delivery from the rotor windings as the required reactive power for the induction machine is provided by the GSC. This decision results in increasing the dimension of the stator windings. It is worth mentioning that the generality of the proposed method is not limited by the i^*_{dr} set value.

Grid Side Controller

The AC-DC-AC converter must conform to the grid requirements regardless of the wind speed. Therefore, the GSC should be able to control the active and reactive power delivered to the grid and provide grid support. Furthermore, the GSC controller maintains a fixed fundamental frequency and voltage amplitude on the grid side and restrains the current's Total Harmonic Distortion (THD) at a low level [63, 64]. The reactive power is regulated to generate the expected predefined Q^*_g, while the active power is indirectly controlled by regulating the DC bus and reactive power.

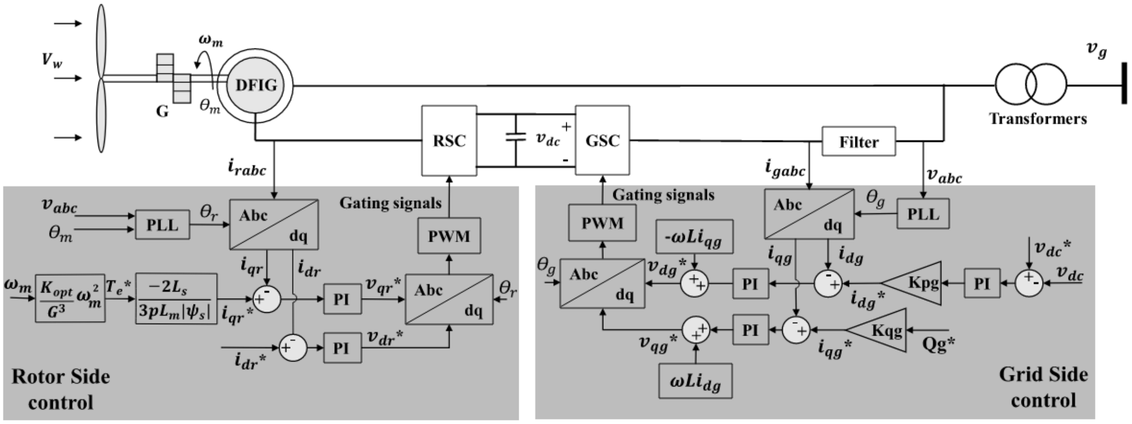

Figure 3.10: DFIG WTG complete schematic

Fig. 3.9 shows the vector control approach of the GSC controller. To ensure the DC link voltage stability, the GSC controller regulates the DC bus voltage v_{dc}. The d-axis grid reference current i^*_{dg} is generated by using the PI compensator on the DC voltage error where K_{pg} and K_{qg} are:

$$K_{pg} = \frac{2}{3\mathbf{V}_s\sqrt{\frac{2}{3}}}, \qquad K_{qg} = -\frac{2}{3\mathbf{V}_s\sqrt{\frac{2}{3}}}. \tag{3.28}$$

The q-axis grid current reference i^*_{qg} is generated by multiplying K_{qg} in the reactive power reference Q^*_g. Because the dominant reactive power consumed by an induction machine is determined by its magnetizing inductance, the $Q^*_q \cong v_s^2/X_m$, where v_s is the measured stator rms line-to-line voltage and X_m is the machine magnetizing reactance. The $\mathrm{d}-\mathrm{q}$ representation of the grid current is calculated by obtaining the rotating speed θ_g, where θ_g is the angle of the grid voltage. As shown in Fig. 3.9, the reference grid voltage in $\mathrm{d}-\mathrm{q}$ frame v^*_{dg} and v^*_{qg} are then determined by an inner current control loop on i^*_{dg} and i^*_{qg}, respectively.

The DFIG WTG complete schematic is depicted in Fig. 3.10.

3.2.4 Steady-State Derivation

A small-signal model of a WTG is required to find the dynamic model of a DFIG-based wind farm. To find the small-signal model of a WTG, the steady-state magnitudes of the system should be calculated for a given operating point. The steady-state electro-mechanical relationship between the mechanical side and electrical side of a WTG is:

$$T_m + T_e = D\omega_m, \tag{3.29}$$

where T_e is the electrical torque, and D is the mechanical damping of the induction machine. Thus, assuming that the T_m and $I_{dr} = 0$ are given for a specific operating point, the other variable magnitudes of the system at steady-state can be calculated.

By assuming that the control system is stable, it can be concluded that $T_e^* = T_e$. Therefore, the steady-state speed, ω_{m_0}, is obtained by substituting (3.8) and (3.9) into (3.29). Thus, all other DFIG steady-state parameters can be expressed as follows [61]:

$$\begin{gathered}
T_{e_0} = K_{opt}\omega_{m_0}^2, \quad I_{qr} = -\frac{T_{m_0}}{\frac{3}{2}p\frac{L_m}{L_s}|\psi_s|}, \quad I_{dr} = 0, \\
T_{m_0} = T_{e_0} + D\omega_{m_0}, \quad I_{qs} = -\frac{L_m}{L_s}I_{qr}, \quad I_{ds} = \frac{|\psi_s|}{L_s}, \\
V_{ds} = R_s I_{ds}, \quad V_{qs} = R_s I_{qs} + \omega_s|\psi_s|, \quad s = \frac{\omega_r}{\omega_s},
\end{gathered} \tag{3.30}$$

where $|\psi_s| = |\psi_s| = \sqrt{\frac{-B\pm\sqrt{B^2-4AC}}{2A}}$ with:

$$A = \frac{R_s^2}{L_s^2} + \omega_s^2, \quad B = \frac{4R_sT_{m_0}\omega_s}{3p} - |V_s|^2, \quad C = (\frac{2R_sT_{m_0}}{3pL_m})^2. \tag{3.31}$$

3.3 Proposed Weighted Dynamic Aggregation Model of DFIG Based Wind Farm

The equivalent WD Agg model of a DFIG-based wind farm is proposed in two sections: equivalent DFIM and corresponding control system (electrical side) and equivalent wind turbine (mechanical part). This section calculates the wind farm equivalent electrical side (generator and control system) and mechanical part (the equivalent turbine) separately:

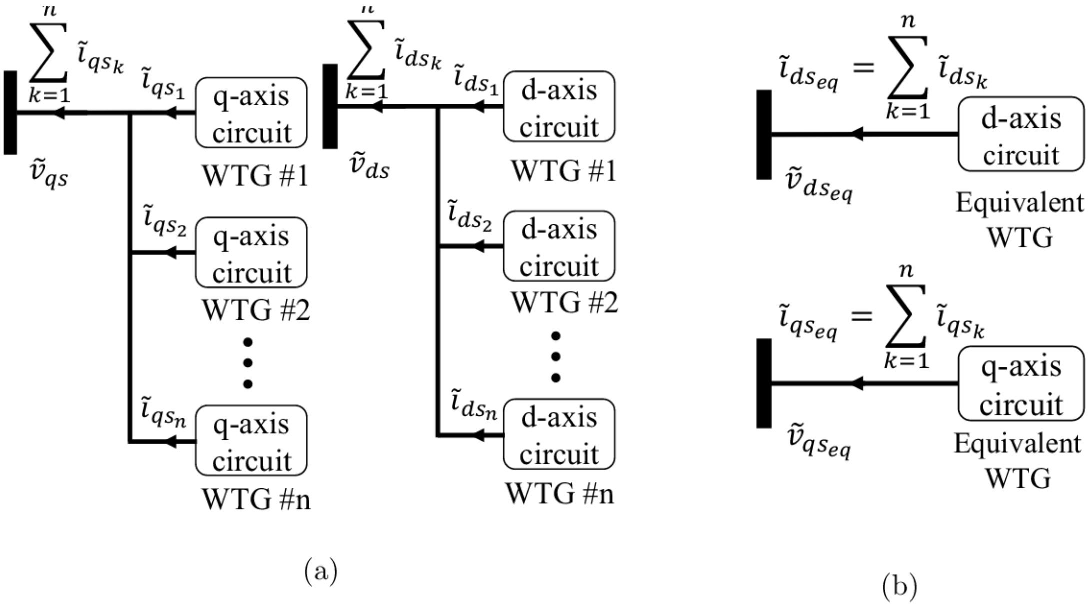

Figure 3.11: (a) Wind farm d − q axis circuits. (b) Equivalent model d − q axis circuits

3.3.1 Equivalent DFIM and Control System

WTGs are connected to the grid in parallel; therefore, the small-signal d − q representation of a wind farm circuit is depicted in Fig. 3.11a. The objective is to find an equivalent DFIM whose dynamic behavior is similar to the overall wind farm from the grid point of view. Thus, the equivalent DFIM should have a similar small-signal d − q equations to the wind farm as shown in Fig. 3.11b:

$$\begin{gathered} \tilde{v}_{ds_{eq}} = \tilde{v}_{ds}, \quad \tilde{v}_{qs_{eq}} = \tilde{v}_{qs}, \\ \tilde{i}_{ds_{eq}} = \sum_{k=1}^{n} \tilde{i}_{ds_k}, \quad \tilde{i}_{qs_{eq}} = \sum_{k=1}^{n} \tilde{i}_{qs_k}. \end{gathered} \tag{3.32}$$

The differential equation relating $\tilde{i}_{dqs}$ and $\tilde{v}_{dqs}$ is derived to find the interaction of the wind farm with the grid. The proposed equivalent DFIM should also have similar interaction with the grid; therefore, the equivalent parameters of the WD Agg model can be calculated based on the corresponding wind farm parameters. Then, the equivalent WTG parameters can be determined by the weighted average of WTGs parameters, where the weight of each WTG is determined by the contribution of that WTG injected current to the grid.

Because P_m is constant, (3.8) can be linearized as:

$$\tilde{P}_m = \tilde{T}_m \omega_{m_0} + T_{m0}\tilde{\omega}_m = \tilde{C}_p(\lambda, \beta) P_W, \tag{3.33}$$

where P_W is defined in (3.4). Because β is constant $\tilde{C}_p(\lambda, \beta)$ is:

$$\tilde{C}_p(\lambda, \beta) = \left.\frac{\partial C_p}{\partial \lambda}\right|_{\lambda=\lambda_0} \tilde{\lambda} = \left.\frac{\partial C_p}{\partial \lambda}\right|_{\lambda=\lambda_0} \frac{r\tilde{\omega}_m}{GV_W}. \tag{3.34}$$

By substituting (3.34) in (3.33), $\tilde{T}_m$ can be obtained as:

$$\tilde{T}_m = e_m \tilde{\omega}_m, \tag{3.35}$$

where e_m is:

$$e_m = \left(\left.\frac{\partial C_p}{\partial \lambda}\right|_{\lambda=\lambda_0} \frac{rP_W}{GV_W} - T_{m0} \right) / \omega_{m_0} \tag{3.36}$$

The mechanical linearized equation of the induction machine is calculated in [65], where $\tilde{T}_m$ is:

$$\tilde{T}_m = X_m I_{dr} \tilde{i}_{qs} - X_m I_{qr} \tilde{i}_{ds} - X_m I_{ds} \tilde{i}_{qr} + X_m I_{qs} \tilde{i}_{dr} - 2H \frac{d}{dt} \tilde{\omega}_m, \tag{3.37}$$

where H is the turbine inertia constant. Therefore, $\tilde{\omega}_m$ can be determined in terms of $\tilde{i}_{dqs}$ and $\tilde{i}_{dqr}$ by substituting (3.35) into (3.37). Let's assume than the controller is fast; therefore, $T_e^* = T_e$ and $i_{dqr}^* = i_{dqr}$. Thus, $\tilde{i}_{qr}$ can be calculated by substituting (3.35) into the linearized controller equation(3.26):

$$\tilde{i}_{qr} = \frac{e_m}{\frac{3}{2} p \frac{L_m}{L_s} \left|\psi_s\right|} \tilde{\omega}_m. \tag{3.38}$$

Hence, $\tilde{i}_{qr}$ can be written as a function of $\tilde{i}_{dqs}$ because $\tilde{\omega}_m$ is a function of $\tilde{i}_{dqs}$ and $\tilde{i}_{dqr}$, and $\tilde{i}_{dr} = i_{dr}^* = 0$.

The linearized stator equations can be determined as:

$$\begin{aligned} \tilde{v}_{ds} &= (R_s + L_s \frac{d}{dt}) \tilde{i}_{ds} - \omega_s L_s \tilde{i}_{qs} + L_m \frac{d}{dt} \tilde{i}_{dr} - \omega_s L_m \tilde{i}_{qr} = \alpha_{dd} \tilde{i}_{ds} + \alpha_{dq} \tilde{i}_{qs}, \\ \tilde{v}_{qs} &= \omega_s L_s \tilde{i}_{ds} + (R_s + L_s \frac{d}{dt}) \tilde{i}_{qs} + \omega_s L_m \tilde{i}_{dr} + L_m \frac{d}{dt} \tilde{i}_{qr} = \alpha_{qd} \tilde{i}_{ds} + \alpha_{qq} \tilde{i}_{qs}, \end{aligned} \tag{3.39}$$

where $\alpha_{dd}, \alpha_{dq}, \alpha_{qd}$ and α_{qq} are a function of both WTG and calculated steady-state parameters. The frequency response of $\alpha_{dd}, \alpha_{dq}, \alpha_{qd}$ and α_{qq} for an arbitrary ω can be determined by replacing $\frac{d}{dt}$ with $j\omega$. Because the dc components of these variables are required to find the desired $\tilde{v}_{dqs}, \tilde{i}_{dqs}$, the corresponding equations for $\alpha_{dd}, \alpha_{dq}, \alpha_{qd}$ and α_{qq} can be derived for $\omega = 0$. Now, $\tilde{i}_{dqs}$ can be determined by rewriting (3.39) as:

$$\begin{aligned} \tilde{i}_{ds} &= y_{dd}\tilde{v}_{ds} + y_{dq}\tilde{v}_{qs}, \\ \tilde{i}_{qs} &= y_{qd}\tilde{v}_{ds} + y_{qq}\tilde{v}_{qs}, \end{aligned} \tag{3.40}$$

where y_{dd}, y_{dq}, y_{qd}, and y_{qq} are:

$$\begin{aligned} y_{dd} &= \alpha_{qq}/\Delta_y, \quad y_{dq} = -\alpha_{dq}/\Delta_y, \\ y_{qd} &= -\alpha_{qd}/\Delta_y, \quad y_{qq} = \alpha_{dd}/\Delta_y, \end{aligned} \tag{3.41}$$

where:

$$\Delta_y = \alpha_{dd}\alpha_{qq} - \alpha_{dq}\alpha_{qd}. \tag{3.42}$$

Therefore, the contribution of each WTG in the injected current of the wind farm to the grid can be determined by calculating (3.40) for each WTG. Thus, the weight of each WTG is obtained.

As shown in Fig. 3.11, the currents of each WTG and overall wind farm can be projected to d and q axis circuits. To make the derivations more straightforward, the $\mathrm{d} - \mathrm{q}$ axis is rotated to $\mathrm{d}' - \mathrm{q}'$ so that the overall current injected to the grid does not have any q-component as shown in Fig. 3.12. Rewriting (3.40) in the new $\mathrm{d}' - \mathrm{q}'$ frame where $\sum_{k=1}^{n} \tilde{i}'_{qs_k} = 0$, $\tilde{v}'_{ds} = |\Delta V_s|$ and $\tilde{v}'_{qs} = 0$:

$$\begin{aligned} \tilde{i}'_{ds} &= (y_{dd}\cos^2\delta_0 + y_{qq}\sin^2\delta_0 - (y_{dq} + y_{qd})\sin\delta_0\cos\delta_0)\tilde{v}'_{ds}, \\ \tilde{i}'_{qs} &= (y_{qd}\cos^2\delta_0 - y_{dq}\sin^2\delta_0 + (y_{dd} - y_{qq})\sin\delta_0\cos\delta_0)\tilde{v}'_{ds}, \end{aligned} \tag{3.43}$$

where δ_0 is the difference between the two $\mathrm{d} - \mathrm{q}$ phase reference frames as depicted in Fig. 3.12. Therefore, the weight of jth WTG can be defined as:

$$\mu_j = \frac{\tilde{i}'_{ds_j}}{\sum_{k=1}^{n} \tilde{i}'_{ds_k}}. \tag{3.44}$$

Now, the equivalent DFIM and control parameters can be calculated by weighted averaging the wind farm corresponding parameters in per unit. It is noteworthy that the apparent power of the equivalent WTG is the summation of the apparent powers

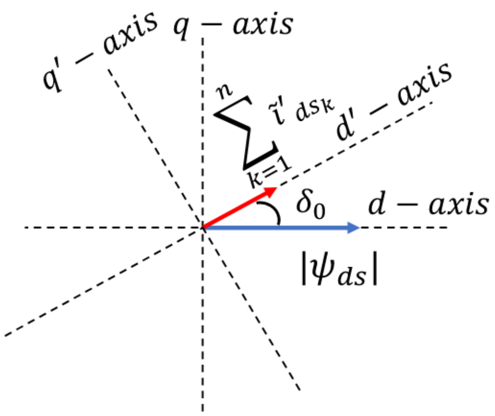

Figure 3.12: Rotating the d − q frame by δ_0

of all the WTGs in the wind farm $S_{eq} = \sum_{k=1}^{n} S_k$. For instance, the equivalent $R_{s_{eq}}$ can be obtained as:

$$R_{s_{eq}}^{pu} = \sum_{k=1}^{n} \mu_k R_{s_k}^{pu}. \tag{3.45}$$

The control parameters can also be normalized using their unit. For instance, K_p unit is $[V/A]$ which similar to an impedance; therefore, $K_{p_{eq}}$ can be calculated like (3.45) as:

$$K_{p_{eq}}^{pu} = \sum_{k=1}^{n} \mu_k K_{p_k}^{pu}. \tag{3.46}$$

Therefore, the equivalent WTG parameters are obtained through one-time calculations of the weighted dynamic model of a reduced-order system:

$$\dot{X}_{eq} = [A_{eq}]\, X_{eq}, \tag{3.47}$$

where X_{eq} is the states of the reduced-order equivalent WTG model, and A_{eq} is in terms of system parameters and equilibrium points. (3.47) is derived from the full-order model of the detailed wind farm:

$$\dot{X} = [A_W]\, X, \tag{3.48}$$

where X is the full-order system state, and A_W is the detailed system matrix. These derivatives can also be used in large-signal events by dividing the large-signal variations into small-signal steps and updating the equilibrium points in A_{eq}.

3.3.2 Equivalent Wind Turbine

In this section, an equivalent turbine and wind speed of the wind farm are obtained for the equivalent WD Agg model. It is worth mentioning that the area which is covered by the equivalent turbine should be equal to the summation of the area that all the WTGs cover in the wind farm combined:

$$A_{eq} = \sum_{k=1}^{n} A_k. \tag{3.49}$$

Also, the amount of wind power in the area is independent of the wind farm structure; thus, $V_{W_{eq}}$ can be obtained as:

$$P_{W_{eq}} = \sum_{k=1}^{n} P_{W_k} \quad \rightarrow \quad V_{W_{eq}} = \sqrt[3]{\frac{\sum_{k=1}^{n} A_k V_{W_k}^3}{A_{eq}}}. \tag{3.50}$$

Moreover, the equivalent mechanical power P_m generated by the equivalent turbine should be equal to the summation of wind farm's generated mechanical power:

$$P_{m_{eq}} = \sum_{k=1}^{n} P_{m_k}. \tag{3.51}$$

Let's assume $T_{e_{eq}} = \sum_{k=1}^{n} T_{e_k}$ in steady-state to get a more realistic results. Therefore, G_{eq} can be obtained as:

$$G_{eq} = \sqrt[3]{\frac{\omega_{m0_{eq}}^2 K_{opt_{eq}}}{\sum_{k=1}^{n} \omega_{m0_k}^2 \frac{K_{opt_k}}{G_k^3}}}, \tag{3.52}$$

where $K_{opt_{eq}} = \sum_{k=1}^{n} \mu_k K_{opt_k}^{pu}$. $\omega_{m0_{eq}}$, can be calculated similar to the section 3.2.4 calculations by considering:

$$\begin{gathered} I_{qs_{eq}} = \sum_{k=1}^{n} I_{qs_k}, \quad I_{qr_{eq}} = -\frac{L_{s_{eq}}}{L_{m_{eq}}} I_{qs_{eq}}, \\ T_{e0_{eq}} = -\frac{3}{2} p_{eq} \frac{L_{m_{eq}}}{L_{s_{eq}}} \left|\psi_{s_{eq}}\right| I_{qr_{eq}}, \quad T_{m0_{eq}} = \frac{P_{m0_{eq}}}{\omega_{m0_{eq}}}. \end{gathered} \tag{3.53}$$

Furthermore, the equivalent turbine curve $C_{p\max_{eq}}$ and $\lambda_{opt_{eq}}$ can be determined by considering $P_{m_{eq}} = \sum_{k=1}^{n} P_{m_k}$:

$$C_{p_{eq}} P_{W_{eq}} = \sum_{k=1}^{n} C_{p_k} P_{W_k}, \quad K_{opt_{eq}}^{pu} = \sum_{k=1}^{n} \mu_k K_{opt_k}^{pu}, \tag{3.54}$$

Table 3.1: Scenarios 1 and 2 specifications: a 4-WTGs DFIG wind farm with equal WTG parameters and various wind speeds

Parameter	WTG1	WTG2	WTG3	WTG4	Unit
V_W(Sc.1, 2)	$9.5, 11.5$	$9.5, 11.5$	$9.5, 6.5$	$9.5, 6.5$	[m/s]
S	2	2	2	2	[MVA]
J	127	127	127	127	[kgm^2]
τ_n	100	100	100	100	[ms]
r	48	48	48	48	[m]
λ_{opt}	7.9168	7.9168	7.9168	7.9168	[−]

Table 3.2: Scenarios 3, 4, and 5 specifications: a 4-WTGs DFIG wind farm with unequal WTG parameters and various wind speeds

Parameter	WTG1	WTG2	WTG3	WTG4	Unit
V_W(Sc.3)	9.5	9.5	9.5	9.5	[m/s]
V_W(Sc.4)	11.5	11.5	6.5	6.5	[m/s]
V_W(Sc.5)	6.5	6.5	11.5	11.5	[m/s]
S	2	2	0.5	0.5	[MVA]
J	127	127	31.75	31.75	[kgmm^2]
τ_n	100	100	25	25	[ms]
r	48	48	24	24	[m]
λ_{ept}	7.91681	7.91681	3.9584	3.9584	[−]

where $K_{opt_{eq}}$ is:

$$K_{opt_{eq}} = \frac{1}{2}\rho\pi R_{eq}^5 C_{p\max_{eq}} / \lambda_{opt_{eq}}^3 \tag{3.55}$$

There are three possibilities to model the equivalent inertia J_{eq}:

1) By the summation of all turbines inertia similar to the existing Full and Zone Agg methods $J_{eq} = \sum_{k=1}^{n} J_k$,

2) Based on the total angular momentum of all WTGs $J_{eq}\omega_{m_{eq}} = \sum_{k=1}^{n} J_k\omega_{m_k}$,

3) Based on the total rotational energy of all WTGs $\frac{1}{2}J_{eq}\omega_{m_{eq}}^2 = \frac{1}{2}\sum_{k=1}^{n} J_k\omega_{m_k}^2$.

To compare these approaches, a 4-WTG DFIG wind farm is simulated in five different case scenarios of equal and unequal rated power, inertia, and operating points. Scenario 1 to 5 specifications can be found in Tables 3.1 and 3.2, where scenarios 2, 4 and 5 are extreme conditions that two groups of WTGs operating speeds are different by 0.5pu. Also, a 0.2pu voltage drop is applied at $t = 4s$ and cleared

Table 3.3: Aggregated J_{eq} modeled by summation, total angular momentum, and total rotational energy approaches in scenarios 1 to 5

Approach	Sc. 1	Sc. 2	Sc. 3	Sc. 4	Sc. 5
Summation	508	508	317.5	317.5	317.5
Total Angular Momentum	508	444.34	317.49	299.51	273.85
Total Rotational Energy	508	418.64	317.49	292.80	253.01

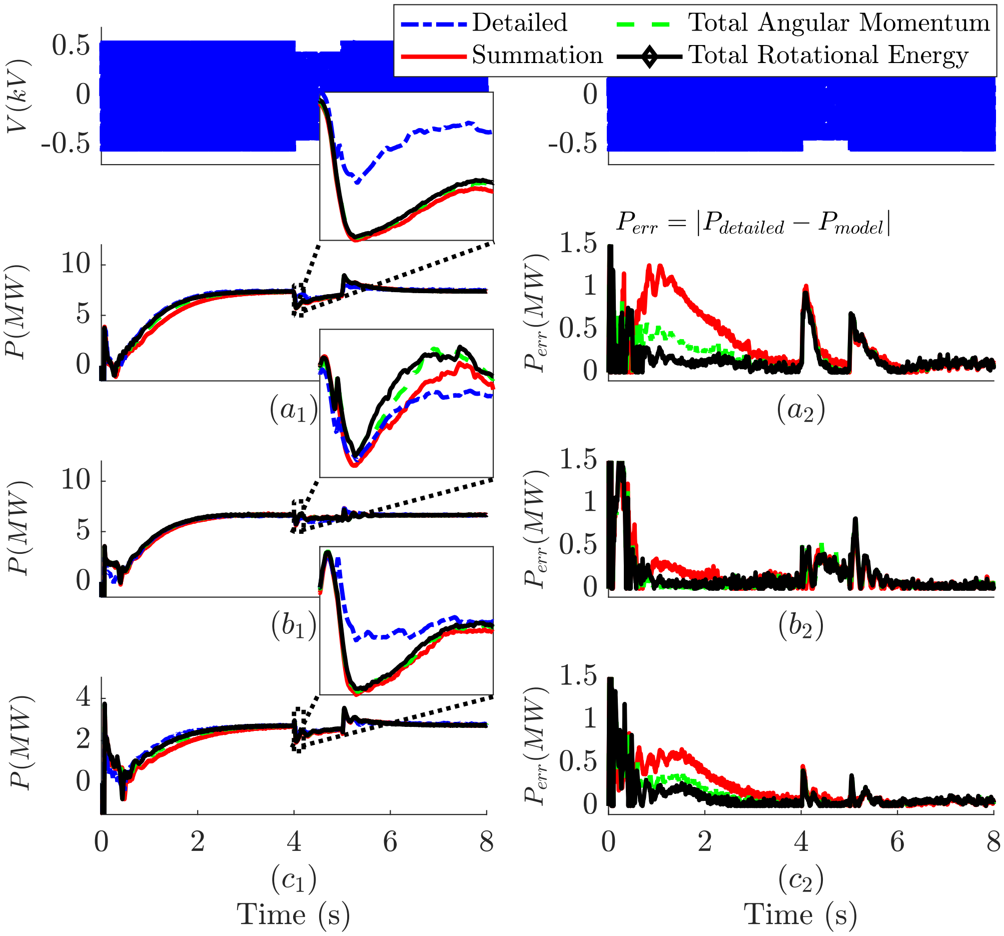

Figure 3.13: Comparison of equivalent inertia derivation with the summation, total angular momentum, and total rotational energy approaches for a detailed 4WTGs DFIG wind farm: $(a_{1,2})$ Scenario 2, $(b_{1,2})$ Scenario 4, $(c_{1,2})$ Scenario 5

at $t = 6s$ to compare the system's transient behaviour in different approaches. The equivalent inertia J_{eq} is calculated for different approaches and shown in Table 3.3. Simulation results and J_{eq} values shown in Table 3.3 indicate that all approaches

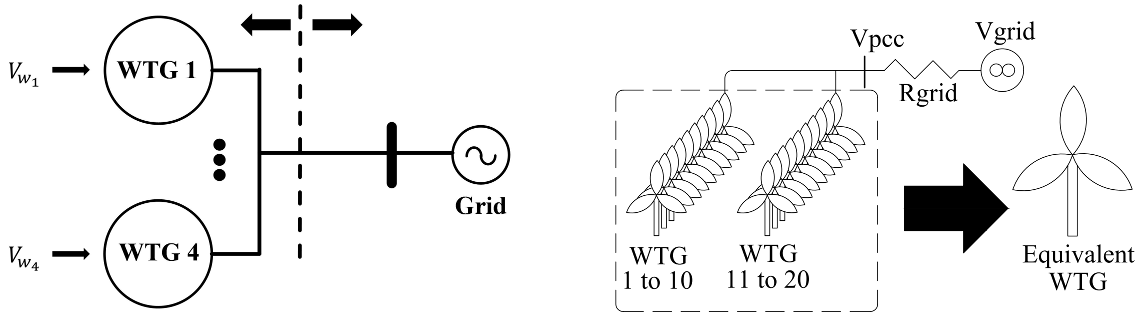

(a) (b)

Figure 3.14: (a) 4-WTGs wind farm, (b) 20-WTGs wind farm, where WTGs parameters and wind speeds are not necessarily similar

result in the same equivalent inertia when WTGs operating speeds are the same. However, the equivalent inertia differs where the operating points are different, which is the case in scenarios 2, 4, and 5. Fig. 3.13 reveals that the total rotational energy approach is more accurate than the other two approaches in all scenarios combined, where V is the PCC voltage, P is the active power, and P_{err} is the active power Agg models error with respect to the detailed model. Therefore, the total rotational energy approach is used to calculate the equivalent inertia J_{eq}.

Using the equivalent DFIM, controllers, and wind turbine parameters, the equivalent WD Agg model for a DFIG-based wind farm is proposed with similar dynamic behavior to the detailed wind farm model.

3.4 Simulations and Results

To evaluate the proposed WD Agg model, several case studies are presented. A 4-WTGs DFIG wind farm shown in Fig. 3.14a and a large-scale 20-WTGs DFIG wind farm shown in Fig. 3.14b are studied under various operating scenarios. The DFIG controller parameters for these scenarios can be found in Table 3.4. Also, the simulation parameters are listed in Tables. 3.5 to 3.11.

The proposed WD Agg model is compared to the existing Full Agg, Zone Agg, and detailed models in all scenarios. The system's transient responses are studied in

Table 3.4: Controller parameters for all DFIG WTGs in scenarios 1 to 5, A, B, C, and D

Parameter	Value	Parameter	Value
σ	$1 - L_m^2 \ / \ L_s L_r$	α_1	$-L_m/L_s$
α_2	$L_r - L_m^2/L_s$	τ_i	$\sigma L_r/R_r$
ω_{ni}	$100/\tau_i$	ω_{nn}	$1/\tau_n$
$K_{p_{idq}}$	$2\omega_{ni}\sigma L_r - R_r$	$K_{i_{idq}}$	$\omega_{ni}^2 L_r \sigma$
K_{pg}	$1/\left(\frac{3}{2}V_s\sqrt{\frac{2}{3}}\right)$	K_{qg}	$-1/\left(\frac{3}{2}V_s\sqrt{\frac{2}{3}}\right)$
τ_{ig}	L_g/R_g	ω_{nig}	$2\pi f$
$K_{p_{idqg}}$	$2\omega_{nig}L_g - R_g$	$K_{i_{idqg}}$	$\omega_{nig}^2 L_g$

Table 3.5: Common parameters for all DFIG WTGs in scenarios 1 to 5, A, B, C, and D

Parameter	Value	Unit	Parameter	Value	Unit
v_s	690	[v]	f	50	[Hz]
V_{DC}	1500	[v]	f_{sw}	4	[kHz]
L_{si}	87	$[\mu H]$	G'	100	–
L_m	2.5	$[mH]$	C_{DC}	80	$[mF]$
R_s	2.6	$[m\Omega]$	L_g	0.4	$[mH]$
R_r	2.9	$[m\Omega]$	R_g	20	$[\mu\Omega]$
p	2	–	K_{pv}	10^3	–
D	0.001	–	K_{iv}	3×10^5	–

scenarios A and B, where the WTGs have equal and unequal parameters, and a 0.2 *pu* voltage sag is applied at $t = 4$s and is cleared at $t = 6$s. The WD Agg model is evaluated for a 20-WTGs large-scale wind farm to demonstrate the generality and applicability of the method in scenario C. Moreover, the generality of the WD Agg model is evaluated for a 4-WTGs DFIG wind farm with a different power coefficient model for WTGs in scenario D. The detailed, Full Agg, Zone Agg, and proposed WD Agg models are simulated by MATLAB \ Simulink 2019 b for these scenarios.

3.4.1 Scenario A: 4-WTGs DFIG Wind Farm With Equal Parameters

Considering an ideal condition where all WTGs parameters and wind speeds are equal results in similar dynamic equations for all voltage nodes. Therefore, it can

Table 3.6: Scenario A specifications: 4-WTGs DFIG wind farm with equal parameters

Parameter	WTG 1	WTG 2	WTG 3	WTG 4	Unit
S	2	2	2	2	[MV]
J	127	127	127	127	$\left[\mathrm{kgm}^2\right]$
τ_n	12.5	12.5	12.5	12.5	[ms]
r	42	42	42	42	[m]
$C_{p\max}$	0.48	0.48	0.48	0.48	–
λ_{opt}	8.1	8.1	8.1	8.1	–
V_W	10	10	10	10	[m/s]

Table 3.7: Full Agg, Zone Agg and proposed WD Agg models RSC and wind turbine parameters comparison

Name of the parameter	Full Agg	Zone Agg	WD Agg
C_{pmax}	0.48	$0.48, 0.48$	0.48
λ_{opt}	8.1	$8.1, 8.1$	15.47
$K_{opt} \times 10^{-5}$	72.684	$12.849, 12.849$	9.0855
K_i	122.9	$245.8, 245.8$	122.9
K_p	0.1443	$0.2886, 0.2886$	0.1443
$L_m[mH]$	0.625	$1.25, 1.25$	0.625
$R_s[m\Omega]$	0.65	$1.3, 1.3$	0.65
$C_{DC}[F]$	0.32	$0.16, 0.16$	0.32
D	0.004	$0.002, 0.002$	0.004

be concluded that similar components of the WTGs are connected in parallel. For example, the $L_{m_{eq}}$ for an ideal-condition equivalent model will be $L_{m_1} \| L_{m_2} \| \ldots . \| L_{m_n}$. Therefore, this ideal condition is the assumption of the existing Full Agg and Zone Agg models. Table 3.7 shows the calculated equivalent parameters in Full Agg, Zone Agg, and proposed WD Agg models. The controller parameters of the system, such as K_p and K_i, have 1/4 value of the detailed system, which shows that they behave similarly to the real impedance components in parallel. The same justification can be made for the turbine shaft parameter D, which has admittance unit type in the WD Agg model. Therefore, Table 3.7 demonstrates the accuracy of the WD Agg method in an ideal condition.

Fig. 3.15 shows the PCC voltage V, active and reactive power $P\&Q$, and phase

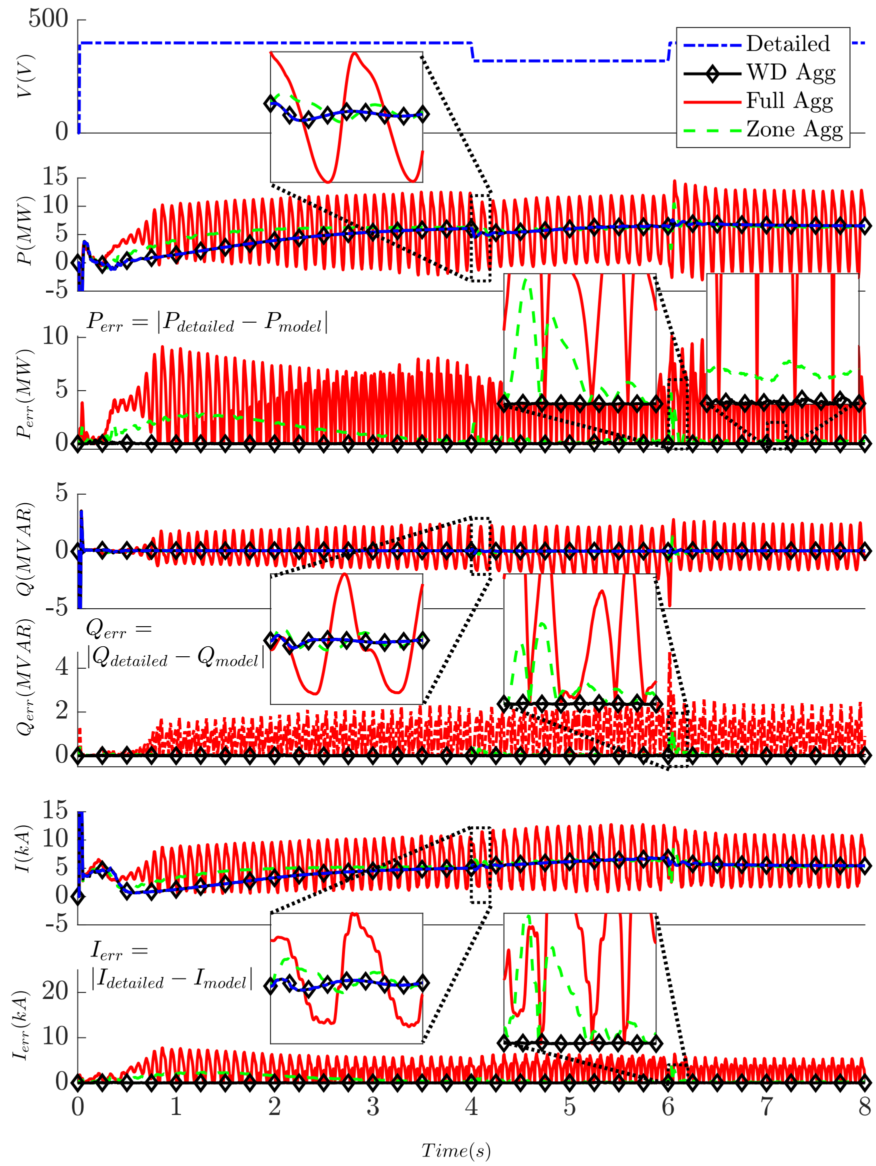

Figure 3.15: Scenario A: equal parameters of WTGs; performance comparisons from PCC point for a detailed 4-WTGs DFIG wind farm, proposed WD Agg, Full Agg, and Zone Agg models

A current I for all aggregation methods and their errors with respect to the detailed model. As shown in Fig. 3.15, the Full Agg model has an oscillatory current due to a very large K_{opt}. Therefore, it can be concluded that if the number of WTGs is increased and the same equation is used to design the control parameters, the Full Agg model may exhibit oscillatory or even unstable behavior. There are three options to solve this issue:

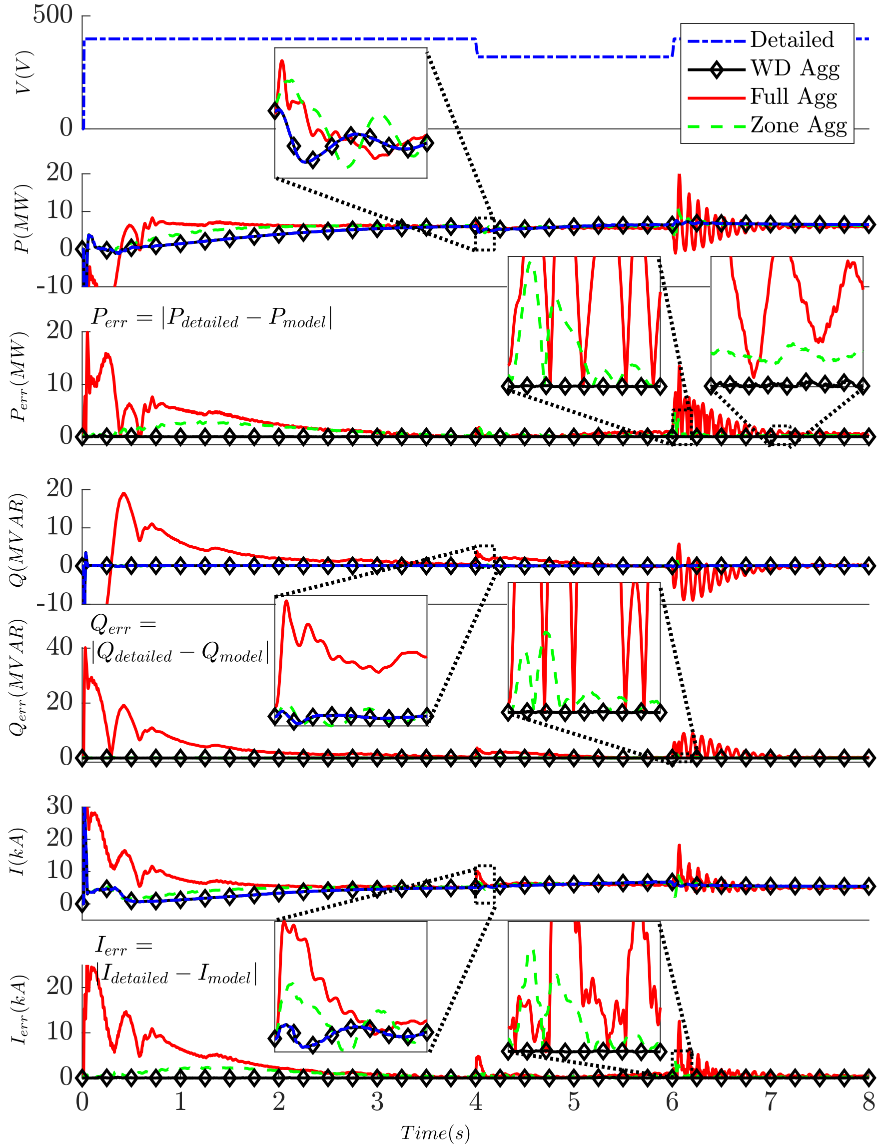

Figure 3.16: Scenario A: equal parameters of WTGs; performance comparisons from PCC point for a detailed 4-WTGs DFIG wind farm, proposed WD, stabilized Full, and Zone Agg models

1) Dividing the WTGs into smaller zones which results in the Zone Agg model with higher model complexity

2) $K_{opt_{eq}}$ can be redesigned by $K_{opt_{eq}} = \sum_{k=1}^{n} K_{opt_k}$ which contradicts with (3.9) and leads to a model inaccuracy.

3) The current controller parameters K_i and K_p can be redesigned by trial and error method to stabilize the model.

Table 3.8: Scenario B specifications: 4-WTGs DFIG wind farm with unequal parameters

Parameter	WTG 1	WTG 2	WTG 3	WTG 4	Unit
S	2	2	1	1	[MVA]
J	127	127	63.5	63.5	[kgm^2]
τ_n	12.5	12.5	12.5	12.5	[ms]
r	42	42	42	42	[m]
$C_{p\,\max}$	0.48	0.48	0.48	0.48	–
λ_{opt}	8.1	8.1	8.1	8.1	–
V_W	11	10	9	8	[m/s]

Fig. 3.16 shows the same results for all methods with modified Full and Zone Agg models with the third option. The stability is achieved at the cost of a slower controller response. The second option is applied to Scenario C. Figs. 3.15 and 3.16 demonstrate the accuracy of the WD Agg model in mimicking the behavior of the detailed model compared to the Full and Zone Agg models in an ideal condition.

3.4.2 Scenario B: 4-WTGs DFIG Wind Farm With Unequal Parameters

In this scenario, unequal turbine parameters and wind speeds listed in Table. 3.8 are considered for the WTGs. As shown, WTGs have unequal rated powers, which affect other parameter values in per unit. The PCC voltage V, active and reactive power $P\&Q$, and phase A current I for all aggregation methods and their errors with respect to the detailed model are shown in Fig. 3.17. The accuracy of the WD Agg model in transient and steady-state is verified compared to the existing Full and Zone Agg models. An error index is defined as the integral of the absolute value of the difference between the model and the detailed system responses:

$$EI = \int_{t=t_0}^{t=t_1} \left(\left|F_{\text{detailed}} - F_{\text{model}}\right|\right) dt, \tag{3.56}$$

where F can be any response curve. The EI is calculated for active power, reactive power, and phase A current curves for all methods between $t_0 = 1$ to $t_1 = 10$. The calculated error is then normalized with respect to the proposed WD Agg model,

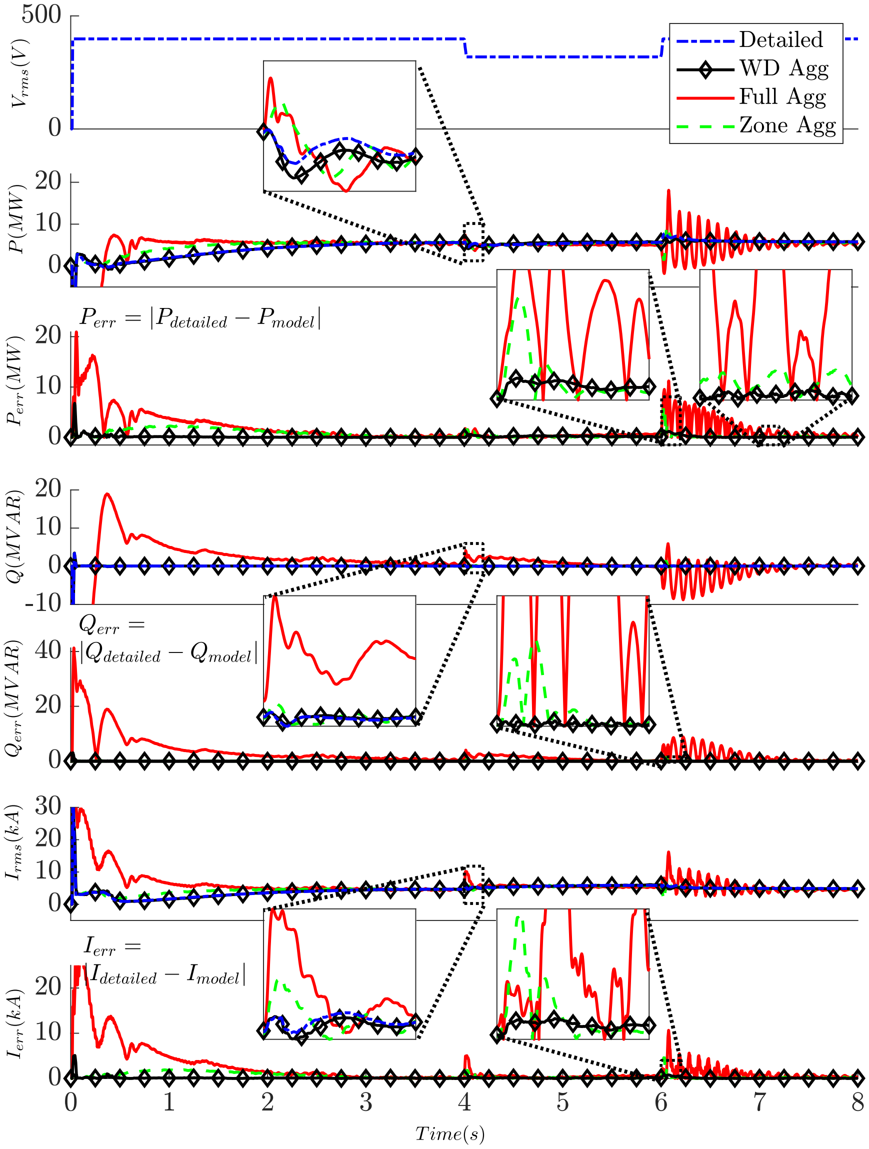

Figure 3.17: Scenario B: unequal parameters of WTGs; performance comparisons from PCC point for a detailed 4-WTGs DFIG wind farm, proposed WD, Full, and Zone Agg models

which has the minimum error. The results are listed in Table. 3.9, which shows that the WD Agg model provides at least 3 times more accurate output power in all scenarios with half the complexity compared to the Zone Agg model.

Table 3.9: Calculated error indexes for active power P, reactive power Q, and phase A current I in scenarios A and B

Error Index	**Active Power**		**Reactive Power**		**Current**	
	Sc.A	Sc.B	Sc.A	Sc.B	Sc.A	Sc.B
EI_{Full}/EI_{WD}	21.41	5.49	74.83	230	9.04	7.15
EI_{Zone}/EI_{WD}	12.13	3.22	3.14	2.71	4.67	1.5

Table 3.10: Scenario C specifications: 20-WTGs DFIG wind farm

Parameter	WTG 1-5 & 11-15	WTG 6-10 & 16-20	Unit
S	2	1	$[MVA]$
J	127	63.5	$[\text{kgm}^2]$
τ_n	50	50	[ms]
r	42	29.7	[m]
$C_{p\,\max}$	0.48	0.48	–
λ_{opt}	7.69	5.44	–

3.4.3 Scenario C: Large-Scale 20-WTGs DFIG Wind Farm

A large-scale wind farm consisting of twenty DFIG WTGs with dissimilar wind speed profiles for two groups of WTGs is simulated and compared for all aggregation methods. The system specification is listed in Table. 3.10. Fig. 3.18 shows the wind speed profile V_w, active power P and its error with respect to the detailed system P_{err} and phase A current I for all aggregation models. The better performance of the WD Agg model in aggregating the detailed model compared to the Full and Zone Agg models is verified in Fig. 3.18. The error index EI defined in (3.56) is calculated for the active power for all aggregation models and normalized by EI_{WD} for the Full and Zone Agg models, which comes to about 7.18 and 4.51, respectively.

3.4.4 Scenario D: 4-WTGs DFIG Wind Farm With Other Existing Power Coefficient Model

To show the generality of the WD Agg method, a 4-DFIG wind farm with the parameters listed in Table. 3.11 is simulated considering the power coefficient model [66,

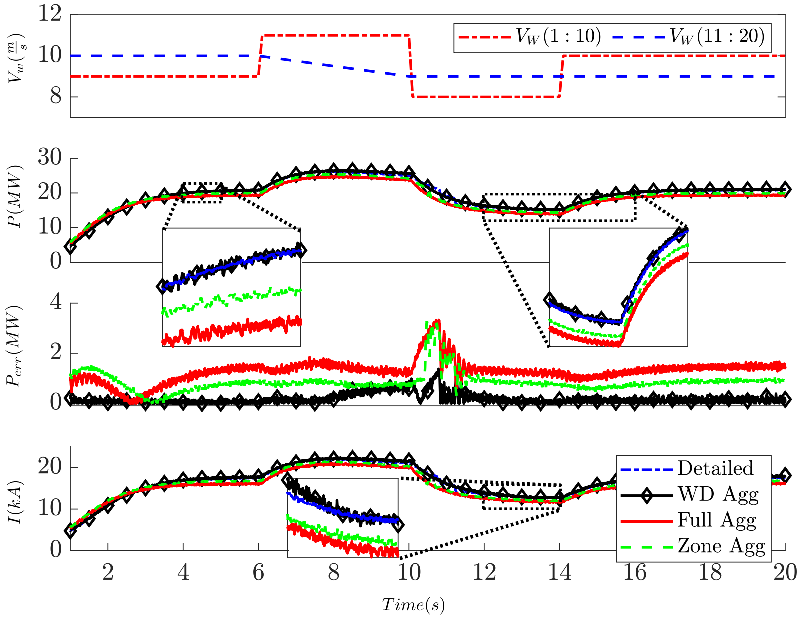

Figure 3.18: Scenario C: dissimilar wind speed profile and unequal WTGs parameters; performance comparisons from PCC point for detailed 20-WTGs DFIG wind farm, proposed WD, Full, and Zone Agg models

Table 3.11: Scenario D specifications: 4-WTGs DFIG wind farm (3.57) power coefficient model

Parameter	WTG 1	WTG 2	WTG 3	WTG 4	Unit
S	2	2	1	1	[MVA]
J	127	127	63.5	63.5	[kgm^2]
τ_n	25	25	25	25	[ms]
r	42	42	29.69	29.69	[m]
$C_{p\max}$	0.42	0.42	0.42	0.42	–
λ_{opt}	6.92	6.92	4.89	4.89	–
V_W	10	8	10	8	[m/s]

67]:

$$C_p = (1.12\lambda - 2.8)e^{-0.38\lambda}, \tag{3.57}$$

with:

$$\lambda = 5.2r\omega_m / \left(\lambda_{opt} V_W G\right). \tag{3.58}$$

The transient behavior of the system is studied through a $0.2pu$ voltage drop at $t = 10$s which is cleared at $t = 12$s. Fig. 3.19 shows the better performance and

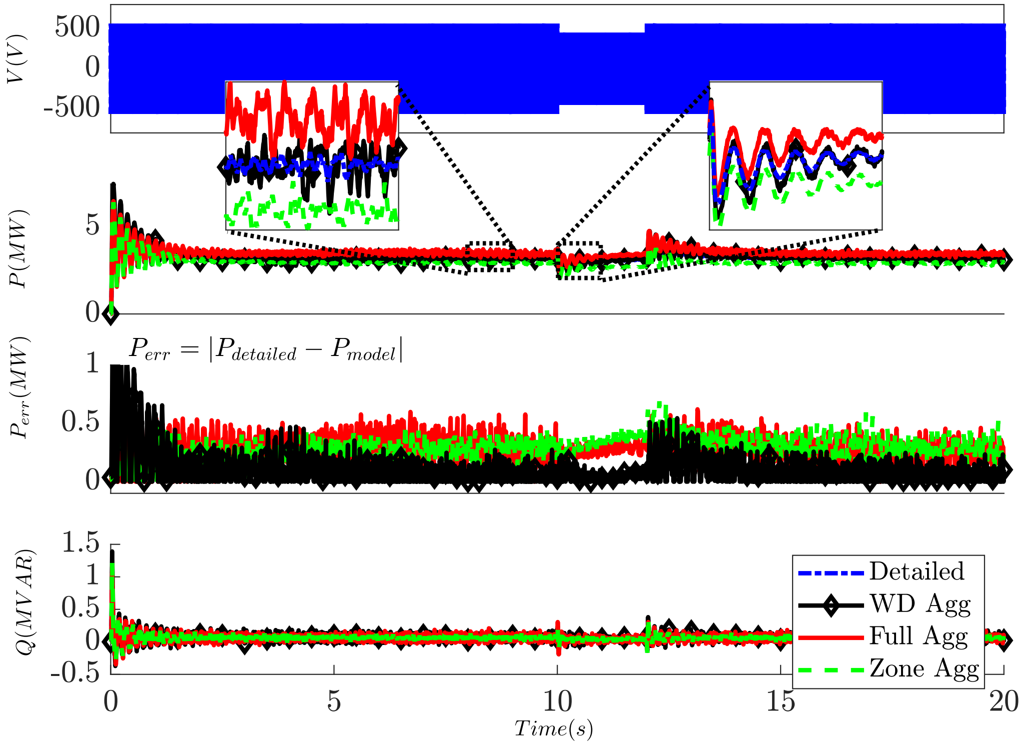

Figure 3.19: Scenario D: WTGs with power coefficient model of (3.57); performance comparisons from PCC point for a detailed 4-WTGs DFIG wind farm, proposed WD, Full, and Zone Agg models

generality of the WD Agg model in aggregating wind farms with other existing power coefficient models.

3.4.5 Scenario E: 4-WTGs DFIG Wind Farm at Oscillatory Mode

In this scenario, the parameters of scenario A are modified to evaluate the performance of the WD Agg model in the condition that the system's eigenvalues are closed to the imaginary axis. The modified parameters are $L_m = 3.5$ mH, $C_{DC} = 8$ mF, $K_{iv} = 3\times10^6$, and $K_{opt} = 5.2242\times10^6$. Fig. 3.20 demonstrates the PCC voltage, active and reactive power and phase A current for this system. The results show that the WD Agg model mimics the behavior of the detailed model with good approximation, while the Full and Zone Agg models show a stable behavior with some sub-oscillation

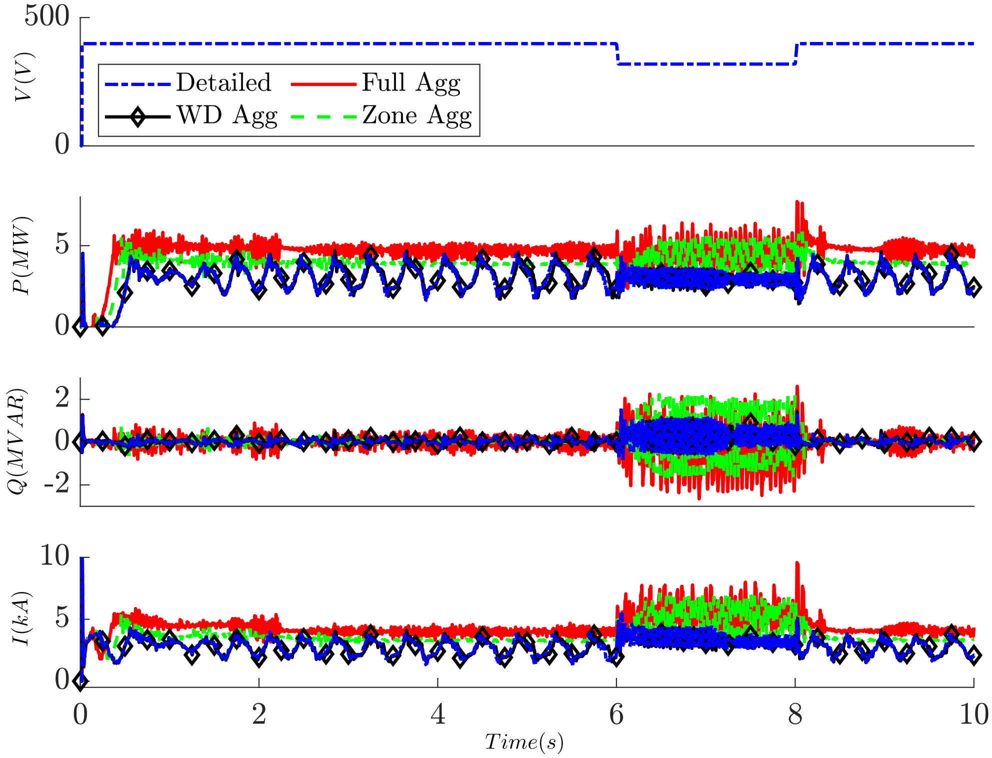

Figure 3.20: Scenario E: Oscillatory operating point for WTGs; performance comparisons from PCC point for a detailed 4-WTGs DFIG wind farm, proposed WD, Full, and Zone Agg models

modes.

The results achieved from scenarios A to E verify the accuracy of the proposed WD Agg model in matching the corresponding detailed model. It is worth mentioning that the linearization is not valid if the system's eigenvalues are pure imaginary [68]. Other methods can be used to study the system behavior in this cases [69–73].

By studying the EI normalized values in different scenarios, it can be concluded that the Zone Agg model performs better than the Full Agg model to the detriment of higher model complexity. The Zone-Agg model for a large-scale wind farm with realistic conditions requires a large number of zones which will also increase the complexity of the model. To reduce the complexity, the number of zones can be reduced at the cost of higher error compared to the WD Agg model. In summary, the proposed WD Agg model has a superior performance compared to the Full Agg and Zone Agg models considering accuracy, simplicity and generality.

3.5 Conclusions

This section proposes a Weighted Dynamic model for large-scale DFIG-based wind farms. This model presents an equivalent WTG consisting of an equivalent wind turbine, generator, and controller with a similar structure as all the WTGs of the wind farm. The $\mathrm{d-q}$ representation of the equivalent generator is obtained by quantifying the contribution of each WTG to the wind farm using Weighted averaging. The WD Agg model is evaluated by simulating 4-WTGs and large-scale 20-WTGs wind farms in 5 different scenarios of various wind speeds and WTGs parameters. It can be observed that the error of the proposed WD Agg model is at least 2 times less than the existing Full and Zone Agg models. The equivalent WTG is obtained through a simple one-time calculation, resulting in significantly less computational burden and model complexity compared to equivalent admittance, optimization methods and Semi Agg models. The simulation results indicate that the proposed WD Agg method is adequately accurate in both transients and steady-state responses, and it can be readily used for modeling large-scale wind farms to reduce the overall computational burden of the system.

Chapter 4

Summary and Future Work

4.1 Summary of Contributions

In this thesis, aggregated models using the Weighted Dynamic Aggregation (WD Agg) method are proposed for two applications of the distributed generation systems: DC Microgrids and Doubly-Fed Induction Generator (DFIG) based wind farms. The proposed reduced-order models' objective is to accurately predict the behavior of the detailed systems in various steady-state and dynamic studies with a less computational burden. The main contributions and conclusions of this thesis are summarized below.

(i) To model and analyze a DC microgrid consisting of droop-controlled DC-DC converters, transmission lines, and a Constant Power load (CPL). A control system is designed, and the state-space model of the detailed system is derived.

(ii) To provide an equivalent converter, controller, and transmission line model as a reduced-order system of droop-controlled DC-DC converters in DC microgrids. The WD Agg has less complexity and computational burden compared to the detailed model. The weight of each converter is determined by calculating the impact factor of that converter in the dynamic response through steady-state and small-signal analysis. Moreover, the state-space model of the equivalent WD Agg system is derived.

(iii) To evaluate the WD Agg model of droop-controlled DC-DC converters in sensitivity, stability, and time-domain steady-state and transient studies. The eigenvalues of the detailed and WD Agg models are derived and compared with other existing reduced-order models in bode plots, root locus diagrams, and for various controller parameters and output filter capacitance. Also, an islanded DC microgrid setup consisting of three DC-DC converters feeding a CPL is tested in various scenarios with equal or unequal controller parameters and input voltages. The results obtained from the experimental and simulation systems are compared with the WD Agg, Tahim, and MSM models. The comparison results indicate that the error of the proposed WD agg method is at least 12 times less than Tahim and MSM models.

(iv) To model and analyze a DFIG-based wind farm. The wind turbine, Doubly-fed induction machine, and AC-DC-AC converter are modeled. The $\mathrm{d-q}$ model and equations of the DFIG wind turbine are derived. The rotor side and grid side converters are designed to extract the maximum energy from the wind, ensure DC-link stability, and determine the system's active and reactive power. The steady-state parameters of the DFIG are calculated. Finally, The $\mathrm{d-q}$ model of the wind farm is derived.

(v) To provide an equivalent mechanical wind turbine, electrical generator, and converter as a reduced-order model of a large-scale DFIG-based wind farm. The single equivalent wind turbine generator is obtained through a simple one-time calculation, resulting in significantly less computational burden and model complexity than other reduced-order models. The steady-state and small-signal equations of the wind farm are derived to find the weight of each wind turbine in the dynamic response of the wind farm.

(vi) To evaluate the WD Agg model of a large-scale wind farm in scenarios with various wind speed zones and unequal WTG parameters. A WD Agg model is presented for 4-WTG and 20-WTG DFIG-based wind farms. The time-domain simulation results are compared with the detailed model results in scenarios with unequal wind speeds, generator parameters, and various wind turbine coefficients. The comparison results verify the WD agg model accuracy in both steady-state and transient behaviors. Also, it is shown that the error of the proposed WD agg method is at least 2 times less than the existing Full and Zone agg models.

4.2 Suggested Future Work

There are a number of directions that this research could proceed in; three of the most promising are outlined below.

(i) To use the WD Agg model to design an islanded DC microgrid with the desired power-sharing between DC-DC converters. DC microgrids are employed in data centers; thus, a straightforward design method can help avoid instability and damage to the system components.

(ii) To apply the WD Agg method on CPLs. The CPL converters are typically the source of instability; therefore, an aggregation model of parallel CPLs is beneficial in stability analysis and power-sharing decisions.

(iii) To apply the WD Agg method to other distributed generation systems consisting of parallel subsystems such as PV systems. The reduced-order model should accurately mimic the behavior of the detailed model in various steady-state and dynamic studies to reduce the computational burden and complexity of the system studies.

Bibliography

[1] E. M. Gui and I. MacGill, “Typology of future clean energy communities: An exploratory structure, opportunities, and challenges,” *Energy research & social science*, vol. 35, pp. 94–107, 2018.

[2] P Monica and M Kowsalya, “Control strategies of parallel operated inverters in renewable energy application: A review,” *Renewable and Sustainable Energy Reviews*, vol. 65, pp. 885–901, 2016.

[3] M. Cespedes and J. Sun, “Renewable energy systems instability involving grid-parallel inverters,” in *2009 Twenty-Fourth Annual IEEE Applied Power Electronics Conference and Exposition*, IEEE, 2009, pp. 1971–1977.

[4] H. Alrajhi, “A generalized state space average model for parallel dc-to-dc converters,” *Comput. Syst. Sci. Eng*, vol. 41, pp. 717–734, 2022.

[5] M Iqbal, M Azam, M Naeem, A. Khwaja, and A Anpalagan, “Optimization classification, algorithms and tools for renewable energy: A review,” *Renewable and sustainable energy reviews*, vol. 39, pp. 640–654, 2014.

[6] S. Anand and B. G. Fernandes, “Reduced-order model and stability analysis of low-voltage dc microgrid,” *IEEE Transactions on Industrial Electronics*, vol. 60, no. 11, pp. 5040–5049, 2012.

[7] R. Wang, Q. Sun, P. Tu, J. Xiao, Y. Gui, and P. Wang, “Reduced-order aggregate model for large-scale converters with inhomogeneous initial conditions in dc microgrids,” *IEEE Transactions on Energy Conversion*, vol. 36, no. 3, pp. 2473–2484, 2021.

[8] M. Juneja, S. R. Mohanty, and S. K. Nagar, “Robust optimisation-based order reduction and stability analysis of autonomous dc microgrid with consideration of non-linearity,” *International Transactions on Electrical Energy Systems*, vol. 30, no. 2, e12228, 2020.

[9] N. Rashidirad, M. Hamzeh, K. Sheshyekani, and E. Afjei, “A simplified equivalent model for the analysis of low-frequency stability of multi-bus dc microgrids,” *IEEE Transactions on Smart Grid*, vol. 9, no. 6, pp. 6170–6182, 2017.

[10] J. Conroy and R Watson, “Aggregate modelling of wind farms containing full-converter wind turbine generators with permanent magnet synchronous machines: Transient stability studies,” 1, vol. 3, IET, 2009, pp. 39–52.

[11] J. Brochu, C. Larose, and R. Gagnon, “Validation of single-and multiple-machine equivalents for modeling wind power plants,” 2, vol. 26, IEEE, 2010, pp. 532–541.

[12] L. P. Kunjumuhammed, B. C. Pal, C. Oates, and K. J. Dyke, “The adequacy of the present practice in dynamic aggregated modeling of wind farm systems,” 1, vol. 8, IEEE, 2016, pp. 23–32.

[13] H. Liu and Z. Chen, “Aggregated modelling for wind farms for power system transient stability studies,” in *2012 Asia-Pacific Power and Energy Engineering Conference*, IEEE, 2012, pp. 1–6.

[14] X. Tuo, S. Hong, B. Hai, H. Bin, C. Dezhi, and D. Jian, “A practical equivalence method of large scale wind farm,” in *2010 International Conference on Power System Technology*, IEEE, 2010, pp. 1–6.

[15] W. Qiao, R. G. Harley, and G. K. Venayagamoorthy, “Dynamic modeling of wind farms with fixed-speed wind turbine generators,” in *2007 IEEE Power Engineering Society General Meeting*, IEEE, 2007, pp. 1–8.

[16] L. Lin, Y. Chen, and N. Wang, “Clustering wind turbines for a large wind farm using spectral clustering approach based on diffusion mapping theory,” in *2012 IEEE International Conference on Power System Technology (POWERCON)*, IEEE, 2012, pp. 1–6.

[17] L. M. Fernández, F. Jurado, and J. R. Saenz, “Aggregated dynamic model for wind farms with doubly fed induction generator wind turbines,” *Renewable energy*, vol. 33, no. 1, pp. 129–140, 2008.

[18] N. Dhlamini and S. Chowdhury, “The impact of wind farm aggregation techniques for analyzing power system dynamics,” in *2015 50th International Universities Power Engineering Conference (UPEC)*, IEEE, 2015, pp. 1–6.

[19] M. Chowdhury, N. Hosseinzadeh, M. Billah, and S. Haque, “Dynamic dfig wind farm model with an aggregation technique,” in *International Conference on Electrical & Computer Engineering (ICECE 2010)*, IEEE, 2010, pp. 330–333.

[20] K. Balasubramanian, S. B. Thanikanti, U. Subramaniam, N Sudhakar, and S. Sichilalu, “A novel review on optimization techniques used in wind farm modelling,” *Renewable Energy Focus*, vol. 35, pp. 84–96, 2020.

[21] Y. Zhou, L. Zhao, and W.-J. Lee, “Robustness analysis of dynamic equivalent model of dfig wind farm for stability study,” *IEEE Transactions on Industry Applications*, vol. 54, no. 6, pp. 5682–5690, 2018.

[22] Y. Zhou, L. Zhao, and W.-J. Lee, “Robustness analysis of dynamic equivalent model of dfig wind farm for stability study,” 6, vol. 54, IEEE, 2018, pp. 5682–5690.

[23] Y. Zhou, L. Zhao, I. B. Matsuo, and W.-J. Lee, “A dynamic weighted aggregation equivalent modeling approach for the dfig wind farm considering the weibull distribution,” in *2019 IEEE/IAS 55th Industrial and Commercial Power Systems Technical Conference (I&CPS)*, IEEE, 2019, pp. 1–7.

[24] Y. Zhou, L. Zhao, I. B. Matsuo, and W.-J. Lee, “A dynamic weighted aggregation equivalent modeling approach for the dfig wind farm considering the weibull distribution for fault analysis,” 6, vol. 55, IEEE, 2019, pp. 5514–5523.

[25] D. Kajela and M. S. Manshahia, “Optimization of renewable energy systems: A review,” *Int. J. Sci. Res. Sci. Technol*, vol. 3, no. 8, pp. 769–795, 2017.

[26] A. P. N. Tahim, D. J. Pagano, E. Lenz, and V. Stramosk, “Modeling and stability analysis of islanded dc microgrids under droop control,” 8, vol. 30, IEEE, 2014, pp. 4597–4607.

[27] N. Yang, B. Nahid-Mobarakeh, F. Gao, D. Paire, A. Miraoui, and W. Liu, “Modeling and stability analysis of multi-time scale dc microgrid,” vol. 140, Elsevier, 2016, pp. 906–916.

[28] N. Yang, F. Gao, D. Paire, A. Miraoui, and W. Liu, “Distributed control of multi-time scale dc microgrid based on adrc,” 3, vol. 10, IET, 2017, pp. 329–337.

[29] A. Khajehoddin, A. Tabesh, and N. Shabanikia, “Aggregated model of large-scale publication classification wind farms for power system simulation software tools,” pat. US 2020/0401740 A1, 2020.

[30] A. A. Nia, N. Shabanikia, and S. A. Khajehoddin, “Weighted dynamic aggregation modeling of dc microgrid converters with droop control,” in *2021 IEEE Energy Conversion Congress and Exposition (ECCE)*, IEEE, 2021, pp. 700–706.

[31] N. Shabanikia, A. A. Nia, A. Tabesh, and S. A. Khajehoddin, “Weighted dynamic aggregation modeling of induction machine-based wind farms,” *IEEE Transactions on Sustainable Energy*, vol. 12, no. 3, pp. 1604–1614, 2021.

[32] M. Su, Z. Liu, Y. Sun, H. Han, and X. Hou, “Stability analysis and stabilization methods of dc microgrid with multiple parallel-connected dc–dc converters loaded by cpls,” *IEEE Transactions on Smart Grid*, vol. 9, no. 1, pp. 132–142, 2016.

[33] Y. Gui, R. Han, J. M. Guerrero, J. C. Vasquez, B. Wei, and W. Kim, “Large-signal stability improvement of dc-dc converters in dc microgrid,” *IEEE Transactions on Energy Conversion*, vol. 36, no. 3, pp. 2534–2544, 2021.

[34] Y. Han, X. Ning, P. Yang, and L. Xu, “Review of power sharing, voltage restoration and stabilization techniques in hierarchical controlled dc microgrids,” *IEEE Access*, vol. 7, pp. 149 202–149 223, 2019.

[35] L. Meng, T. Dragicevic, J. M. Guerrero, and J. C. Vasquez, “Optimization with system damping restoration for droop controlled dc-dc converters,” in *2013 IEEE Energy Conversion Congress and Exposition*, IEEE, 2013, pp. 65–72.

[36] M. Wu and D. D.-C. Lu, “A novel stabilization method of lc input filter with constant power loads without load performance compromise in dc microgrids,” *IEEE Transactions on industrial electronics*, vol. 62, no. 7, pp. 4552–4562, 2014.

[37] X. Zhu and Z. Pan, "Impedance-model-based ssr study considering dfigs at different locations," in *2017 20th International Conference on Electrical Machines and Systems (ICEMS)*, IEEE, 2017, pp. 1–5.

[38] J. Ma, F. Liu, L. Jiang, M. Wu, Y. Li, and W. Wang, "Multi-dfig aggregated model based ssr analysis considering wind spatial distribution," *IET Renewable Power Generation*, vol. 13, no. 4, pp. 549–554, 2019.

[39] M. Ahmed, L. Meegahapola, A. Vahidnia, and M. Datta, "Stability and control aspects of microgrid architectures–a comprehensive review," *IEEE Access*, vol. 8, pp. 144 730–144 766, 2020.

[40] J. J. Justo, F. Mwasilu, J. Lee, and J.-W. Jung, "Ac-microgrids versus dc-microgrids with distributed energy resources: A review," *Renewable and sustainable energy reviews*, vol. 24, pp. 387–405, 2013.

[41] C Boonseng, D Suksawat, and K Kularbphettong, "Design and control of dc microgrids (dcmg) systems for improving reliability and stability of data centers," in *2019 5th International Conference on Engineering, Applied Sciences and Technology (ICEAST)*, IEEE, 2019, pp. 1–4.

[42] K. Palaniappan, S. Veerapeneni, R. M. Cuzner, and Y. Zhao, "Viable residential dc microgrids combined with household smart ac and dc loads for underserved communities," *Energy Efficiency*, vol. 13, no. 2, pp. 273–289, 2020.

[43] D. Salomonsson, L. Soder, and A. Sannino, "An adaptive control system for a dc microgrid for data centers," in *2007 IEEE Industry Applications Annual Meeting*, IEEE, 2007, pp. 2414–2421.

[44] K. Engelen *et al.*, "The feasibility of small-scale residential dc distribution systems," in *IECON 2006-32nd Annual Conference on IEEE Industrial Electronics*, IEEE, 2006, pp. 2618–2623.

[45] F. Locment and M. Sechilariu, "Modeling and simulation of dc microgrids for electric vehicle charging stations," *Energies*, vol. 8, no. 5, pp. 4335–4356, 2015.

[46] A. Emadi, A. Khaligh, C. H. Rivetta, and G. A. Williamson, "Constant power loads and negative impedance instability in automotive systems: Definition, modeling, stability, and control of power electronic converters and motor drives," *IEEE Transactions on vehicular technology*, vol. 55, no. 4, pp. 1112–1125, 2006.

[47] M. Jyothish and E. Jasmin, "Load sharing control and circulating current minimization of parallel dc-dc converters based on droop index," in *2018 International CET Conference on Control, Communication, and Computing (IC4)*, IEEE, 2018, pp. 84–88.

[48] J. Kumar, A. Agarwal, and V. Agarwal, "A review on overall control of dc microgrids," *Journal of energy storage*, vol. 21, pp. 113–138, 2019.

[49] D. Li and C. N. M. Ho, "A delay-tolerable master–slave current-sharing control scheme for parallel-operated interfacing inverters with low-bandwidth communication," *IEEE Transactions on Industry Applications*, vol. 56, no. 2, pp. 1575–1586, 2019.

[50] S. K. Mazumder, M. Tahir, and K. Acharya, “Master–slave current-sharing control of a parallel dc–dc converter system over an rf communication interface,” *IEEE Transactions on Industrial Electronics*, vol. 55, no. 1, pp. 59–66, 2008.

[51] A. Khalil, A. S. Peng, and A. Asheibi, “Stability analysis of parallel dc-dc converters controlled over communication network,” *International Journal of Power Electronics*, vol. 14, no. 4, pp. 501–528, 2021.

[52] T. Dragičević, X. Lu, J. C. Vasquez, and J. M. Guerrero, “Dc microgrids—part i: A review of control strategies and stabilization techniques,” *IEEE Transactions on power electronics*, vol. 31, no. 7, pp. 4876–4891, 2015.

[53] M. U. Iftikhar, D. Sadarnac, and C. Karimi, “Conducted emi suppression and stability issues in switch-mode dc-dc converters,” in *2006 IEEE International Multitopic Conference*, IEEE, 2006, pp. 389–394.

[54] J. Liu, W. Zhang, and G. Rizzoni, “Robust stability analysis of dc microgrids with constant power loads,” *IEEE Transactions on Power Systems*, vol. 33, no. 1, pp. 851–860, 2017.

[55] B. A. Francis and W. M. Wonham, “The internal model principle for linear multivariable regulators,” *Applied mathematics and optimization*, vol. 2, no. 2, pp. 170–194, 1975.

[56] B. D. Anderson and J. B. Moore, *Optimal control: linear quadratic methods.* Courier Corporation, 2007.

[57] S. A. Khajehoddin, M. Karimi-Ghartemani, and M. Ebrahimi, “Optimal and systematic design of current controller for grid-connected inverters,” *IEEE Journal of Emerging and Selected Topics in Power Electronics*, vol. 6, no. 2, pp. 812–824, 2017.

[58] K Richardson *et al.*, “Green energy-the road to a danish energy system without fossil fuels,” *Danish Commission on Climate Change Policy*, 2010.

[59] Z. Chen, J. M. Guerrero, and F. Blaabjerg, “A review of the state of the art of power electronics for wind turbines,” *IEEE Transactions on power electronics*, vol. 24, no. 8, pp. 1859–1875, 2009.

[60] G. Abad, J. Lopez, M. Rodriguez, L. Marroyo, and G. Iwanski, *Doubly fed induction machine: modeling and control for wind energy generation.* John Wiley & Sons, 2011.

[61] H. Abu-Rub, M. Malinowski, and K. Al-Haddad, *Power electronics for renewable energy systems, transportation and industrial applications.* John Wiley & Sons, 2014.

[62] R. Teodorescu and F. Blaabjerg, “Flexible control of small wind turbines with grid failure detection operating in stand-alone and grid-connected mode,” *IEEE transactions on power electronics*, vol. 19, no. 5, pp. 1323–1332, 2004.

[63] R. Teodorescu, M. Liserre, and P. Rodriguez, *Grid converters for photovoltaic and wind power systems.* John Wiley & Sons, 2011.

[64] F. Blaabjerg, R. Teodorescu, M. Liserre, and A. V. Timbus, “Overview of control and grid synchronization for distributed power generation systems,” *IEEE Transactions on industrial electronics*, vol. 53, no. 5, pp. 1398–1409, 2006.

[65] P. Krause, O. Wasynczuk, S. D. Sudhoff, and S. Pekarek, “Alternative forms of machine equations,” 2013.

[66] Y. Xia, K. H. Ahmed, and B. W. Williams, “Wind turbine power coefficient analysis of a new maximum power point tracking technique,” *IEEE transactions on industrial electronics*, vol. 60, no. 3, pp. 1122–1132, 2012.

[67] R. Wai, C. Lin, and Y. Chang, “Novel maximum-power-extraction algorithm for pmsg wind generation system,” *IET Electric Power Applications*, vol. 1, no. 2, pp. 275–283, 2007.

[68] H. K. Khalil, “Performance recovery under output feedback sampled-data stabilization of a class of nonlinear systems,” *IEEE Transactions on Automatic Control*, vol. 49, no. 12, pp. 2173–2184, 2004.

[69] L. Yang, Z. Xu, J. Østergaard, Z. Y. Dong, K. P. Wong, and X. Ma, “Oscillatory stability and eigenvalue sensitivity analysis of a dfig wind turbine system,” *IEEE Transactions on Energy Conversion*, vol. 26, no. 1, pp. 328–339, 2011.

[70] K. Liao, Z. He, Y. Xu, G. Chen, Z. Y. Dong, and K. P. Wong, “A sliding mode based damping control of dfig for interarea power oscillations,” *IEEE Transactions on Sustainable Energy*, vol. 8, no. 1, pp. 258–267, 2016.

[71] D. Ke, F. Shen, C. Chung, C. Zhang, J. Xu, and Y. Sun, “Application of information gap decision theory to the design of robust wide-area power system stabilizers considering uncertainties of wind power,” *IEEE Transactions on Sustainable Energy*, vol. 9, no. 2, pp. 805–817, 2017.

[72] M. J. Morshed and A. Fekih, “A probabilistic robust coordinated approach to stabilize power oscillations in dfig-based power systems,” *IEEE Transactions on Industrial Informatics*, vol. 15, no. 10, pp. 5599–5612, 2019.

[73] A. Xue, X. Fu, Z. Wang, and J. Wang, “Analysis of sub-synchronous band oscillation in a dfig system with non-smooth bifurcation,” *IEEE Access*, vol. 7, pp. 183 142–183 149, 2019.